

Experimental and Numerical Investigation of Brittle Ice Crushing Loads

**Vom Promotionsausschuss der
Technischen Universität Hamburg**

zur Erlangung des akademischen Grades

Doktor-Ingenieur (Dr.-Ing.)

genehmigte Dissertation

von

Hauke John Herrnring, M.Sc.

aus

Hamburg

2023

Vorsitzender des Prüfungsausschusses:

Prof. Dr.-Ing. Otto von Estorff

Gutachter:


Prof. DSc. (Tech) Sören Ehlers

Univ.-Prof. Dr.-Ing. Jürgen Grabe

Tag der mündlichen Prüfung:

16. Dezember 2022

DOI: 10.15480/882.4923

ORCID: 0000-0002-3583-684X 

License: This work is licensed under the Creative Commons Attribution 4.0 International License (CC BY 4.0). To view a copy of this license, visit <https://creativecommons.org/licenses/by/4.0/>. Wherever marked otherwise, parts of the text, figures or other third party material is excluded from the above-mentioned license.

Abstract

Ice loads pose a significant risk for ship operation in ice covered waters. At low strain rates, the ice behaves ductile, whereas at high strain rates it reacts in brittle manner. This thesis focuses on the brittle mode, which is the dominating mode for ship-ice interactions. A multitude of experimental data and numerical approaches for the simulation of ice can be found in the literature. Nevertheless, versatile and profound validated simulation techniques are currently missing to access the consequences of an iceberg collision or ice floe impact.

Hence, in this thesis the new experimental set-up of the ice extrusion tests for the investigation of ice crushing loads is presented and a finite element model for the simulation of brittle ice-structure interaction problems is developed. During the comprehensive ice extrusion test campaign confined ice specimens were pushed against quasi rigid or full-scale ship structures. The obtained results reveal that the failure mode depends mainly on the test speed, while the confinement of ice mainly determines the load level.

The core objective of the developed Mohr-Coulomb Nodal Split (MCNS) ice material model is to enable efficient physical based ice-structure interaction simulations. Unlike previously existing ice models, the MCNS model takes spalling and crushing into account, which significantly increases the versatility and reliability of the approach. The confinement effect on the crushing strength and the anisotropic material behaviour of the ice is modelled by the Mohr-Coulomb material model. To preserve mass and energy as much as possible, the node splitting technique is applied in addition to the element erosion technique. To validate the findings of the model, the simulated maximum ice forces and contact pressures are compared with small- and large-scale ice extrusion experiments and double pendulum tests. During validation, the MCNS model shows a very good agreement with these experimental results.

Finally, a procedure is proposed to simulate full-scale ship-ice collisions on basis of the given methodologies and experimental results.

Preface

This doctoral thesis is the result of my research work at the Institute of Ship Structural Design and Analysis of Hamburg University of Technology (TUHH) between 2015 and 2022. During this time I had the pleasure to work with a multitude of great and inspiring people and I thank all of them for their support.

First, I would like to thank my supervisor, Prof. Sören Ehlers. Sören, I am very thankful for the opportunity to work in this still fascinating field of research, and that you taught me to think outside the box. Your positive approach to problems and the certainty that we can solve them will definitely strengthen me my whole life. I would like to thank also Prof. Jürgen Grabe for acting as a co-supervisor and Prof. Otto von Estorff chairing the Phd-defense.

Further, I would like to express my gratitude to Dr. Franz von Bock und Polach for giving me the necessary freedom to finalise my work.

In particular, the extensive experimental campaign could not have been realized by me alone. Special thanks to my friend and colleague Jan M. Kubiczek. I will never forget the many hours we spent together in the lab, in the cold room or in discussions. Furthermore, I would like to thank especially Andrzej Iwaszko, Robin Härer, Eric Grove, Nils Schwickardi and Michel Röben for preparing the ice specimens and great help during the different experimental campaigns.

I would like to thank all colleagues and friends at the institute or anyway at Hamburg University of Technology for great cooperation and exchange. I am also very thankful for joining the fantastic NATO AVT300 and later AVT367 working groups. For the funding of our research, I would like to thank in particular Dr. Paul Hess of the Office of Naval Research (ONR).

Further, my thanks go to my family and friends for the loving support and never-ending interest in my work.

I would like to dedicate the last lines to my wife Franziska Herrnring. You have experienced all the ups and downs of this thesis. I thank you for your understanding, your support and pragmatism in dealing with obstacles.

Hamburg, 21.02.2023

Contents

| | |
|--|------------|
| List of Abbreviations | 5 |
| Original Features | 6 |
| 1. Introduction | 7 |
| 1.1. Objective | 10 |
| 1.2. List of Publications | 11 |
| 1.3. Limitations | 13 |
| 1.4. Structure of the Thesis | 14 |
| 2. State of the Art | 15 |
| 2.1. The Material Behaviour of Ice | 15 |
| 2.2. Ice-Structure Interaction | 21 |
| 2.3. Ice-Structure Interaction Simulations | 30 |
| 3. Experimental Analysis | 34 |
| 3.1. Test Set-ups of the Ice Extrusion Tests | 35 |
| 3.2. Ice Production and Ice Properties | 39 |
| 3.3. I-Scan Pressure Measurements | 42 |
| 3.4. Ice Extrusion Tests - Quasi Rigid Structures | 48 |
| 3.4.1. Conducted tests | 48 |
| 3.4.2. Results | 48 |
| 3.5. Ice Extrusion Tests - Deformable Structures | 59 |
| 4. The Mohr-Coulomb Nodal Split Ice Model | 64 |
| 4.1. Methodology | 64 |
| 4.2. Contact Modelling | 68 |
| 4.3. Verification of the MCNS Model | 69 |
| 4.4. Ice Extrusion Test Simulations - Quasi Rigid Structures | 72 |
| 4.5. Ice Extrusion Test Simulations - Deformable Structures | 76 |
| 4.6. Double Pendulum Test Simulation | 85 |
| 5. Discussion | 89 |
| 6. Conclusion | 95 |
| A. Tensile Test Results for Panel1 and Panel2 | 109 |
| B. LS-Dyna Keyword Decks of Used Material Models | 111 |

List of Abbreviations

| | |
|--------------------|---|
| CZM | Cohesive Zone Method |
| IACS | International Association of Classification Societies |
| IMO | International Maritime Organisation |
| ISI | Ice-Structure Interaction |
| FE | Finite Element |
| FEM | Finite Element Method |
| FSICR | Finnish-Swedish Ice Class Rules |
| HPZ | High Pressure Zone |
| MAE | Mean Average Error |
| MARPOL | International Convention for the Prevention of Pollution from Ships |
| MCNS | Mohr-Coulomb Nodal Split |
| nMAE | Normalised Mean Average Error |
| NSR | Northern Sea Route |
| POLAR Class | Unified Requirements concerning Polar Class ships |
| POLAR Code | International Code for Ships Operating in Polar Waters |
| POLARIS | Polar Operational Limitations Assessment Risk Indexing System |
| PSC | Polar Ship Certificate |
| SMP | Shared Memory Parallel |
| SOLAS | International Convention for the Safety of Life at Sea |

Original Features

Ice loads are crucial for the design of marine structures exposed to critical ice conditions. The material- and failure behaviour of ice is difficult to describe because it is characterized by many different continuum and fracture mechanic processes. Unlike the simulation of steel structures, only highly idealized material models are available for the simulation of ice. No ice model has yet been shown to be particularly valid and generally applicable; therefore, in this thesis, the crushing behaviour of ice was investigated experimentally and based on these results an ice material model was developed, which is able to represent spalling and crushing for the first time.

Therefore, this thesis makes original contributions on the following fields:

1. A novel experimental set-up for the investigation of continuous crushing dominated ice-structure interaction processes is proposed. The ice extrusion test set-up achieved for the first time the investigation of brittle ice loads up to 2.9 MN in a laboratory environment. More than 350 tests in three different scales are presented. The extensive test program enables a profound assessment of velocity, geometrical, confinement and scale effects on the crushing strength.
2. The contact areas and pressure distributions of a majority of the ice-extrusion tests conducted were determined by using the I-Scan pressure measurement system of the manufacturer TekScan. To achieve best possible results a novel calibration approach for the I-Scan system is proposed.
3. A novel numerical ice model for design purposes is developed, which enables for the first time an efficient representation of spalling and crushing failure. Unlike in the existing models, the proposed physical based Mohr-Coulomb Nodal Split model tries to preserve the mass and volume as far as possible. The model was developed based on the experimental results of the ice extrusion test results. For the validation rigid and deformable ship structures were simulated, under consideration of the right representation of forces, contact pressures and structural deformations.
4. Based on the experimental and numerical findings, a framework for valid full-scale ice-structure interaction simulations is proposed.

1. Introduction

From a security perspective, the polar and ice-covered waters are a particularly challenging place for ships and offshore structures. Harsh weather conditions, remoteness, ice loads and very fragile ecosystems place high demands to the technology used.

Historically, ship navigation in ice-covered waters is a relatively recent episode. Sailing ships were not able to break thicker ice. Only the use of combustion engines in combination with propeller drives enable the construction and operation of first icebreakers in the mid of the 19th century (Riska, 2010).

It is difficult to derive a general trend for Arctic shipping. A major breakthrough of trans-Arctic routes in maritime trade between Europe and Asia has so far not occurred (X. Li et al., 2019). On the one hand, there were more ship entries into the Polar Region and an increase of the tonnage from 2.8 million tons in 2013 to 32 million tons in 2020 on Russia's Northern Sea Route (NSR) (Danilov, 2021; Humpert, 2020). On the other hand, is the tonnage on the NSR compared to the Suez channel still small. Given the Gazprom's Novy Port crude oil project and Novatek's Yamal LNG project accounting for 80% of the tonnage to Russia's NSR (Humpert, 2020), it seems unlikely that the traffic will increase towards Europe and America in the near future, considering the Ukraine war in 2022.

However, as a result of political disruptions, the military interest of Western countries in Arctic waters is currently increasing (Ministry of Defence, 2022). A further driver for Arctic shipping was a strong increase in tourist activity in polar regions in pre-Corona pandemic times (IAATO, 2019).

Ice is an obstacle to any ship (Canadian Coast Guard, 2012) and can cause significant damage even to ice-strengthened ship structures. The consequences of a collision of an ice strengthened cargo vessel with a Bergy Bit (large piece of floating glacier ice, less than 5 m but more than 1 m above the sea level (World Meteorological Organization, 2015)) is shown in Figure 1.1. The outer hull of the bulbous bow was ruptured and the structure is massively deformed over a large area. Even in the recent past, total and ice-related ship losses, such as the sinking of the expedition cruise vessel MS Explorer in 2007, had to be registered (Marchenko, 2014).

Current rules for ships operating in icy water can be subdivided into international and national regulations. Ships operating in Arctic or Antarctic waters are subject to the International Code for Ships Operating in Polar Waters (POLAR Code) (International Maritime Organization, 2016b). The POLAR Code came into force in 2017. The POLAR Code is an extension of the International Convention for the Safety of Life at Sea (SOLAS) and International Convention for the Prevention of Pollution from Ships (MARPOL) given by the International Maritime Organisation (IMO) an agency of the United Nations. The POLAR Code includes goal based regulations regarding the equip-



Figure 1.1.: Damaged bulbous bow of a cargo vessel with a Lloyd’s Register 100 A1 ice class after a collision with a Bergy Bit (Canadian Coast Guard, 2012)

ment, design & construction and operation & manning to ensure safe ship operation and to protect the polar environment. For the ship structure the POLAR Code imposes functional requirements on the used materials and the design. Both should be suitable for the harsh environment and foreseen ice conditions (International Maritime Organization, 2016b).

A ship approved under the IMO POLAR Code obtains a Polar Ship Certificate (PSC) according to the three following categories (International Maritime Organization, 2016b):

- **Category A**, which means a ship designed for operation in polar waters in at least medium first-year ice, which may include old ice inclusions.
- **Category B**, which means a ship not included in category A, designed for operation in polar waters in at least thin first-year ice, which may include old ice inclusions.
- **Category C**, which means a ship designed to operate in open water or in ice conditions less severe than those included in categories A and B.

The issuance of a PSC requires an operational assessment to specify a ship’s operational limitations, taking into account the anticipated range of operating conditions in terms of operation in low air temperature, ice loads, icing and high latitude, among other hazards that a ship may encounter in polar waters (IMO, 2015). The risk assessment could be carried out for a specific ship or operation.

Structural scantlings have to be accepted by the administration or a recognized organisation (e.g. classification society). In particular for category A and B ships, reference is made to the IACS POLAR Class (International Association of Classification Societies, 2019). Also the operation of non ice strengthened vessels is allowed, if the ship

structure is adequate in the opinion of the administration for the intended application (International Association of Classification Societies, 2019). More information on the IMO POLAR Code can be found for example in Lloyd's Register (2016). Additional to the international IMO POLAR Code, there are national regulations for Canadian and Russian waters existing.

Ships under IMO POLAR Code have to conduct a risk assessment. For this purpose the IMO published the Polar Operational Limitations Assessment Risk Indexing System (POLARIS) (International Maritime Organization, 2016a). POLARIS assesses the risk of a ship being damaged by ice considering the ice conditions and the ship's assigned IACS POLAR Class notation. The POLARIS is fully empirical. The result is a non-physical risk parameter (Bergström et al., 2022).

The IACS POLAR Class was developed between 1992 and 2000 by the International Association of Classification Societies (IACS). The IACS is the association of the leading ship classification societies. Goal of the development of the IACS POLAR Class was the harmonisation of the previously more than 30 different ice classes assigned by classification societies intended for operating in polar regions (Kämäräinen et al., 2017). The IACS POLAR Class considers a multiyear ice edge glancing impact as design case (Ekaterina Kim et al., 2016). The ice edge could be a part of the level ice field or a separate ice floe. The load is calculated by a modified Popov ice load model together with a pressure-area approach (Kämäräinen et al., 2017; Ekaterina Kim et al., 2016). The IACS POLAR Class rules contain also global longitudinal and machinery strength requirements. Performance requirements such as a minimum speed under certain ice conditions are not considered (Kämäräinen et al., 2017).

In the Baltic Sea, traffic density is higher than in polar regions, even in the winter. For the winter navigation in the Baltic Sea the Finnish-Swedish Ice Class Rules (FSICR) (Finnish Transport Safety Agency, 2017) are mandatory. The FSICR is a national regulation of Finland and Sweden for their territorial waters and a relevant part of the winter navigation system in the Baltic Sea. The winter navigation system consists mainly of icebreaker escorts, ice-strengthened vessels, and fairway fees that depend on the ice classification of the vessels. The overall goal of the winter navigation system is to enable for all players an economically efficient winter navigation. This means a trade-off of less as possible icebreaker assistance and less as possible ice-strengthening, since the more expensive as well as heavier ice-strengthened ships compete with conventional ships under open water conditions outside winter.

The origins of the FSICR rules can be traced back to the year 1890. The FSICR are the industrial standard for first year ice conditions (Riska, 2010). The design scenario of the FSICR is a ship operation with icebreaker assistance in broken ice channels. As the Baltic sea is ice free during summer only first year ice is considered. An empirical design ice pressure, based on idealized back calculations of ship damages (Riska, 2022), is used together with a simplified elastic structural model. Additionally to structural requirements also minimum ship speeds are specified. The development of the FSICR is supported by damage statistics (Kujala, 1991; Hänninen, 2005). According to these studies, the rules were adjusted several times (Kämäräinen et al., 2017).

Summarized essential elements of the existing regulations for structural design based

on empirical data and operational experience. A direct design or physical based risk assessment of a given impact scenario is currently not possible based on existing methods, although the POLAR code already allows this.

Moreover, it is difficult to assess if existing rules can also be applied to new ship types as for example naval vessels or increasingly large ice strengthened merchant vessels, since these ships are significantly different from the original data used for rule development. Within the current ice rules the ice load is idealized with a constant design pressure. Real brittle ice loads are characterized by temporal and special varying ice pressure distributions (R. Gagnon et al., 2020). It has been shown, that local ice loads are potentially more dangerous for ship structures than comparable constant pressures (Erceg et al., 2014).

As mentioned before, the hazard potential of ice is reflected by different significant damages also of ice-strengthened ships (Hänninen, 2005; Banda et al., 2014; Goerlandt et al., 2017; Marchenko, 2014). However, physical based reliable and widely applied simulation approaches for the assessment of structural response in case of ice loads are currently missing. The reason for this is essentially the complex material behaviour of ice (F. R. U. v. Bock und Polach et al., 2019; Bergström et al., 2022).

Nevertheless, an ice-strengthened ship structure means a significant increase of the ship mass compared to conventional vessels. Thicker plating and smaller spacings of the supporting structures are needed. Transverse frames are often used in the ice belt to distribute the ice load over several frames. An ice class incur significant higher capital and fuel costs compared to a non ice classed vessel (Solakivi et al., 2019). The increase of shipping costs for a IA or IA Super container ship according to FSICR in comparison to a conventional vessel is given by 9% (Solakivi et al., 2019). This shows the need of accurate methods for structural design, risk assessment and rule development, since unnecessary heavy ships are economically and ecologically undesirable.

This thesis will address the physical based modelling of ice loads for ship-ice interaction problems. The direct load assessment in open water is state of the art. Reliable and universally applicable methods for the direct assessment of ice loads are missing (F. R. U. v. Bock und Polach et al., 2019). Depending on the failure modes, fracture- or continuum mechanical processes determine the achievable ice forces (Schulson; Duval, 2009). However, the direct assessment would be beneficial:

- to determine the structural consequences of specific ship-ice collision,
- to support the development of new ice rules,
- to verify the applicability of existing rules to new ship types or dimensions,
- for investigations after accidents or in the scientific scope.

1.1. Objective

To achieve the goal of a physical based ice load assessment for ice-structure interaction problems with respect to ship operation, the following objectives were defined within

this thesis:

1. Identify experimentally the influence of confinement and scale on ice forces and ice pressure distributions.
2. Develop a first principle-based simulation technique for ice loads for direct load assessment. The model to be developed should be validated against the previously conducted experimental work.

1.2. List of Publications

This thesis is based on the following peer-reviewed publications:

- (P1):** Bock und Polach, Franz R. U. von; Klein, Marco; Kubiczek, Jan; Kellner, Leon; Braun, Moritz; Herrnring, Hauke (2019): State of the Art and Knowledge Gaps on Modelling Structures in Cold Regions. In: International Conference on Offshore Mechanics and Arctic Engineering OMAE2019-95085. DOI: 10.1115/OMAE2019-95085.

Herrnring contributed to the general outline of the paper and wrote parts of the ice mechanic section.

- (P2):** Herrnring, Hauke; Kubiczek, Jan M.; Ehlers, Sören (2020): The Ice Extrusion Test: A novel Test Setup for the Investigation of Ice-Structure Interaction – Results and Validation. In: Ships and Offshore Structures 15 (sup1), S. 1–9. DOI: 10.1080/17445302.2020.1713437.

Herrnring and Kubiczek conceived the study and conducted the experiments. Herrnring analysed the data and wrote the paper. Kubiczek contributed with comments and guidance. Ehlers supervised the research.

- (P3):** Herrnring, Hauke; Ehlers, Sören (2021): A Finite Element Model for Compressive Ice Loads Based on a Mohr-Coulomb Material and the Node Splitting Technique. In: Journal of Offshore Mechanics and Arctic Engineering 144 (2). DOI: 10.1115/1.4052746.

Herrnring conceived the ice model and the study. Herrnring created all numerical models, ran simulations, and wrote the paper. Ehlers contributed with comments, guidance and supervision.

- (P4):** Kubiczek, Jan M.; Herrnring, Hauke; Kellner, Leon; Ruckert, Phil; Ehlers, Sören (2022): Ice pressure measurements with TekScan - sensor behavior, calibration and application limits. In: Proceedings of the ASME 2022 41st International & Conference on Ocean, Offshore and Arctic Engineering OMAE 2022. Hamburg, Germany, June 5-10.

Herrnring and Kubiczek conceived the study and conducted most experiments. Kubiczek did data processing, analysed the sensor behaviour and contributed

to the writing. Herrnring worked on the sensor calibration and contributed to writing. Kellner was involved in setting up the test set-up and contributed to the writing. Ruckert provided additional experimental data. Ehlers supervised the research.

- (P5):** Bergström, Martin; Browne, Thomas; Ehlers, Sören; Helle, Inari; Herrnring, Hauke; Khan, Faisal et al. (2022): A comprehensive approach to scenario-based risk management for Arctic waters. In: Ship Technology Research, S. 1–29. DOI: 10.1080/09377255.2022.2049967.

Herrnring contributed with a subsection on the finite element method in the section ice load assessment.

- (P6):** Bergström, Martin; Brown, Thomas; Ehlers, Sören; Helle, Inari; Herrnring, Hauke; Faisal, Khan et al. (2022): Scenario based risk management for Arctic waters. In: Proceedings of the ASME 2022 41st International & Conference on Ocean, Offshore and Arctic Engineering OMAE 2022. Hamburg, Germany, June 5-10.

Herrnring contributed with a subsection on the finite element method in the section numerical ice modelling.

1.3. Limitations

Based on available test capacities and available laboratory times, there were certain limitations to the experimental work and the parameters investigated. The same applies to the numerical work in order to obtain a reasonably solvable ice material model.

The limitations of the thesis are considered as follows:

Experimental work

- Only granular freshwater ice at approximately -10°C was used during the experiments, to achieve isotropic material properties and simplify the ice production process. Influencing factors such as different ice temperatures or salinity were not considered.
- The maximum test velocity in the experimental campaign with 10 mm s^{-1} was low in comparison to real ship related ice-structure interaction scenarios. Higher speeds could not be realized with the available hydraulic test rigs for the given load range.
- It cannot be excluded that some observed effects during the ice extrusion experiments were caused by the elasticity of the experimental set-ups.
- Due to limited time and resources, only a small number of repetitions for every parameter set was tested. This is especially the case for the complex and labour-intensive large-scale tests. Accordingly, statistical uncertainty is not known in all cases.

Numerical modelling

- The proposed Mohr-Coulomb Nodal Split model (MCNS) is intended for the simulation of the ice crushing process under consideration of spalling.
- The material parameters were characterised on basis of the granular freshwater ice at approximately -10°C .
- To allow an efficient formulation of the model, cracks are represented just in a simplified form.
- The MCNS model takes into account the anisotropic behaviour of ice. However, e.g. creep and microcracking are neglected. Furthermore, no heeling or sintering effects of damaged (crushed) elements are considered.
- It was focused on the simulations of laboratory ice-structure interaction experiment. The simulation of ship-ice problems was not performed within this thesis.

1.4. Structure of the Thesis

The scientific concept of the thesis is presented in Figure 1.2. Fundamentally the thesis is subdivided into an experimental and a numerical part. Starting at the state of the art on the mechanical behaviour of ice, ice-structure interaction, and numerical modelling in chapter 2 the experimental work is presented in chapter 3. The experimental work includes also in section 3.3 preliminary works to access and improve the capabilities of the TekScan pressure sensors, which are used in the experimental campaign. In the following, the developed ice load model for the explicit finite element solver LS-Dyna is presented in chapter 4. The thesis is concluded by a discussion of the results in chapter 5, taking into account literature data. At the end of the discussion chapter, a methodology for reliable ship-ice interaction simulations in full-scale based on the found experimental and numerical results is proposed. The work ends with the conclusion in chapter 6.

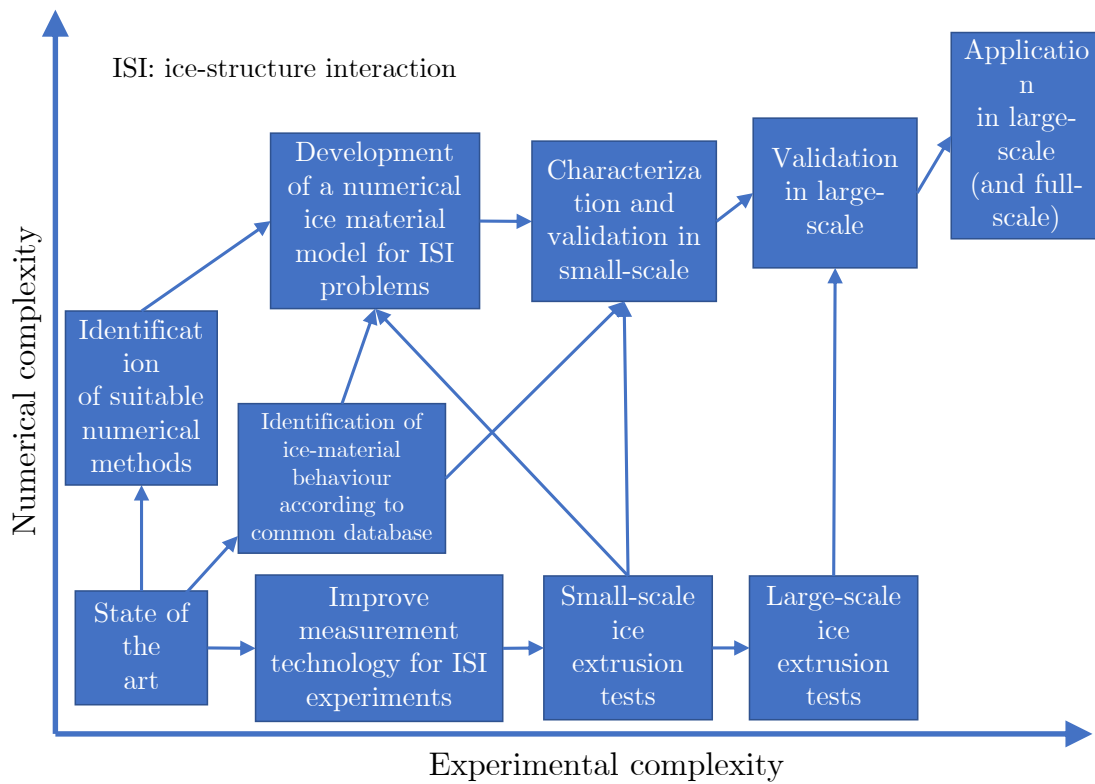


Figure 1.2.: Scientific concept of the thesis

2. State of the Art

The state of the art chapter is divided into four parts: 1. the material behaviour of ice; 2. ice-structure interaction; 3. current rules and design principles for ice strengthened ships; 4. numerical ice models for ice-structure interaction.

2.1. The Material Behaviour of Ice

Many characteristics of ice-structure interaction problems are largely determined by the material behaviour of ice. Therefore, an insight into the known fundamental material behaviour is essential for the following study.

Ice is the solid form of water. There are 12 different crystal structures, plus two amorphous states of ice (Schulson, 1999). Under environmental conditions ice occurs in its crystalline form Ih. The crystalline structure of ice Ih is hexagonal (compare Figure 2.1). The hexagonal lattice structure of ice Ih is responsible for the anisotropic physical properties of the single crystal in radial and axial direction. Therefore, the mechanical properties e.g. Young's modulus of the single crystal are in principle different from polycrystalline ice (Schulson; Duval, 2009). Elastic properties for single crystals and polycrystals are given by Hobbs (2010).

At temperatures near to the melting point, Young's modulus of a single crystal varies less than 30%, from 12 GPa parallel to the c-axis to 8.6 GPa normal to the c-axis (compare Figure 2.1). Along directions within the basal plane Young's modulus is 10 GPa. For randomly oriented polycrystals, typical values of Young's modulus and Poisson's ratio at -5°C are 9.0 GPa and 0.33 (Schulson, 1999).

The grain structure of natural ice and thus also the basic mechanical properties are essentially determined by environmental conditions during freezing and the thermal-mechanical history (Schulson; Duval, 2009). The grain texture of polycrystalline ice can easily be investigated by thin sections under polarized light. An example of granular polycrystalline ice is given in Figure 2.2.

Typically, a distinction is made between sea and freshwater ice. Freshwater ice can be found on inland water ways like rivers and lakes. Icebergs are formed by the calving of glaciers. Glacier ice is also freshwater ice. Sea ice has a much higher salinity than freshwater ice because it freezes on the surface of the sea. However, in case of multi-year sea ice, the salinity of the ice decreases and strength increases accordingly.

The theoretical density of pure ice Ih at 0°C is with 916.4 kg m^{-3} significantly lower compared to liquid water 999.8 kg m^{-3} (Hobbs, 2010). Only through the "density anomaly of water" ice floats on the water surface. Measured densities for freshwater ice in nature are generally lower than the theoretical value due to imperfections. This applies

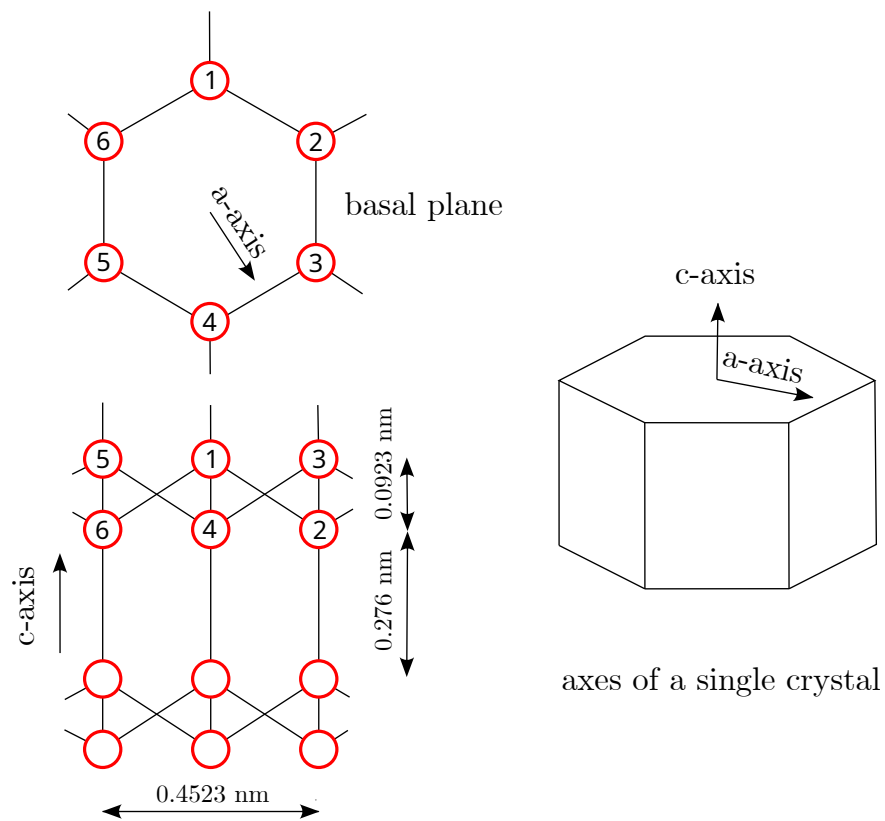


Figure 2.1.: Chrystal structure of ice Ih. Only oxygen atoms are shown (based on Fellin, 2013)

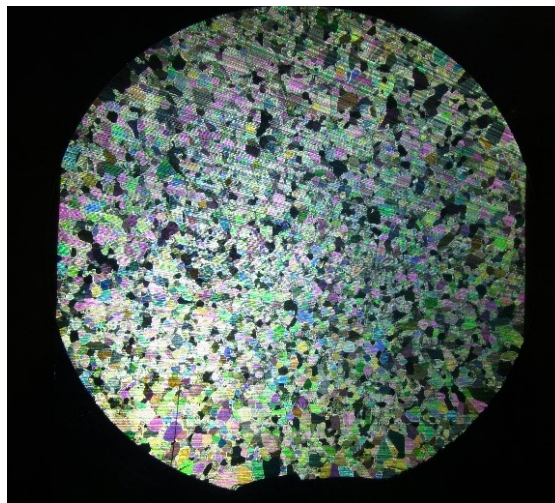


Figure 2.2.: Thin section of a granular freshwater ice specimen under cross-polarized light to visualize the grain structure

especially for sea water ice, where the salt results in a large amount of brine pockets. Generally, the density of ice depends on the temperature. The density in dependence of the temperature for ice Ih and water is presented in the Figure 2.3. The "density anomaly of water" at 0 °C is clearly apparent in the graph.

The mechanical behaviour of ice was subject to several reviews. The mechanical properties of freshwater ice were summarized by Gold (1977) and Petrovic (2003). An extensive review for sea water ice is given by G. W. Timco; Weeks (2010).

In ice-structure interaction problems, ice temperatures close to the melting temperature are common. This results in a high homologous temperature. The homologous temperature is defined as the actual temperature of the material T divided by the melting temperature T_M in Kelvin-scale. For metals creep becomes relevant at a homologous temperature T/T_M greater 0.5 (Rösler et al., 2016). For example Schulson; Duval (2009) shows the importance of creep for long term deformation of ice.

Despite the high homologous temperatures, ice behaves extremely brittle at higher loading rates. As typical for brittle materials, the mechanical failure behaviour in tension and compression is different.

Standard tests are widely used to study the mechanical behaviour of ice. Common tests are in the majority uniaxial, but also different triaxial compression tests were performed. A database of uni- and triaxial tests was collected and analysed by Kellner (2022). It is difficult to carry out ice tensile tests (Schwarz et al., 1981). Therefore, uniaxial tensile tests are only carried out by relatively few researchers (Kellner, 2022). Compared to the uniaxial tensile test, three- and four-point bending tests are less complicated to perform. A review of flexural strength tests is given by G. W. Timco; Brien (1994). According to the different stress states of uniaxial tensile and flexural tests, the obtained strength values are not equivalent (Schulson; Duval, 2009; Ashby et al., 1986).

A schematic sketch of the stress-strain curves for tensile- and compression experiments at different strain rates is given in Figure 2.4a. The figure is based on Schulson (1999). At extreme small strain rates, no large unstable cracks are formed in compression. The stress-strain curve is fully ductile. At high strain rates unstable cracks are formed and the material behaves in compression and tension brittle. For intermediate strain rates the reaction of ice in compression is ductile whereas in tension brittle (Schulson, 1999; Schulson; Duval, 2009). Brittle failure is usually accompanied by an immediate significant drop in load carrying capacity. Pictures of exemplary uniaxial tension and compression tests of the different failure modes are even presented in Figure 2.4a.

Uniaxial failure stresses for tension and compression tests in dependency of the strain rate are presented in Figure 2.4b. An increase of the compressive strength with increasing strain rate is observed until the transition from ductile to brittle fracture is reached. The transition takes place at a strain rate $\dot{\epsilon}$ of approximately $1 \times 10^{-3} \text{ s}^{-1}$. In contrast, the tensile strength seems to be relatively constant for a wide range of strain rates. For high brittle loading rates the compressive strength is a multiple higher than the tensile strength. As a rule of thumb at -10°C and the same grain size Schulson; Duval (2009) indicates $\sigma_c/\sigma_t \approx 8$.

Several authors were able to show experimentally that the compressive strength depends not only on the strain rate, but also on the confinement (Stephen J. Jones, 1982;

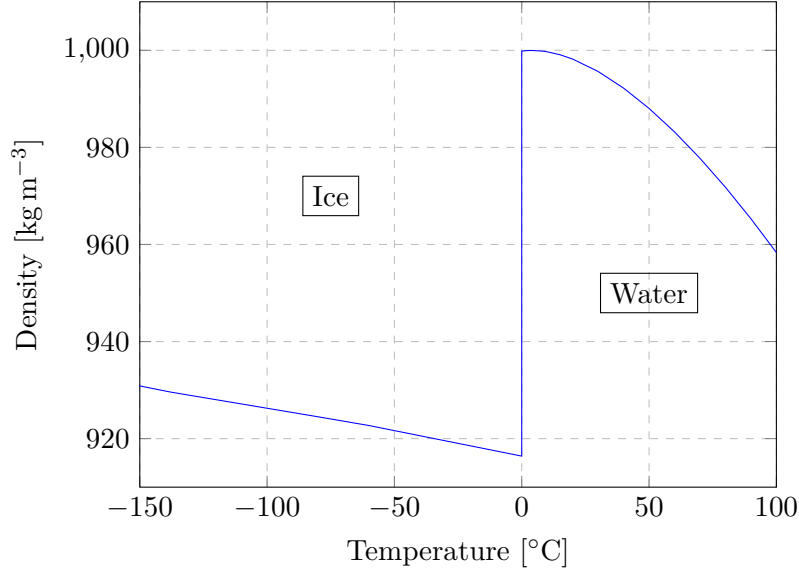
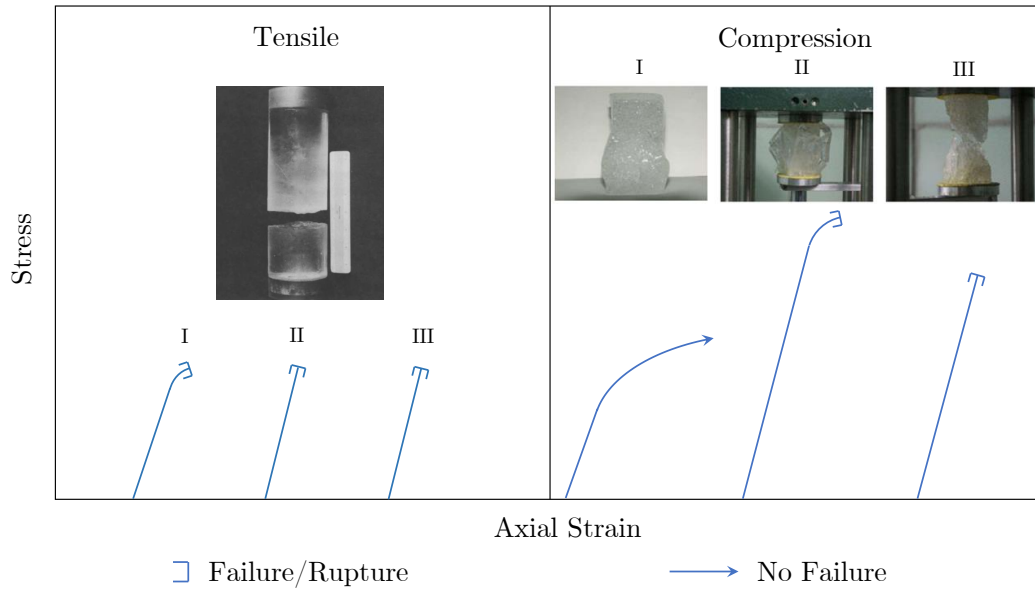


Figure 2.3.: Density of ice Ih and liquid water in dependency of the temperature under constant atmospheric pressure (data according to Hobbs, 2010; Bettin et al., 1990)

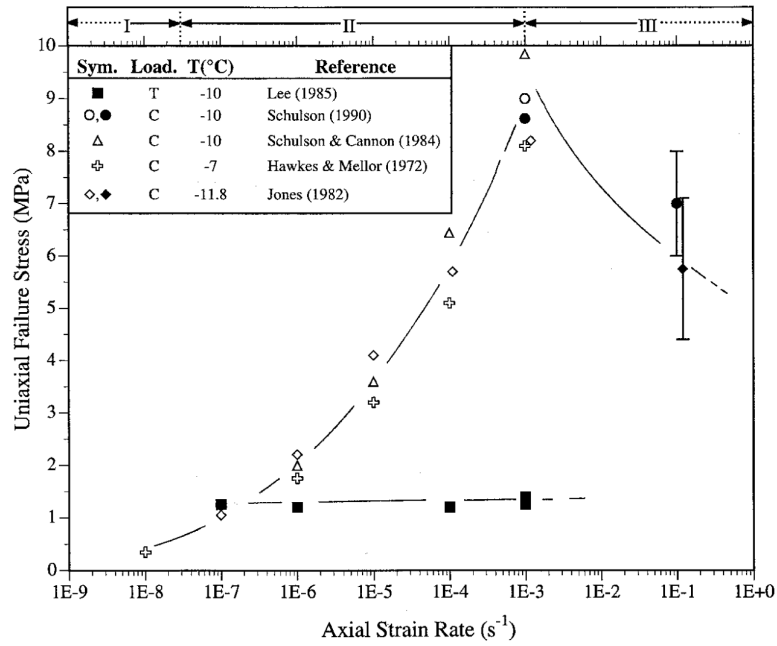
Rist; Murrell, 1994; R. E. Gagnon; Gammon, 1995; Melanson et al., 1999). Exemplary results of triaxial compression tests by Rist; Murrell (1994) are shown in Figure 2.5. In particular, at higher strain rates $\dot{\epsilon} \geq 1 \times 10^{-3} \text{ s}^{-1}$ associated with brittle failure under unconfined conditions, the peak shear stress increased with increasing hydrostatic pressure. In addition, a transition from brittle to "plastic" failure with increasing confining pressure was observed. Rist; S. J. Jones, et al. (1994) observed a volume conserving behaviour during shear fracture.

Based on experimental results and predictions C. E. Renshaw et al. (2014) has derived a detailed failure map for ice which describes different failure mechanisms in dependency of the strain rate and the confinement ratio R_c . The confinement ratio R_c is defined as the ratio of the least to the greatest principle stress. The failure map is presented in Figure 2.6. Unconfined ice like in a common uniaxial compression test fails by axial spalling at high strain rates. Under low respectively moderate confinement and higher strain rates ice fails by Coulombic faulting (C-faulting). At higher confinement the failure of ice will be dominated by plastic faulting (P-faulting). At low strain rates the failure is dominated in general by ductile behaviour. The failure map is completely consistent with the research shown before in this section. A comprehensive explanation axial spalling, C- and P-faulting is given in doctoral thesis of Golding (2011). C-faulting can be represented with the Mohr-Coulomb theory.

Not mentioned in the failure map of C. E. Renshaw et al. (2014) but also relevant in ice-structure interaction is the thermodynamic phase change from solid ice to liquid water (Riska, 2010). It can be expected, that for very high homologous temperatures the effect is of great significance, since the melting pressure continues to decrease with



(a) Stress-strain curves for tension and compression tests. I, II, III – low-, intermediate- and high- strain rates. The strain rate ranges are also provided in Figure 2.4b. The figure based on Schulson (1999). The tensile test photo was taken from J.H. Currier et al. (1983) and the compression tests photos from Fellin (2013), with permission from Springer Nature



(b) Tensile and compressive strength for equiaxed and randomly oriented freshwater ice of 1 mm grain size vs. strain rate in a relevant temperature range between $-7^{\circ}C$ and $-11.8^{\circ}C$ (Schulson, 1999; with permission from Springer Nature)

Figure 2.4.

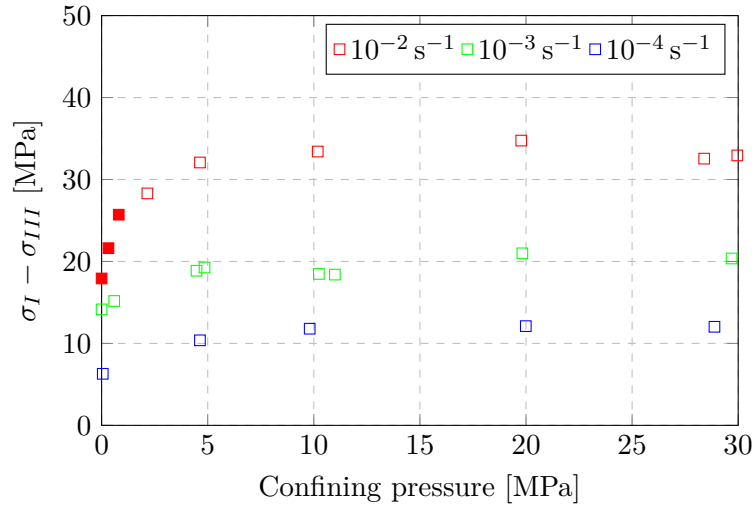


Figure 2.5.: Triaxial tests at different strain rates considering freshwater ice at -20°C . The peak shear stress is given. Solid symbols denote brittle-shear fracture, others ductile respectively plastic faulting (data according to Rist; Murrell, 1994)

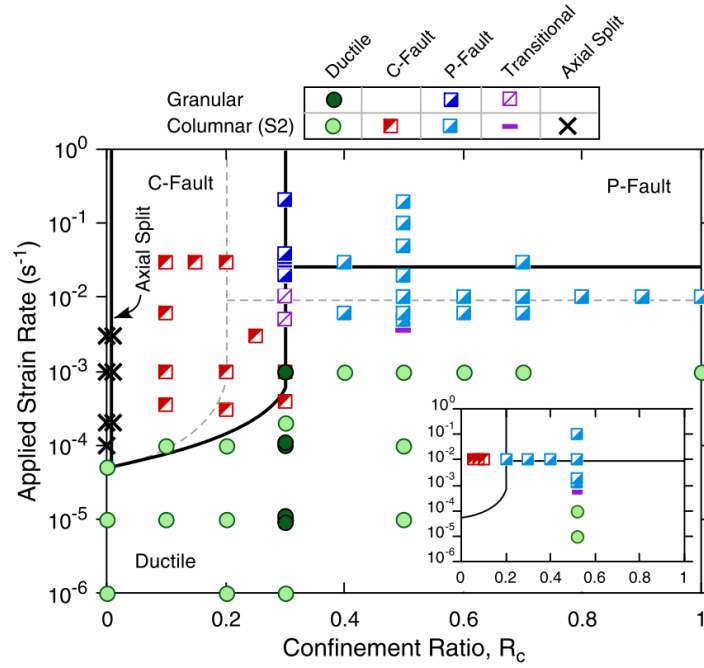


Figure 2.6.: Failure maps of ice in dependency of the applied strain rate and the confinement ratio R_c . R_c is defined as the ratio of the least to the greatest principle stress. Solid lines are transitions predicted for -10°C , dashed lines for -40°C . Experimental data from experiments of granular and freshwater ice at -10°C . Inset shows results for -40°C (reprinted from C. E. Renshaw et al., 2014; with permission from Elsevier)

increasing temperature. The temperature depended melting pressure according to Feistel et al. (2006) is given in Figure 2.7.

Kellner (2022) investigated the influence of parameters such as the global strain rate, ice temperature, grain size, porosity, type of ice, triaxiality and specimen geometry on the strength and transition behaviour (ductile/brittle failure) with machine learning as well as statistical tools. A key finding of the study was that confinement or stress triaxiality is a leading parameter for strength, while strain rate and temperature dominate the failure mode.

Although it can be assumed that during ice-structure interaction problems crushed and damaged ice plays a significant role. Unfortunately, only a very few studies treat the mechanical behaviour of crushed or damaged ice. During the triaxial tests of Rist; S. J. Jones, et al. (1994) in brittle mode damaged ice reveal the same elastic properties as intact ice. Stone et al. (1997) observed an increased creep rate of damaged ice for slow loading rates.

2.2. Ice-Structure Interaction

The two terms ice-structure and ship-ice interaction are not clearly defined in the literature. Hence, in this thesis the term ice-structure interaction is used for problems that consider only the interaction of the affected structure and the ice feature. The term ship-ice interaction, on the other hand, is used for the holistic problem including global motions, hydrodynamic and hydrostatic effects. In the following, the thesis will focus on ice-structure interaction problems with respect to a potential future ship-ice interaction application.

The basic requirement for ice loading is the collision of an ice feature with the hull of the ship. The relative speed, the impact position and the masses of the two colliding bodies together with hydrodynamic effects (added mass) determine the maximum energy available (Popov et al., 1969). The ice force itself resulting from the energy is determined by several hierarchical subproblems. First the ice force is limited by fracture (due to bending failure, splitting or buckling) away from the contact interface and second by crushing in the contact domain direct on the ship structure. "Crushing" is the common term for the brittle failure of ice into small particles (Riska, 2010). It is often accompanied by "Spalling". Spalling describes the process of large splinters forming at circumference of ice feature and reducing the contact area. Figure 2.8 presents a simplified sketch of the ship-ice interaction problem.

Fracture limits are e.g. dominating for inclined contacts under level ice conditions. In case of smaller ice floes and icebergs global bending failure is suppressed. Whereas for nearly vertical structures no significant bending loads occur in the ice and crushing is usually the limiting failure process.

Furthermore, there is an interaction with the ship structure possible. If the ship structure is weak, it absorbs a larger amount of the collision energy (Amdahl, 2019). Under certain circumstances significant elastic and plastic deformations of the structure can reduce the resulting accelerations of the ice feature and accompanying impact forces.

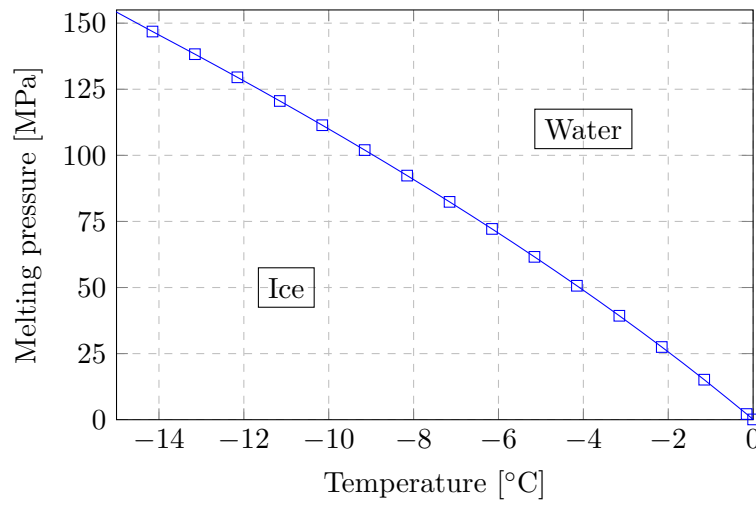


Figure 2.7.: Melting pressure curve of ice Ih (data according to Feistel et al., 2006)

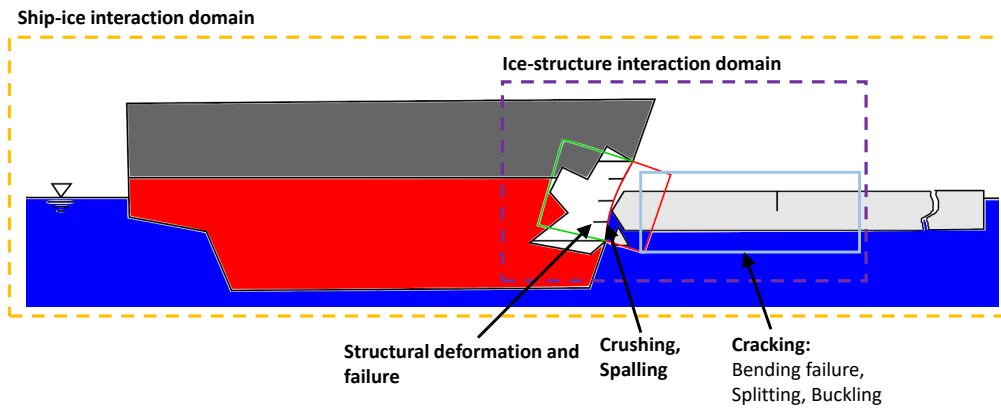


Figure 2.8.: Schematic sketch of a ship-ice interaction scenario

However, plastic deformation are non-reversible and only tolerable to a certain level. Ultimately, the ice force is limited by the collapse or rupture of the ship structure. This potentially dangerous scenario must be avoided during ship operation. A schematic summary of the multitude of influencing factors of ice-structure interaction for offshore structures is given in the ISO19906 (International Organization for Standardization, 2010). These influencing factors also essentially apply to ships.

A comprehensive understanding of the ice-structure interaction and in particular of the crushing and spalling process is necessary to access ice loads on a promote way, since these processes are ultimately limiting the ice load on the outer hull of the ship. Ice-structure interaction was subject of multiple studies and papers in the literature. A comprehensive review is given by Ian J. Jordaan (2001).

The ice-structure interaction process can be studied in:

- laboratory experiments, e.g. Lande Andrade et al. (2022), R. Gagnon et al. (2020), Määttänen et al. (2011), and Tuhkuri (1995),
- field trials, e.g. D. Masterson et al. (1993) and D. S. Sodhi (2001),
- or sea trials, e.g. ISSC (2015) and Suominen et al. (2017).

The foremost advantage of laboratory tests over sea trials are controlled test conditions, direct observations and the possibility to repeat tests easily (G. W. Timco; Sudom, 2013). During full-scale measurements the ice dimensions and properties are often not known, but measurements for long periods are possible, which are necessary to investigate the variation in the ice loading (Suominen et al., 2017). However, detailed investigations with the need of complex measuring technology, such as pressure sensitive foils, are often only possible in the laboratory. Also experiments with large ice induced structural deformations, until rupture, are hard to conduct at sea, without endangering the safety of the ship or offshore structure. These major advantages of laboratory tests are countered by problems such as geometric boundaries and limited load capacities and finally the transferability of the results to full-scale applications.

As observed in the compression test, ice also fails during ice-structure interaction in brittle manner at high velocities or ductile at low velocities (Wells et al., 2011; Määttänen et al., 2011; G. W. Timco; Sudom, 2013). Two exemplary load-time curves of an indentation experiment for brittle and ductile failure are presented in Figure 2.9. Ductile forces are characterized by predominantly continuous force curves, whereas brittle loads are dominated by load oscillations and sudden load drops. These sudden fluctuations are associated with spalling and extrusion of the crushed material (Ian J. Jordaan, 2001).

Standard tests such as the compression test allow the determination of physical meaningful engineering strain rates (test speed/specimen length). However, for real ice-structure interaction scenarios strain rates are difficult to determine, because of the often unknown ice geometry and the brittleness of the material with associated cracks. Therefore, the specification of a transition speed is helpful. The transition from ductile to brittle behaviour commonly takes place in the velocity range of 0.1 and 3 mm s^{-1} (G. W. Timco; Sudom, 2013; Herrnring; Kubiczek, et al., 2020). It can be assumed that

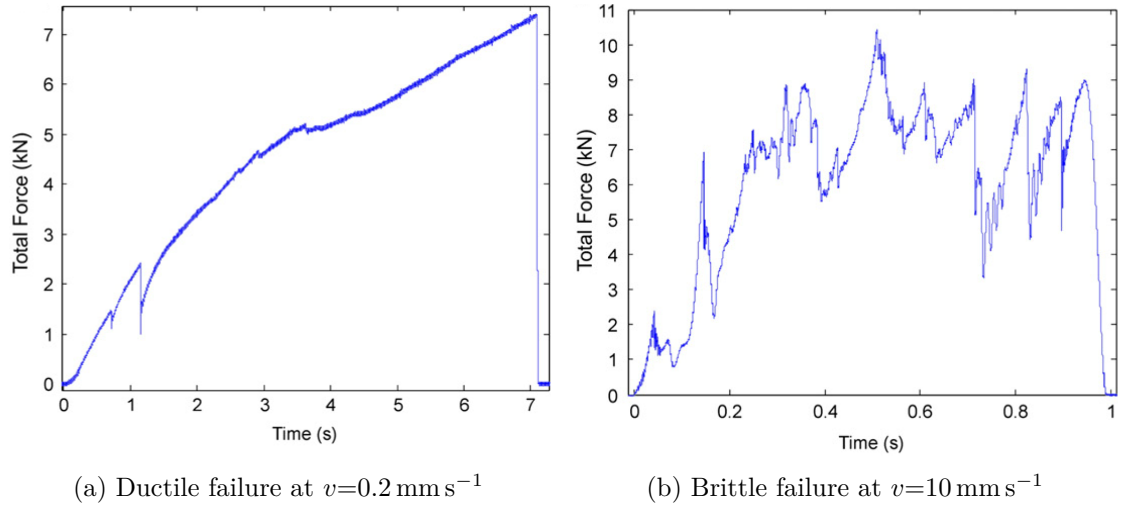


Figure 2.9.: Force time plots of ice indentation experiments at different velocities and an ice temperature of -10°C (reprinted from Wells et al., 2011; with permission of Elsevier)

moving ships are predominantly encountering brittle ice failure. Therefore, most of the existing research deals with brittle interaction problems.

First explanation approaches of brittle ice load fluctuations focused on the brittle failure mechanisms e.g. (R. E. Gagnon, 1999). According to the current knowledge, both fracture and continuums mechanical processes are important to explain the phenomena during brittle ice-structure interaction (Ian J. Jordaan, 2001; Wells et al., 2011; Browne et al., 2013). A comprehensive illustration of an ice-structure interaction process is presented in Figure 2.10.

Typically for brittle ice-structure interaction is the development of a damaged Layer in the center. Kurdyumov et al. (1976) assumed a constant thickness of the damaged layer and a viscous fluid like behaviour. Under extensive idealisations Kurdyumov et al. were able to compute the impact of a sphere in an intact ice surface. The concept was also adapted by Popov et al. (1969) for ship application.

During different field tests in the 1990s it was observed that even the pressure in the damaged layer is varying in spatial and temporal domain (Ian J. Jordaan, 2001). Impressions of exemplary ice pressure distributions are given in Figure 2.11. The uneven pressure distribution leads to so-called High Pressure Zones (HPZ), which are explained on the one hand by spalling and on the the other hand by cyclic hardening and softening of the damaged layer.

Several analyses have already shown that, especially in case of brittle failure, only a fraction of the nominal area is loaded. Takeuchi et al. (2001) measured during the JOIA project for brittle loads maximum contact ratios (loaded area/nominal area) below 35 %. Ductile problems interact on significant larger contact areas compared to brittle scenarios. In case of ductile failure Takeuchi et al. (2001) determined contact ratios up to approximately 90 %. The loaded area is also affected by the ice temperature (Riska,

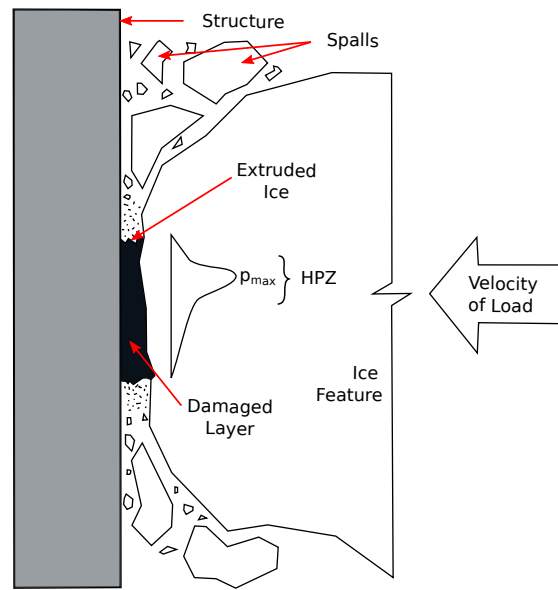


Figure 2.10.: Schematic illustration of the ice-structure interaction zone (based on Melanson et al., 1999; Ian J. Jordaan, 2001)

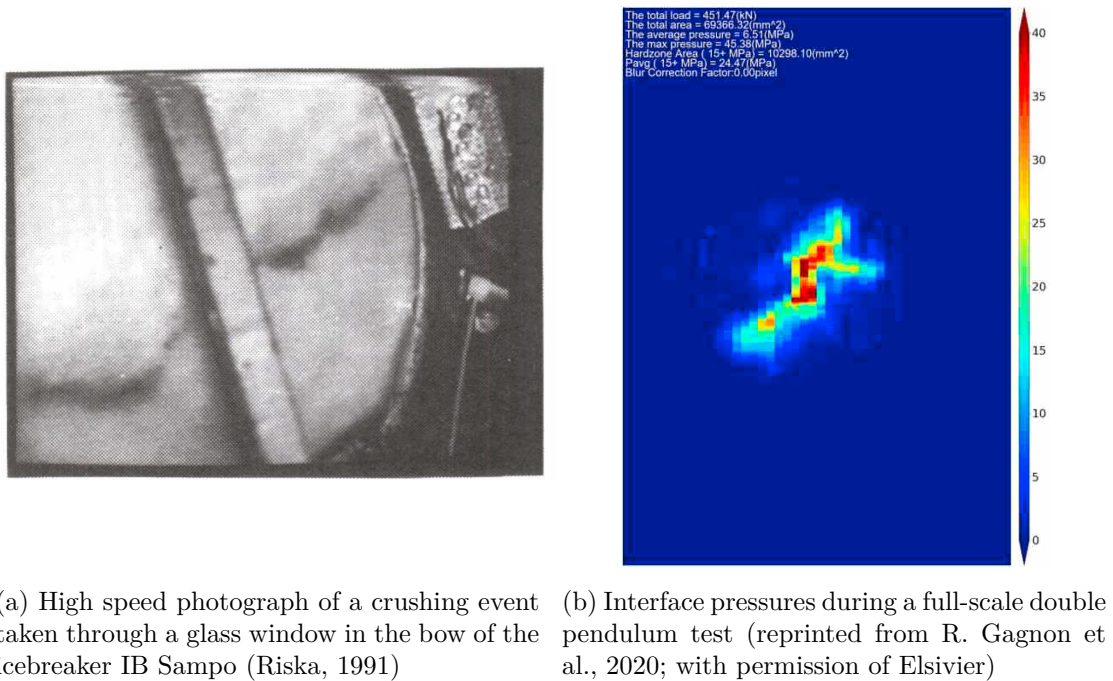


Figure 2.11.: Images of different ice-structure interaction processes

2022). As the temperature increases, the loaded area also becomes larger.

The processes during brittle ice-structure interaction are complex and not fully explained. The following is an attempt to compile the current state of knowledge:

- At the beginning of the ice-structure interaction process is a stress concentration in the area of the HPZ, which results from **spalling and fracture processes** (Mackey et al., 2007). For example Croasdale et al. (1977) and Frederking et al. (1990) observed that fractures under compression tend to propagate in the direction of the nearby outer surface.
- Behind the loaded interfaced respectively HPZ a **damaged layer** develops due to different processes which can result into a softening or hardening of the ice material:
 - **Microcracking** generally does not result a global failure of the specimen except at very low confinement (e.g. uniaxial conditions in combination with the wing crack mechanism) (Wells et al., 2011). Due to microcracking the material gets softer. Microcracking is mostly observed in low-confinement regions (Golding, 2011). Please refer also to Figure 2.12. In the figure, microcracking occurred during the test run at -15°C . It can be seen that less cracks appear at the highly confined center.
 - **Dynamic recrystallization** is a dissipative process of material reorganization that occurs through severe grain modification under high confinement and shear, resulting fine-grained ice (Wells et al., 2011; Golding, 2011). Dynamic recrystallization softens the material. This process is explained by "new" smaller undeformed grains with a c-axis predominantly arranged transverse to the sliding direction. (Burg et al., 1986; Fellin, 2013). Please refer also to Figure 2.12. In the figure, the smaller grains are clearly visible for the test run at -5°C .
 - **Sintering** of crushed material (Singh et al., 1996). The sintered material could also appear as fine grained ice comparable to a recrystallized grain structure (E. Kim et al., 2012).
 - During the **extrusion** process, the disintegrated material is ejected out of the high pressure zone (Wells et al., 2011). An experimental investigation and constitutive description by a Mohr-Coulomb model is given by Sayed et al. (1992) and Savage et al. (1992). Cyclic extrusion of softened and pulverized ice out of the damaged layer is called pulverization by some authors (Ian Jordaan; G. Timco, 1988). It is assumed that softening of the "damaged layer" and ice extrusion results into a cyclic load variation (compare Figure 2.13 – repeated crushing events).
 - During **pressure melting**, the phase change from solid to liquid phase takes place (R. E. Gagnon, 1994). Pressure melting is the ultimate form of extrusion (Wells et al., 2011). For freshwater ice at -10°C the phase change occurs at

approximately 110 MPa (compare Figure 2.7). Assuming the liquid water can escape out of the interaction zone, this value represents the upper bound of the achievable pressure during ice-structure interaction (Riska, 2010). However, there must be an almost perfect confinement to achieve this value.

The final resulting ice force is determined by the "weakest" process. The leading failure mechanism differs depending on the contact situation.

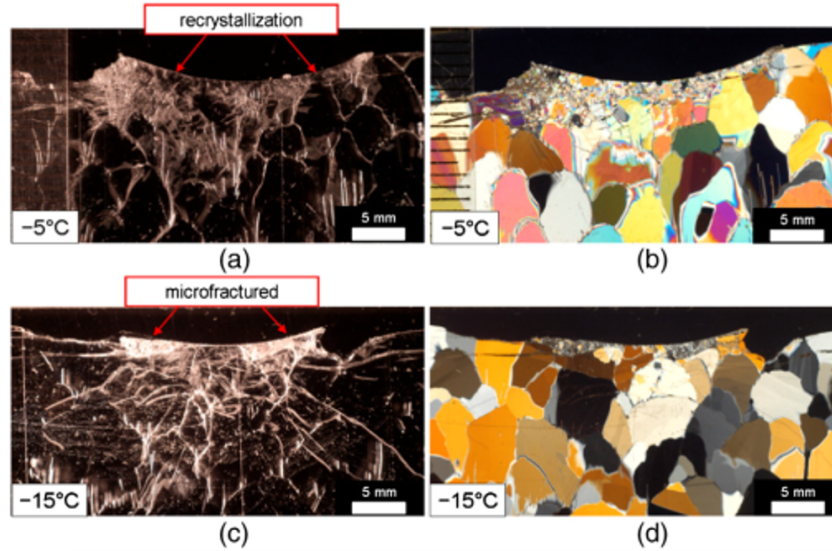


Figure 2.12.: Thin sections of a damaged layer during an indentation test with a compliant structure at a cylinder velocity of 4 mm s^{-1} ; (a) and (b) at -5°C and (c) and (d) at -15°C . Thin-section photos on the left were taken with side-lighting to show the fracture surfaces and on the right with cross-polarized lighting to visualize the grain structure. At -5°C the ice failed in ductile mode, whereas at -15°C brittle failure was observed (reprinted from Browne et al., 2013; with permission of Elsevier).

The ice-structure interaction process described so far, does not apply for ice collisions where the ice perfectly contacts the structure over a wide area during the first contact. In this case the failure behaviour of the ice feature is comparable to an uniaxial compression test and will not occur predominantly by crushing. Spalling and global shear faults (C-faulting) are dominating (Croasdale et al., 1977; Frederking et al., 1990).

Detailed ice pressure measurements are realized by different authors (D. Sodhi et al., 2006; Määtänen et al., 2011; R. Gagnon et al., 2020). In many cases, the I-Scan pressure measurement system of the company TekScan was used (D. Sodhi et al., 2006; Määtänen et al., 2011; Ziemer, 2019). Because of the non-linear sensor behaviour, the calibration of the I-Scan system is challenging (Brimacombe et al., 2009). R. Gagnon et al. (2020) developed an own pressure measurement system.

Apart from the accuracy problems, the evaluation and interpretation of pressure measurement data is challenging. Johnston et al. (1998) already proposed a distinction

between "background" pressures and "active" pressures. A critical pressure of 2 MPa was proposed to distinguish between active and background pressures. R. Gagnon et al. (2020) used differently a HPZ definition according to:

- High pressure zone > 15 MPa
- Low pressure zone < 15 MPa

As shown in experiments with test speeds near to the transition velocity frequently fail alternating in ductile and brittle manner. Therefore, these experiments are well suited to identify and describe different failure mechanisms. A classification was made by Wells et al. (2011). The classified force-time curve is presented in Figure 2.13.

Due to the high complexity of ice-structure interaction process, only isolated sub-problems could be simulated fully physically based so far. Examples are wing-crack (Kolari, 2017) or creep models (Xiao, 1997; Schulson; Duval, 2009). However, these specialised models are not suitable for the description of the holistic ice-structure interaction process.

A purely empirical approach to describe ice-structure interaction is the pressure-area relationship (Palmer et al., 2009). Sanderson (1988) collected the data of different sources in a comprehensive plot where the maximum nominal pressure plotted against the associate contact area. Thereby, the ice pressure decreases with increasing contact area. As an example, the pressure-area plot of three measurement campaigns on different ice breakers is presented in Figure 2.14. For the design of offshore structures the pressure-area relationship is included in the ISO 19906, based on a best fit against experimental data and an increase of 3 standard deviations (International Organization for Standardization, 2010; D. M. Masterson et al., 2007). A comprehensive review and re-evaluation on pressure-area effects was submitted by G. W. Timco; Sudom (2013). The publication clearly distinguishes the following two types of pressures:

- **Global pressures:** The global force is divided by the projected total contact area of the ice feature on the structure.
- **Local pressures:** The global force is divided by the actual contact area. The contact area could be assumed or measured.

G. W. Timco; Sudom (2013) concluded that the Sanderson pressure-area plot is generally useful. However, to answer individual questions on ship-ice interaction or the design of offshore structures comparable data subsets should be used. G. W. Timco; Sudom (2013) proposed in respect to offshore structures several curves for different interaction speeds and contact geometries.

Basically, similar thoughts are presented in Figure 2.15. Based on Johnston et al. (1998), this figure postulates various factors influencing pressure-area curves. Johnston considers the confinement effect and the shape of the ice feature to be the most important. This illustration is still highly relevant and provides a good impression of the complexity to determine meaningful ice-pressures. Furthermore, the figure shows that

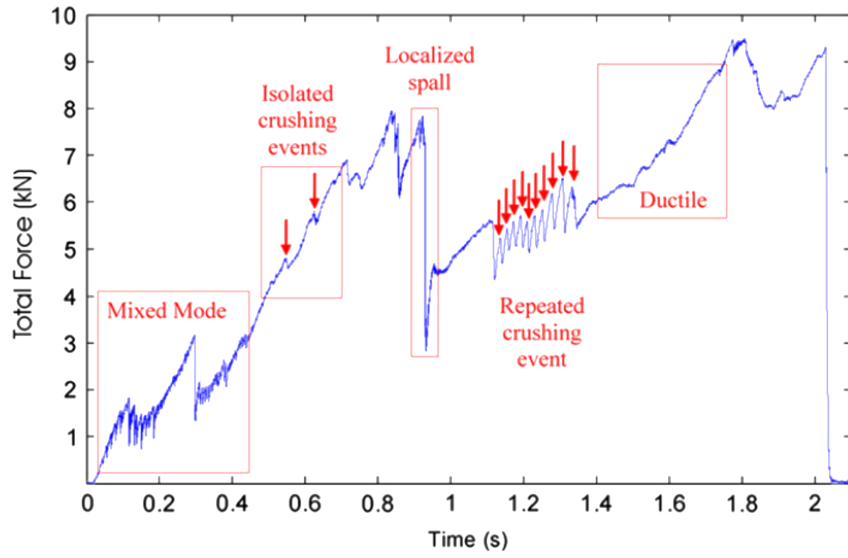


Figure 2.13.: Force time plot of an ice indentation experiment with classification of different failure behaviours. In case of multiple repetitions of a specific failure behaviour (e.g. localised spalls), only one representative example is highlighted (reprinted from Wells et al., 2011; with permission of Elsevier).

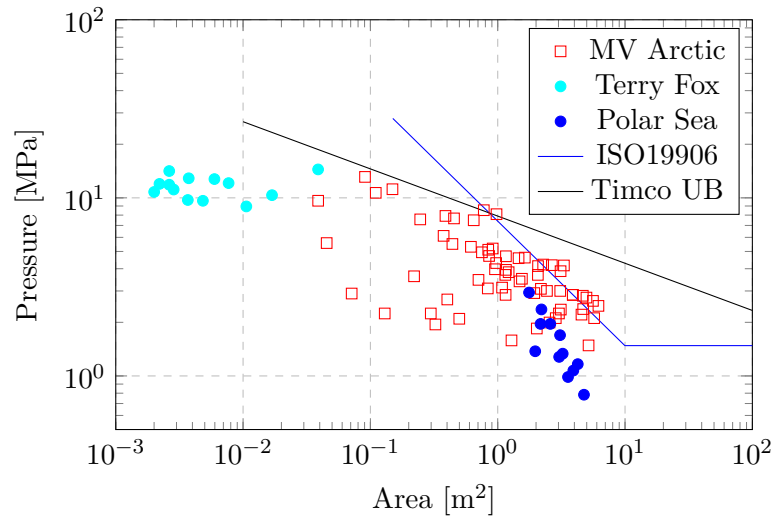


Figure 2.14.: Pressure-area plot showing the highest value of the “process-area” curve during different ship measurement campaigns. In addition the design pressure-area of the ISO19906 (International Organization for Standardization, 2010) and the upper bound curve for isolated ice floe impacts (G. W. Timco, 2011) is given (based on G. W. Timco; Sudom, 2013 and extended with MV Arctic data given by Ian Jordaen; C. Li, et al., 2005)

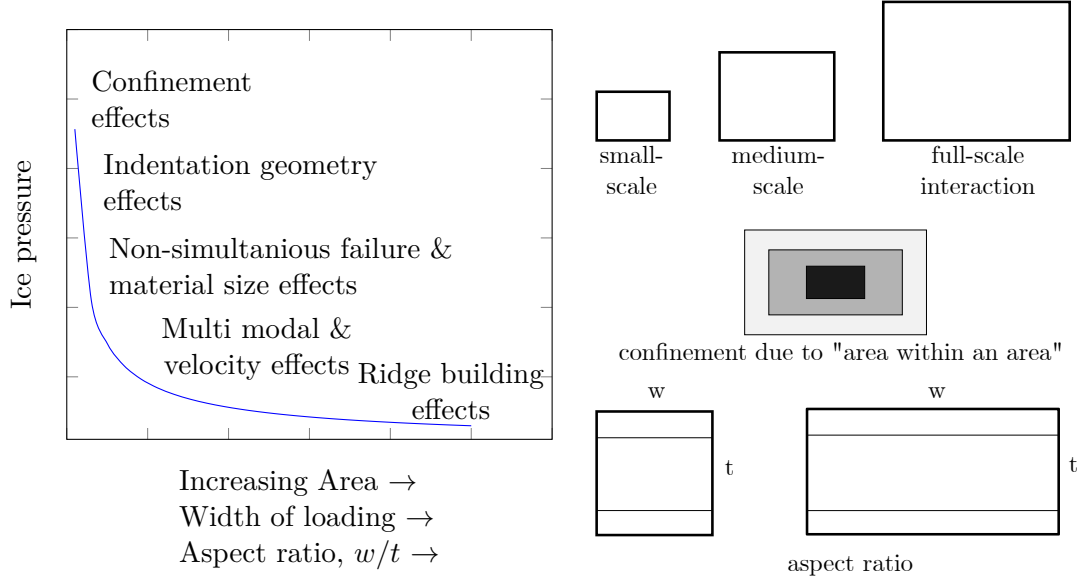


Figure 2.15.: Possible explanations for pressure–area effects (based on Johnston et al., 1998).

similar relationships exist for the ice pressure in dependency of the aspect ratio or width of loading.

Moreover, the influence of the structural feedback on the ice pressures has been studied by Browne et al. (2013), Määtänen et al. (2011), and Amdahl (2019). In particular, Browne et al. (2013), concluded that the frequency of the load variation increases with structural stiffness and speed in brittle mode. Until now in most considerations the structure has been idealized as rigid (Palmer et al., 2009), although an influence of structural deformation on the ice loads cannot be entirely excluded. Amdahl (2019) postulated three different domains for ice collision scenarios. Depending on the structural deformation/stiffness the collision energy will be dissipate into the ice (strength domain), the structure (ductile domain), or both (shared-energy domain).

2.3. Ice-Structure Interaction Simulations

The finite element method (FEM) represents the state of the art in structural design (Nowacki, 2010). The potential of using FEM for the simulation of ship-ice interactions has been a significant topic of research over the recent years (Sazidy, 2015; H. Kim et al., 2015; Ince; Kumar; Park, et al., 2017; Yu et al., 2021). Arguments in favour of using FEM is the maturity and accuracy for continuum mechanics problems. In addition, commercial solvers such as LS-Dyna or Abaqus explicit are well suited to handle large non-linear structural models and complex contact problems.

Potential applications of the FE method include the analysis of hull structural response and strength characteristics, either of new or existing designs, with the aim to

determine appropriate operational limitations or consequences of an accidental impact, among others. In general, there are three concepts to consider ice loads in FEM-based models:

1. **Non-coupled pressure mapping approaches:** In this approach, ice loads are modelled in terms of a priori determined pressures corresponding to the considered design load cases (e.g., as specified by class rules (Finnish Transport Safety Agency, 2017; International Association of Classification Societies, 2019) or empirical pressure relationships (Quinton et al., 2012)). The pressures are mapped onto the structure being analysed. This approach is numerically cheap and robust. It is the industrial standard in structural design.

However, this concept does not consider the interaction between the ice loading and the resulting structural response (Quinton et al., 2012). As a result, depending on the applied load assumptions, there is a risk to obtain flawed structural failure modes. Since there is no coupling between ice and structure, the approach is not suitable for problems with large structural deformations or failure.

Ice rules and common pressure-area based approaches assume constant ice pressures. Spatial and temporal varying HPZs, which are typical for brittle ice loads (R. Gagnon et al., 2020), are neglected. From a structural mechanical perspective, the assumption of a constant pressure is non-conservative (Erceg et al., 2014). Consequently, a constant ice pressure may result in underestimation of the resulting structural deformations or an inaccurate reproduction of the structural failure modes.

2. **Weakly-coupled approaches:** Weakly-coupled approaches represent an intermediate solution between non-coupled and fully coupled approaches. The ice loads are idealized and computed during the run time of the FEM simulation by a separate and efficient algorithm. The ice forces and pressures are often determined based on pressure-area relationships and equations of motion for the ship and the ice feature; see for instance Kolari; Kurkela (2012).

Potential applications include analyses of collisions with e.g. ice floes or icebergs. Since the weakly coupled approaches also assume mostly a constant pressure, the disadvantages already mentioned for the pressure mapping approaches essentially apply. Due to the generally high degree of idealization of the ice-load model, these approaches are even not well suited to handle large plastic deformations and failure of the structure.

3. **Fully coupled approaches:** In fully coupled approaches, the ice feature and the ship structure is solved in a single FE model to achieve a detailed representation of the involved ice forces and pressures. Some models address also hydrostatic and hydrodynamic effects. The particular challenge is to find a suitable ice model. As discussed before, the mechanical behaviour and many processes related to ice-structure interaction occur very locally and are not fully explained. Fracture and continuum mechanic processes take part at the same time and weaken the ice

behaviour globally. Locally also hardening effects could be observed. Several ice models of fully coupled simulations for different applications have been presented in the literature:

- a) **Global ice load models:** The aim of these models is to compute the correct ice induced global forces on offshore structures or ships. Such simulations often include large calculation areas and empirical or semi-empirical low fidelity methods. The correct contact pressure distribution is not the objective of these simulation approaches. Therefore, the ice is discretized with only a few elements in the thickness direction. Examples for these types of models are the coarse Cohesive Zone Models of Gürtner (2009) for offshore structures and Wang et al. (2019) for ships.
- b) **Local load or design load models:** The aim of these models is the correct representation of ice forces and pressures in full-scale. Since the correct simulation of the structural behaviour is the core objective, the ice behaviour is idealised to enable a numerically efficient solution. Despite the weakness that FEM can only represent discontinuities with difficulty, it is still the most widely used approach for ice-structure interaction simulations. The simplest models assume elastic or rigid ice behaviour. These models are applicable to simple ice geometries, e.g. a large sphere, where the primary concern is a conservative estimation of the structural deformation resulting from the ice impact. However, the assumption of a rigid or elastic material behaviour will be much too stiff in case of a general ice body with a significant amount of crushing and spalling.

Plastic approaches are another possibility. First plastic ice models are given by e.g. Ralston (1977) and Derradji-Aouat (2003). An application example of a plasticity model in respect to ships is the iceberg design load model of Liu et al. (2011). The model was recently applied by Yu et al. (2021). In this model a pressure dependent Tsai-Wu yield surface based on the results of Derradji-Aouat (2003) is utilized. Temperature- and strain rate effects are considered. Iceberg material models are not applicable in general, since splitting and spalling are not considered.

Mainly for the investigation of flexural failure dominated ice-structure interaction Sazidy (2015) proposes a plasticity based model consisting of two simple material models in LS-Dyna. Also hydrostatic effects are considered. However, the von Mises plasticity used does not represent the pressure dependence for compressive failure.

A further very common approach in ice modelling is the use of crushable foam models (R. E. Gagnon, 2011; H. Kim et al., 2015). The crushable foam models achieve reasonable results with respect to global loads. Nevertheless, the transferability of the model and the determination of the input curves are challenging.

A possibility to represent failure and preserve the volume is the before men-

tioned Cohesive Zone Method (CZM). Ince; Kumar; Paik (2016) developed the KOSORI constitutive ice model and applied it to ship-like structures (Ince; Kumar; Park, et al., 2017). However, the CZM is numerically expensive and has considerable disadvantages, such as stability issues, artificial compliance and a loss of mass and energy due to the erosion of the cohesive elements (Herrnring; Kellner, et al., 2018).

- c) **Physical correct models:** Complex physically based models already exist for selected and specific academic problems. Examples are Representative Volume Models (Kolari, 2007; Elvin, 1996), Phase Field Models (Schneider et al., 2016), Full Field Models (Grennerat et al., 2012; Suquet et al., 2012) or in certain cases Cohesive Zone Models (Kellner; Wenjun Lu, et al., 2021). Due to the high computational effort and the high degree of specialization, these models are not yet suitable for the simulation of full-scale ice-structure interaction problems.

An open question in FEM is the treatment of failure. The failure of ice is mostly investigated with the element erosion technique. However, if ice is simulated under compression, the element erosion technique leads to non-physical results, because the actually existing ability of damage material to transmit loads is lost. Furthermore, the elemental erosion technique violates the mass and energy conservation (Gürtner, 2009; R. v. Bock und Polach et al., 2013).

As an alternative to the FEM based approaches, there are a variety of mesh-less methods in the literature for simulating brittle problems (Oñate et al., 2011). In this thesis the commercial FEM code LS-Dyna is utilized. LS-Dyna R11.1.0 includes besides the FEM different mesh-less solvers which are applicable to brittle or semi-brittle problems, e.g. Bounded Discrete Element Method (Amiri, 2018), Peridynamic (Bobaru, 2020; Wei Lu et al., 2020), Smooth Particle Galerkin (Wu et al., 2018) or Smooth Particle Hydrodynamics (Sato et al., 2013). However, no mesh-less approach has yet been proven to be generally applicable for brittle problems (Tabiei et al., 2016). In the author's experience, there are major difficulties in simulating the ice self-contact, as the focus of most mesh-less methods is tensile dominated failure, without considering closed crack surfaces.

3. Experimental Analysis

The detailed review of the state of art shows, that there is differently to the basic ice failure behaviour no schematic and holistic investigation of influencing parameters on the spalling and crushing process existing. Experimental concepts for a continuous investigation of the ice failure process at a significant load level were missing.

Therefore, an extensive series of experiments of small and large-scale ice-structure interaction tests were conducted to create a comprehensive and consistent dataset of experiments and gain a deeper insight into the ice crushing process. According to section 2.2 relevant parameters like the test velocity, confinement, specimen size and geometry are investigated in the test campaign. By comparing the experimental results of similarly shaped specimens in three different scales, the scalability of ice loads was analysed. The experimental data is further used for the development of a novel physical founded numerical ice model in chapter 4.

The experiments were carried out in the laboratory of the Institute for Ship Structural Design and Analysis of Hamburg University of Technology. Since the ice specimens size is limited in the laboratory, a novel solution had to be found to artificially constrain the ice and realize high loads. Furthermore, not even a single failure event but a continuous crushing process should be investigated. According to the requirements, the ice extrusion tests were developed, realized and conducted together with Jan Kubiczek. During the ice extrusion tests, a cylindrical ice specimen is pushed out of a confining pipe against a quasi-rigid or deformable test structure with a displacement-controlled servo hydraulic piston. A principle sketch of the ice extrusion test is given in Figure 3.1.

The test set-ups of the ice extrusion test for the three different specimen sizes are explained in section 3.1. In order to visualize and measure the ice pressures acting on the structure as accurately as possible, the I-Scan pressure measurement system of the company TekScan was used. Major opportunities, limitations and strategies for calibrating the TekScan system applied in this thesis are presented in section 3.3. In the following section 3.4, the results of the ice extrusion tests with 100 mm and 200 mm and 800 mm specimens against quasi rigid structures are described. To generate validation data for ice-structure problems with large structural deformations the tests were also conducted against deformable ship-like panels in full-scale. The according results can be found in section 3.5.

The results of the 100 mm and 200 mm ice extrusion tests (Herrnring; Kubiczek, et al., 2020) and the utilization of I-Scan for ice pressure measurements (Kubiczek; Herrnring, et al., 2022) have already been published. Parts of the following chapter were prepared on the basis of the mentioned publication, but re-evaluated and extended by the large-scale tests with 800 mm specimen diameter.

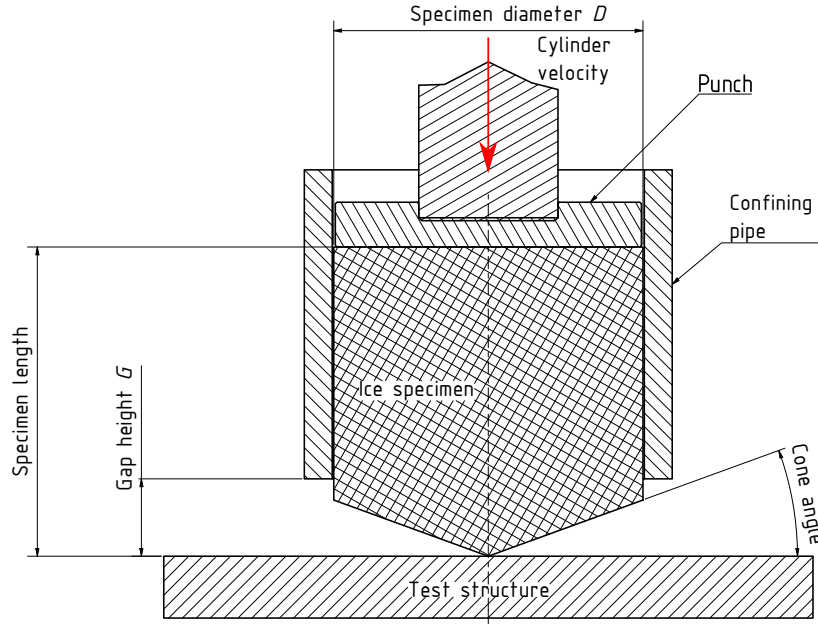


Figure 3.1.: Principle sketch of the ice extrusion test. In addition the investigated ice geometry and test parameters of the following test campaign are shown

3.1. Test Set-ups of the Ice Extrusion Tests

Three different ice specimen sizes were tested. The sample diameters D were 100 mm and 200 mm in small-scale as well as 800 mm in large-scale. The ice extrusion test concept is similar with the wedge shaped laboratory experiments of Tuhkuri (1995).

The test set-up for the small-scale 200 mm tests is shown in Figure 3.2 and Figure 3.3. The small-scale tests were conducted in a cold room at approximately -10°C . The maximum load capacity of the hydraulic cylinder in small-scale was 1.3 MN. The only difference between 100 mm and 200 mm set-up is a punch and confining pipe according to the specimen diameter.

Transferring to the actual ice-structure interaction problem, the confining pipe represents the unbroken surrounding ice and prevents, depending on the gap height G , the radial clearance of the load-bearing ice material in the centre. The gap height is the distance between the test structure and the confining pipe (compare Figure 3.1). The concept of the ice extrusion test should enable the investigation of high ice loads with a relative small test rig size, which otherwise only occur in case of larger ice feature dimensions. In small-scale the gap height were adjusted with threaded rods.

The large-scale tests with 800 mm diameter were conducted on the large structural test rig of the institute with a maximum load of approximately 4 MN. Due to the size of the experimental set-up, cooling of the environment and the structure was not possible. The quasi rigid and deformable test set-up for the large-scale ice extrusion tests is presented in Figure 3.4 and Figure 3.5. For the quasi rigid set-up a pre-existing very stiff mounting

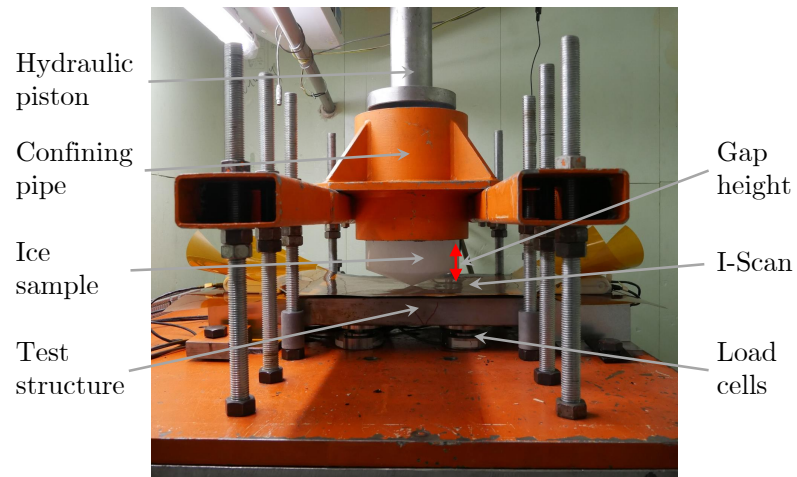


Figure 3.2.: Experimental set-up of the ice extrusion test with a 200 mm specimen



Figure 3.3.: The used test rig and cold room for the small-scale tests with 100 mm and 200 mm specimens. In contrast to the actual test set-up used, the picture shows a 160 kN cylinder. The 1.3 MN cylinder used during the tests can be seen dismounted to the left of the 160 kN cylinder

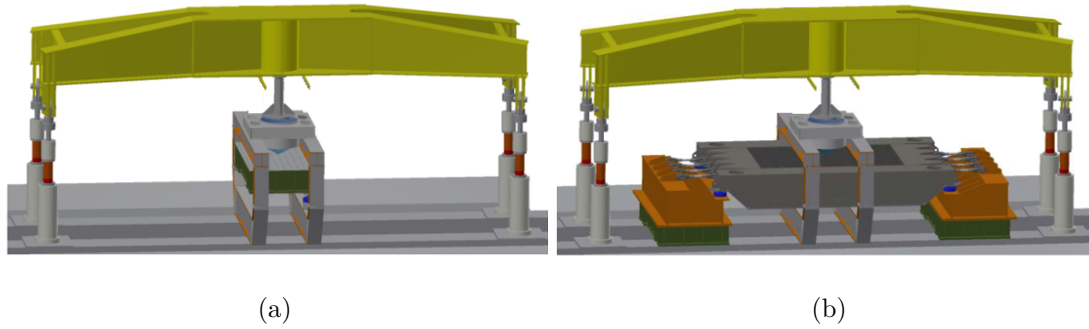


Figure 3.4.: CAD model of the ice extrusion test set-up with 800 mm specimens against a quasi rigid (a) and deformable test structure (b)

plate with a top plate thickness of 50 mm was used. In the deformable case the three tested ship-like panels according FSICR IC (Finnish Transport Safety Agency, 2017) were produced and welded into a surrounding stiff frame. Production and installation of the panels was realized by the yard "Theodor Buschmann GmbH & Co. KG" in Hamburg. Since only a purely ductile test was carried out on the third panel, the test will not be discussed further in this thesis.

The design of the surrounding frame and the test set-up was similar to Martens (2014) and Schötteleindreyer (2015), which conducted various ship collision experiments. The plate thickness of both considered panels was 10 mm. The frames were realized with flat bars in a dimension of 240 x 12 mm. The panels were built out of common construction steel S235JR. The two tested deformable structures with six (Panel 1) and five (Panel 2) frames are given in Figure 3.6. Due to different frame arrangements, the ice sample impacts centrally in the plate field in case of Panel 1 (Figure 3.6a) and directly on the frame in case of Panel 2 (Figure 3.6b).

Independent of the sample size, for a successful conduction of the ice extrusion process the confining pipe for the ice must be as rigid as possible. Therefore, in small-scale a 18 mm and in large-scale a 30 mm thick confining pipe was used. The inner surface of the confining pipe was machined and coated with a self-adhesive Teflon foil (producer: Böhme-Kunststofftechnik GmbH & Co. KG, Büchen, Germany) to reduce the friction between the ice and the pipe. The foil was inspected after each test and replaced in case of damage.

The total force was measured by load cells under the test structure. In addition, the cylinder displacement and the ambient temperature were always measured during the tests. More sensors added as needed. Since these were not considered within this thesis, they will not be introduced further. Data acquisition was performed with a Gantner Instruments Q.raxx multi channel data acquisition system.

Additionally the I-Scan pressure measurement system was used. The thin foil sensors are placed on the test structure. To protect the sensors against damage, water and shear



Figure 3.5.: Experimental set-up of the large-scale ice extrusion test for 800 mm specimens without confining pipe

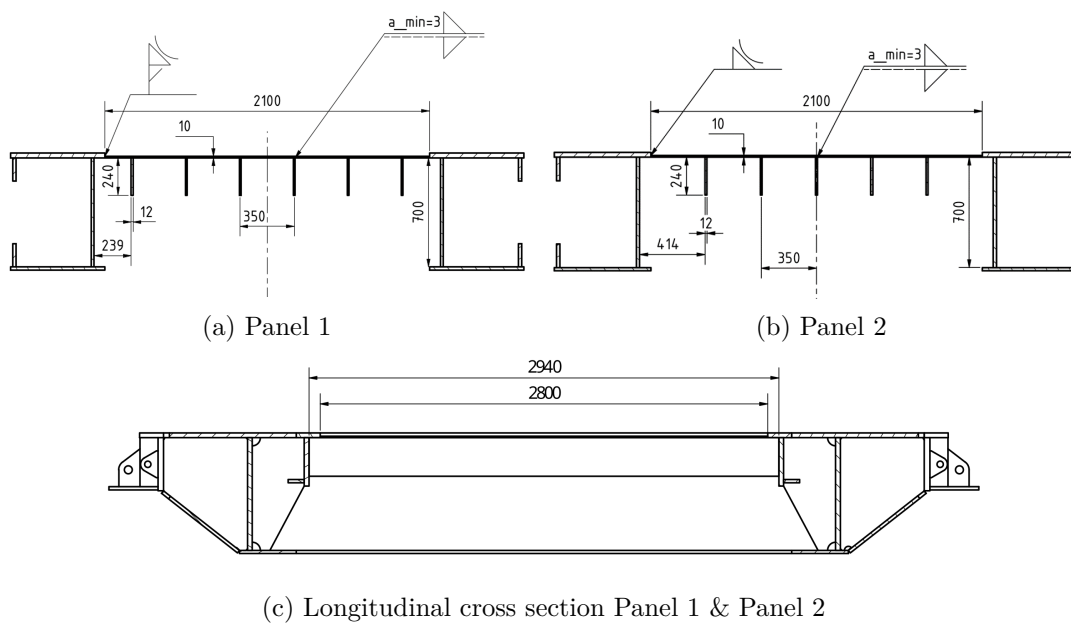


Figure 3.6.: Cross sections of the deformable test structures. The panels are designed according to FSICR IC

forces the I-Scan sensors were covered from both sides with Kapton HN500 polyimide foils. The top and the bottom foil were taped together all around with double-sided adhesive tape. The Kapton foil has absolutely proven itself for the protection of the sensors. In case of the small-scale experiments the Kapton foil was able to withstand more than 100 tests without significant damage. A detailed explanation of the system, investigation of the sensor behaviour and calibration are given in section 3.3.

3.2. Ice Production and Ice Properties

Within this thesis laboratory produced ice specimens were used. The advantage of laboratory produced ice samples is the possibility of repetition and year round availability. Unlike for natural ice, the freezing history and production process of laboratory produced ice is known. After different initial tests of granular and columnar ice (Härer, 2019), it was decided to use exclusively granular freshwater ice for the ice sample production. The reasons for using granular ice were, on the one hand, to achieve the most isotropic material behaviour possible and, on the other hand, the freezing of similar samples of different sizes seemed easier to realize with granular ice.

Usually, granular samples are prepared from an ice-water slurry (Cole, 1979). The production technique used in this thesis is comparable to Gudimetla et al. (2012). Whereas, deviating to Gudimetla, in this study directly commercial crushed ice (supplier: Eiswerft e.K., Glindede, Germany) was mixed with water.

All ice samples were frozen in a cold room at approximately -10°C . Pipes with the final diameters were used as a mold for freezing. The pipes are sealed at the bottom by adding a metal plate. The metal plate enable a high heat flux at the bottom while the top and the lateral surface of the specimens were insulated. The resulting mostly uniaxial freezing direction reduces stresses due to phase change and the air entrapment (Cole, 1979). The whole production process using the example of an 800 mm specimen is shown in Figure 3.7. The cylindrical molds for the small-scale samples were manufactured out of standard PVC-U pipes, whereas a customized steel mould was used for the 800 mm diameter samples. The steel mold was laterally insulated with Armaflex (a closed cell elastomeric foam). In the case of the much smaller PVC-U pipes no additional laterally insulation was necessary to obtain a macroscopic crack-free ice (compare Figure 3.8).

The sample preparation was carried out as follows: At first the stored 10 kg bags of crushed ice were re-crushed to avoid lumps of crushed ice particles. This was done with a self-constructed ice crushing machine. Afterwards, the crushed ice was added to the demineralised water previously poured into the ice mold with a final ratio of 2:1. During the addition of the ice the slurry was continuously stirred. Stirring reduces the amount of entrapped air bubbles (Cole, 1979), prevents clumping, and distributes the material uniformly in the mould. Before covering the specimens with insulation material (Styrodur plates), the mixture was compacted once by hand and water was removed or added as needed. For the large-scale ice specimens the freezing takes between 2 and 3 weeks, whereas the freezing of the small-scale samples takes around 2 days. Samples that were frozen at lower temperatures showed considerably more internal cracks, therefore

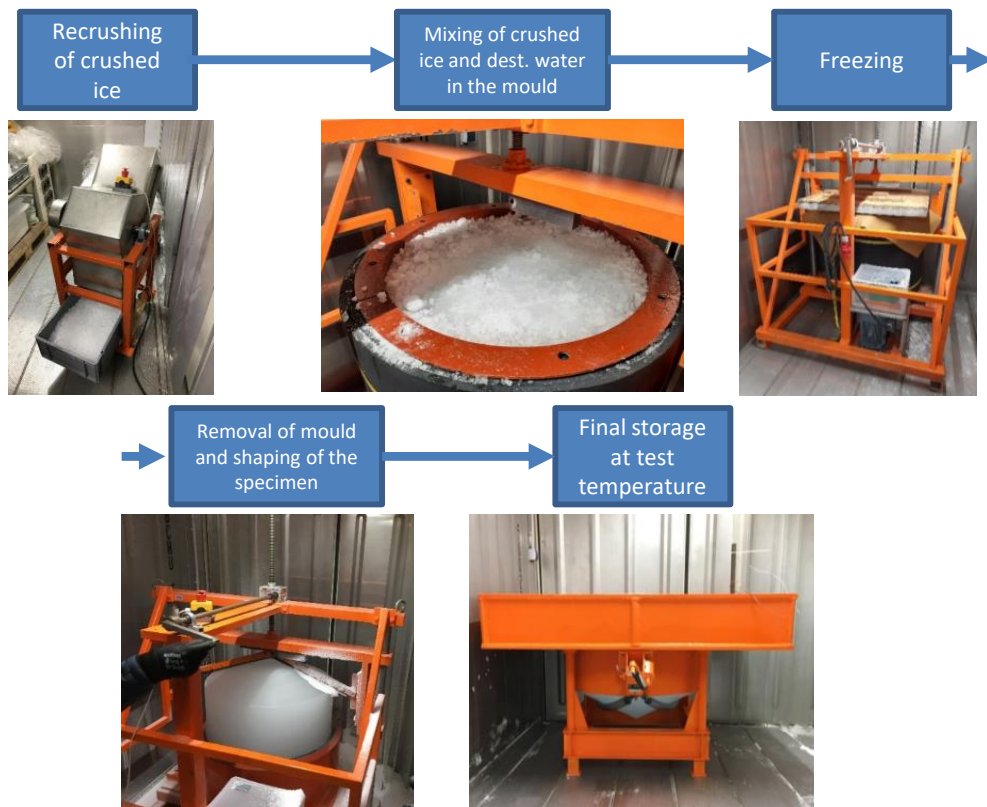


Figure 3.7.: The general ice production process with images of 800 mm specimen



Figure 3.8.: 200 mm specimens during freezing

the long freezing times were accepted for the large samples.

After the samples were fully frozen, the moulds of the small-scale samples were removed by moderate heating outside the cold room. Unlike the small-scale samples, the mould of 800 mm specimen was separable to allow the removal without heating in the cold room. Hereafter the specimens have to be machined to achieve the final dimensions of the test geometry. This was done with a mitre band saw and/or a self-constructed ice coning machine, which was also developed and manufactured specially for the ice extrusion experiments. At the end and regardless of the sample size, the specimens were stored in a refrigerated container for at least one night prior to testing to ensure a stable ice temperature of approximately -10°C .

Based on individual evaluations of thin sections a typical grain size between 2 mm and 4.5 mm was determined for the used ice. The grain size was determined by linear intercept method (ASTM International, 2013). Exemplary thin sections for a small-scale and a large-scale ice sample before testing under cross polarized light are shown in Figure 3.9. Both textures are granular. The average grain size was 2.6 mm for the 200 mm and 3.8 mm for the 800 mm sample. A possible explanation for the significant deviation of both grain sizes could be the considerably longer freezing time of the 800 mm sample.

The density of the ice was determined for the first two large-scale tests. Before testing a density of 902.86 kg m^{-3} for the test Cone800_G230_A30_V4_1 and 895.91 kg m^{-3} for test Cone800_G230_A30_V04 was measured.

In addition to the simple production process, freshwater ice also has the advantage that, it has a relatively high strength. Stephen J. Jones (2007) concluded that the strength of iceberg ice at -10°C is 3 times less compared to freshwater ice at a strain rate of $1 \times 10^1\text{ s}^{-1}$. At $1 \times 10^{-3}\text{ s}^{-1}$ still a difference of 1.7 was observed. Whereas in ductile mode for very low strain rates less than $1 \times 10^{-6}\text{ s}^{-1}$ no difference was found. Therefore, it can be assumed that freshwater ice is a conservative worst case scenario.

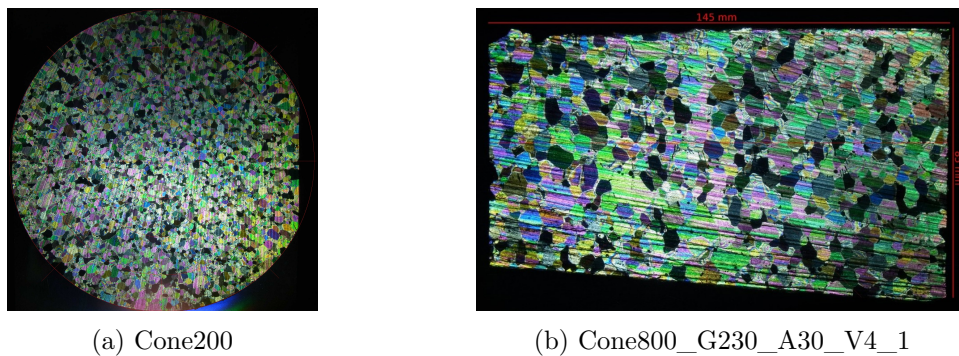


Figure 3.9.: Thin sections of a 200 mm and 800 mm specimen under cross polarized light

3.3. I-Scan Pressure Measurements

In the experimental campaign, not only forces but also the ice-induced pressure distributions on the structure were evaluated and used for validation of the proposed ice model. To measure the pressure distribution and the actual contact area, the tactile pressure measurement system I-Scan of the company TekScan is used. The I-Scan system was frequently used by different authors e.g. (D. S. Sodhi, 2001; Määttä et al., 2011; Browne et al., 2013; Ziemer, 2019) for ice pressure measurements, as the foil sensors are thin, flexible and easy to use.

In this study the I-Scan sensor 5101 (sensing area: 111.8 mm x 111.8 mm) with a pressure range of 3000 PSI (20.68 MPa) was used for the small-scale experiments. The 7105 sensor (sensing area: 528.3 mm x 447.0 mm) with a pressure range of 300 PSI (2.68 MPa) was utilised for the large-scale tests. Unfortunately, no pressure range greater than 300 PSI is offered for the 7105 sensors by TekScan. However, the low pressure range was compensated by reducing the sensitivity of the sensor (reduction of the supply voltage).

In case of the 200 mm and 800 mm specimens, four sensors each were connected together in a so-called Q-map to record the entire contact area. To protect the sensors from damage, shear forces and water, the I-Scan sensors were covered in general between two DuPont Kapton HN500 foils. The used TekScan set-up with tap-extendors for the deformable large-scale ice extrusion tests is shown in Figure 3.10. The section on the calibration of the I-Scan system is based on Kubiczek; Herrnring, et al. (2022).

The measuring principle of the I-Scan foil sensors consists of intersecting conductor leads with a pressure sensitive ink in between. An intersection is called sensel, where each sensel is a force-sensitive resistor with an impedance change from above 10 M Ω (no load) to less than 20 k Ω (full load) (TekScan, Inc., 2016). An analogue-to-digital converter assigns an 8 bit value (255 digits) in accordance with the impedance value of each sensel. This value is stored by the I-Scan software as digital output (*DO*) on a computer and needs to be calibrated to get a physical pressure. However, the pressure evaluation and calibration is challenging due to the complex non-linear sensor behaviour and many influencing factors (TekScan, Inc., 2016; Brimacombe et al., 2009; Rose et al., 2004).

To investigate sensor behaviour in detail and improve the calibration methodologies a special pressure unit was build. The pressure unit is shown in Figure 3.11. Within the pressure unit the sensor was placed on a thick flat steel plate and was loaded due to a hydraulic oil behind a Kapton membrane. A detailed description of the pressure chamber is given by Kubiczek; Herrnring, et al. (2022). The developed pressure unit allows a dynamic computer controlled hydrostatic loading of the I-Scan sensors at a relevant pressure range up to 30 MPa. TekScan offers only comparable devices up to 3.447 MPa for static applications.

During the pressure unit tests the I-Scan sensor was loaded by a symmetric trapezoid load function. The pressure in the oil chamber was created by a single acting hydraulic cylinder, which was loaded by a servo controlled hydraulic piston. An exemplary pressure curve in the oil chamber is given in Figure 3.12. For the investigation of the sensor

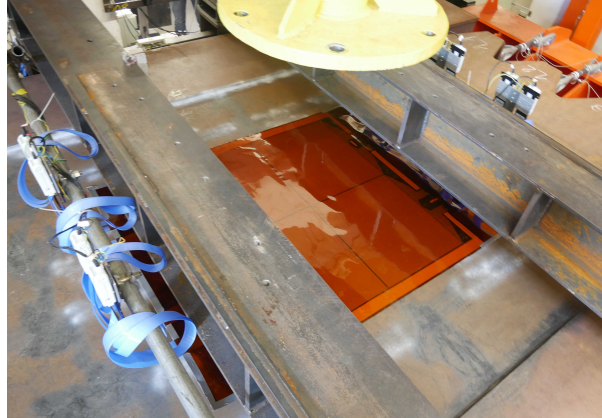
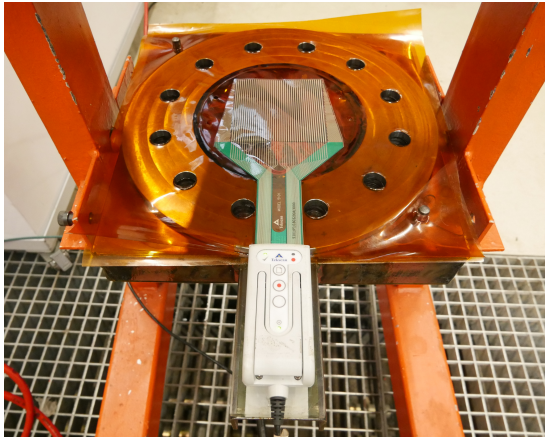
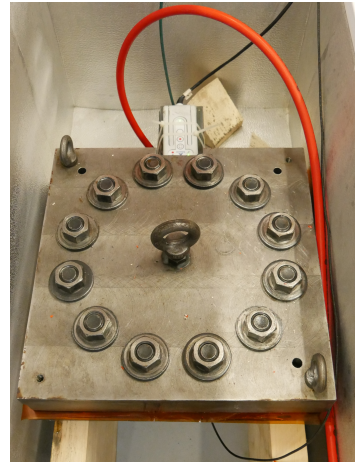


Figure 3.10.: TekScan set-up of the deformable large-scale experiments with a 7105Q map



(a) The open pressure unit with a 5101 I-Scan pressure sensor. The oil chamber is located under the Kapton foil



(b) Pressure Unit in a freezer during testing

Figure 3.11.: Self constructed pressure unit for the investigation and equilibration of 5101 I-Scan sensors

behaviour different loading rates were tested and the mean digital of the sensor was evaluated. These tests were repeated at different ambient temperatures and load sequences. In general only the rising edge of the trapezoid load function was used for evaluation.

Within the pressure unit tests it became apparent, that the sensor behaviour of the I-Scan sensors is non-linear and depends significantly on the selected sensitivity, loading rate and temperature. The sensor behaviour is furthermore influenced by the load history (e.g. number of load cycles and break times). For more details please refer to Kubiczek; Herrnring, et al. (2022).

According to the large variance of the sensor behaviour, the I-Scan system should be calibrated for each material pairing or loading rate (Rose et al., 2004; Brimacombe et al., 2009; TekScan, Inc., 2016). Since many influencing factors, such as the loading rate, depend individually on the considered ice test and failure mechanism, a "calibration" after the test, where the resulting force of the I-Scan system is fitted against the measured total force is recommended (Kubiczek; Herrnring, et al., 2022).

TekScan TekScan, Inc., 2016 offers a simple linear and a non-linear power law approach for calibration:

$$p_{lin}(DO) := a \cdot DO \quad (3.1)$$

$$p_{power}(DO) := a \cdot DO^b \quad (3.2)$$

Both approaches are a function of the digital output $DO \in \{1; 2; \dots; 255\}$. The parameters a and b are unknown variables that must be determined.

While the gradient of the linear approach is constant, the derivative of $p_{power}(DO)$ at the point $DO = 0$ is 0. From a physics perspective, this is questionable, since it implies a zero stiffness of the unloaded sensor. Polynomial approaches used by Brimacombe et al. (2009) are not unfavourable because they are ill-suited for extrapolation (Zielesny, 2016). Therefore, a novel exponential approach is proposed:

$$p_{exp}(DO) := a(b^{DO} - 1) \quad b \neq 1 \quad (3.3)$$

The force F_{TS} acting on the I-Scan sensor is defined as the sum of the product of pressure and sensel area A_{sensel} for all sensels m, n :

$$F_{TS} := A_{sensel} \sum_{m,n=1} p(DO_{m,n}) \quad (3.4)$$

The variables a and b were approximated with an optimisation, where the total force F_{LC} measured by the load cells fitted against the resulting force of the pressure sensor F_{TS} . To account for the non-uniform occurrence probability of the forces during the considered measurement, a weighted least squares approach is used (Zielesny, 2016). The weights w of the respective forces are determined according to the class frequency.

$$SSE := \sum_{i=1} w_i (F_{TS,i} - F_{LC,i})^2 \rightarrow \text{minimize} \quad (3.5)$$

In case of the linear calibration function (Equation 3.1) a weighted linear regression was used to determine a . For the non-linear calibration functions (Equation 3.2 and

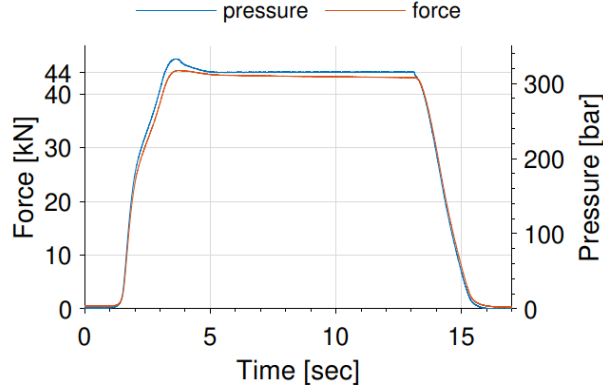


Figure 3.12.: Trapezoidal force function of the force-controlled hydraulic cylinder and the resulting hydrostatic pressure on the I-Scan for a loading rate of 20 kN s^{-1} (reprinted from Kubiczek; Herrnring, et al., 2022; with permission from ASME)

Equation 3.3) a non-linear optimization is necessary. In following the solution for the exponential approach (Equation 3.3) is presented. A solution for the power approach is analog. The task to minimize the sum of squared errors SSE

$$SSE(a, b) = \sum_{i=1} w_i \left(a \sum_{n,m=1} (b^{DO_{m,n,i}} - 1) \cdot A_{sensel} - F_{LC,i} \right)^2 \quad (3.6)$$

$\rightarrow \text{minimize}$

with respect to a and b can be split into two easily performed computations.

For fixed b the minimization of $SSE(a, b)$ with respect to a is a one dimensional linear least squares problem, the solution $a(b)$ of which can written down directly without any iteration. With a known solution $a(b)$ the minimization of $SSE(a, b)$ in a and b is reduced to the minimization of the function

$$SSE^*(b) := SSE(a(b), b) \quad (3.7)$$

of one variable b .

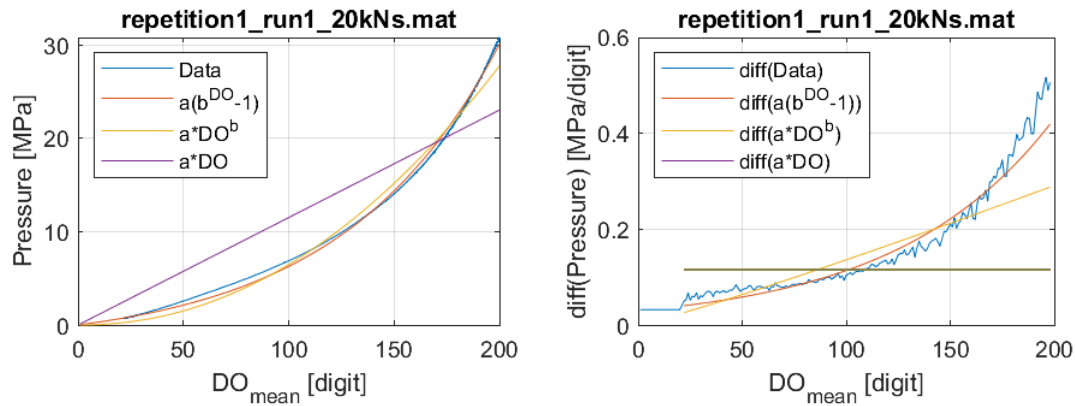
Numerical efficiency can be further increased if the sum of non-linear elements is replaced by the following expression:

$$\sum_{m,n=1} (b^{DO_{m,n}} - 1) = n_1 \cdot (b^1 - 1) + \dots n_{255} \cdot (b^{255} - 1) \quad (3.8)$$

where $n_1; \dots; n_{255}$ are the counts of equal matrix elements of each measured frame. The increase in numerical efficiency is explained by a drastically reduced number of expensive power operations. The optimization was implemented in a MATLAB script and is applicable for "post-test" calibration for the pressure unit and ice extrusion tests, since in both cases the actual total force applied to the sensor is known. The presented method

is similar to the "Movie-Calibration" within the I-Scan software. However, only the TekScan power approach (Equation 3.2) without weights is implemented in the I-Scan software (TekScan, Inc., 2017).

First calibration results are shown in Figure 3.13a for the rising edge of the pressure unit test with a loading rate 20 kN s^{-1} . The linear approach strongly overestimates in the lower range followed by an underestimation of the upper pressure range. Both non-linear approaches match the general trend. However, the TekScan power approach deviates at low and high pressures. This is further illustrated in Figure 3.13b for the first derivative of the curves. The TekScan power approach does not qualitatively reproduce the curve progression. The representation of the proposed exponential approach is much better.



(a) Recalibration of a pressure unit test for a 5101 I-Scan sensor (Pressure range: 3000 psi, Sensitivity: 29) with different trial functions determined calibration functions (reprinted from Kubiczek; Herrnring, et al., 2022; with permission from ASME) (b) Comparison of the derivative of the measured data with the derivatives of the previously determined calibration functions (reprinted from Kubiczek; Herrnring, et al., 2022; with permission from ASME)

Figure 3.13.

Table 3.1 compares the calibration results of the pressure unit tests at different loading rates. The pressure curve is unchanged trapezoidal (compare Figure 3.12). In general, the calibration results showed significant accuracy advantage of the two non-linear approaches compared to the linear trial function. Considering only the non-linear approaches, the exponential approach again shows a considerable accuracy advantage over the power approach. The mean average error (MAE) could be reduced by a factor of up to 2.4 with the exponential approach. Therefore, only the exponential approach was used for the calibration of the brittle ice tests. First calibrated I-Scan pressure measurements of two ice extrusion tests are presented at the end of subsection 3.4.2. However, the exponential approach is not generally recommended for all ice pressure measurements. In case of ductile ice behaviour the variance for optimisation is not sufficient to achieve stable results with a non-linear calibration approach, as a result of a very constant mean ice pressure. For ductile loads the linear approach is the only possibility to achieve robust results (Kubiczek; Herrnring, et al., 2022).

Table 3.1.: Calibration results for a series of pressure unit tests with different loading rates and pressure trial functions. p_{200} indicates the resulting pressure at digital output of $DO = 200$ digits for the corresponding trail function (based on Kubiczek; Herrning, et al. (2022))

| experiment | | exponential trial function | | | | power trial function | | | | linear trial func. | | | |
|------------|-------|----------------------------|-----------|---------|-------|----------------------|-----------|-----------|-------|--------------------|-------|-----------|-------|
| | | load. rate | p_{200} | a | b | p_{200} | MAE | a | b | p_{200} | MAE | a | MAE |
| kN/s | bar | | MPa/digit | - | MPa | MPa | MPa | MPa/digit | - | MPa | MPa | MPa/digit | MPa |
| 0.1 | 264.0 | | 1.690 | 1.01408 | 26.01 | 0.500 | 2.306E-04 | 2.18 | 24.25 | 0.779 | 0.105 | 21.03 | 3.431 |
| 1 | 276.4 | | 1.906 | 1.01369 | 27.03 | 0.482 | 2.949E-04 | 2.14 | 25.21 | 0.796 | 0.108 | 21.56 | 3.389 |
| 10 | 300.1 | | 2.207 | 1.01337 | 29.22 | 0.425 | 4.089E-04 | 2.09 | 27.05 | 0.797 | 0.116 | 23.12 | 3.252 |
| 20 | 300.8 | | 2.254 | 1.01341 | 30.10 | 0.395 | 4.145E-04 | 2.10 | 27.77 | 0.755 | 0.115 | 23.04 | 3.287 |
| 40 | 320.2 | | 2.591 | 1.01311 | 32.50 | 0.317 | 4.988E-04 | 2.08 | 30.05 | 0.775 | 0.125 | 24.98 | 3.658 |

3.4. Ice Extrusion Tests - Quasi Rigid Structures

3.4.1. Conducted tests

Overall, in this thesis the results of 372 extrusion tests against quasi rigid structures are considered. The considered experiments are presented in Table 3.2 and in the Appendix C. In the Appendix C is also the maximum force and the maximum nominal pressure of each test listed. The investigated parameters and the ice sample geometry is illustrated in Figure 3.1. The tests are divided into three different specimen diameters and up to four different specimen geometries. In general, cylindrical specimens with a conical tip were tested. A cone angel of 0° indicates a cylindrical sample without a tip. To investigate the influence of the confinement, the gap height between test structure and pipe was varied. To compare the results of different sample diameters, the same ratios of diameter and gap height were tested in each case. The tests were carried out in a velocity range from 0.01 mm s^{-1} to 10 mm s^{-1} .

All tests with 100 mm and 200 mm specimens were repeated three times. An exception were the tests with a cylinder velocity of 0.01 mm s^{-1} . Due to the long runtime of the tests, no repetition was carried out. Further exceptions are marked in Table 3.2. Due to the high effort of the large-scale tests with 800 mm specimens, it was also not possible to repeat these experiments three times. Accordingly, ductile tests were conducted once and brittle tests twice.

All tests were consistently named based on the test parameters. For example the name Cone100_G50_A20_V4_1 denotes a test run with a specimen diameter of 100 mm, a gap height of 50 mm, a cone angle of 20° and a nominal test velocity of 4 mm s^{-1} . Since the example is the first repetition of the parameter set a 1 is added at the end.

3.4.2. Results

This section summarizes the results of all ice extrusion tests against quasi rigid test structures. In general, the evaluation of the experiments stops 20 mm before the punch emerges from the confining pipe.

Already visually and acoustically large differences for tests with a low and a high test speed become clear. In agreement to previous experiments by other authors (e.g. Bruneau et al., 2013), ductile ice behaviour was observed at slow cylinder velocities. By contrast, only brittle behaviour was observed for tests at velocities of 4 mm s^{-1} and above. Between the 0.1 and 4 mm s^{-1} , ductile, brittle, or transitional behaviour was detected. Transitional behaviour is characterised by alternating brittle and ductile failure. Exemplary force-displacement curves for the three different failure modes are shown in Figure 3.14.

The force of the ductile experiments increased monotonously up to the maximum force. After reaching the maximum force a nearly stable extrusion process began. No significant brittle spalling or generation of loose debris was observed. Acoustically, only a very quite continuous cracking sound was recognized.

The brittle experiments at higher cylinder velocities behaved differently. Due to spalling and crushing of the ice in the contact interface the brittle force curve showed the

Table 3.2.: Considered experiments against quasi rigid test structures. Generally every parameter combination was three times repeated. Exceptions are marked with an asterix in the table

| Diameter | Length | Cone angle | Gap height | Cylinder Velocity |
|----------|--------|---------------|----------------------------|----------------------------|
| mm | mm | ° | mm | mm/s |
| 100 | 100 | 0, 20 | 0***, 6.25, 12.5, 25, 50 | 0.01*, 0.1, 1, 2, 4, 7, 10 |
| 100 | 200 | 0, 20 | 100 | 0.1, 1, 4, 10 |
| 200 | 200 | 0, 10, 20, 30 | 6.25***, 12.5, 25, 50, 100 | 0.01*, 0.1, 1, 2, 4, 7, 10 |
| 800 | 750 | 30 | 230 | 0.1*, 4** |
| 800 | 750 | 20 | 100 | 0.4*, 4** |

*: Only one test of the parameter combination was conducted.

**: Only two tests of the parameter combination were conducted.

***: Due to extreme forces, only selected tests could be carried out.

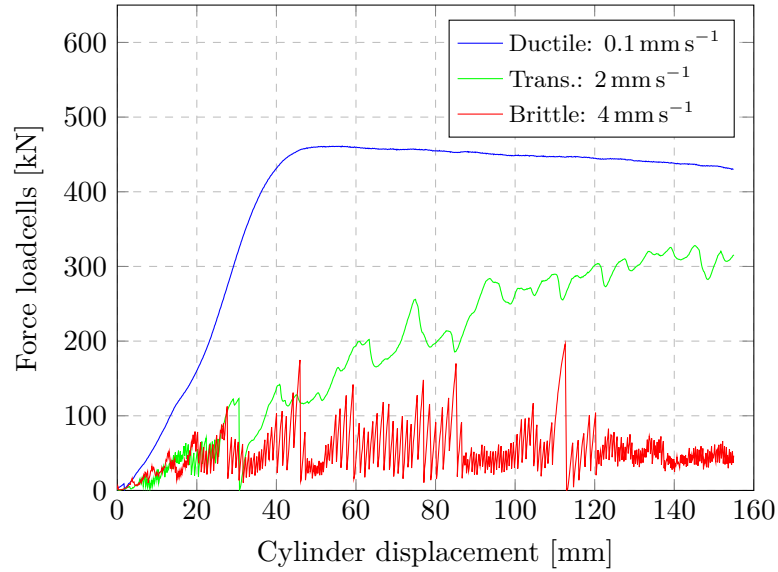


Figure 3.14.: Comparison of a ductile, transitional and brittle ice extrusion test (diameter: 200 mm, gap height: 25 mm, cone angle: 20°)

typical saw-tooth pattern. As a result of the large force oscillations, the brittle process is considerably louder than the ductile one. Impressions of the ductile and brittle ice behaviour in large-scale are given in Figure 3.15. A large number of fragments and pulverized ice was generated during the brittle failure process. In case of brittle behaviour, it was further observed that with a reduced gap height, the fragments become smaller and the pulverized fraction of extruded ice increases. Consistent with the previous observation is also a comparison of the largest load-bearing piece of ice in Figure 3.4.2. For brittle fracture behaviour (1 mm s^{-1} to 10 mm s^{-1}), clear fracture edges and a line-like contact surface can be seen. The ductile specimens (0.1 mm s^{-1} to 0.01 mm s^{-1}) behaved more like "plasticine" with large contact areas.



(a) Ductile test: Cone800_G100_A20_V01 (b) Brittle test: Cone800_G100_A20_V4_1

Figure 3.15.: Exemplary ductile and brittle large-scale ice extrusion tests considering quasi rigid test structures

In Figure 3.17 a detailed evaluation of the peak forces against the cylinder velocity is undertaken. Therefore, the peak forces of 200 mm diameter samples for different normalised gap heights are compared. For determining the normalised gap height G/D the gap height G is divided by the specimen diameter D (compare Figure 3.1). Basically, all curves show the typical speed dependency for ice, which is frequently reported for uniaxial compression tests as shown in Figure 2.4b.

All tests with a speed of 0.1 mm s^{-1} and less behaved ductile. Interestingly, the transition from ductile to brittle behaviour occurred at higher velocities when the normalised gap height was reduced. For example, at 1 mm s^{-1} all three tests with $G/D = 0.5$ were brittle. However, all other tests at same velocity behaved ductile and reached even their maximum force at 1 mm s^{-1} . The ratio between the maximum ductile and brittle loads strongly depended on the gap height. The largest differences are observed for tests at $G/D = 0.25$. At higher confinements, the difference between ductile and brittle loads became smaller again.

The brittle forces were relatively velocity independent for $G/D = 0.5$ and 0.25 , while ductile forces behaved in a strong velocity-dependent manner. It is expected, that the maximum ductile force is not reached for the series with $G/D = 0.5$ in the investigated velocity range.

During ship operation mostly higher loading velocities are to be expected. Therefore,

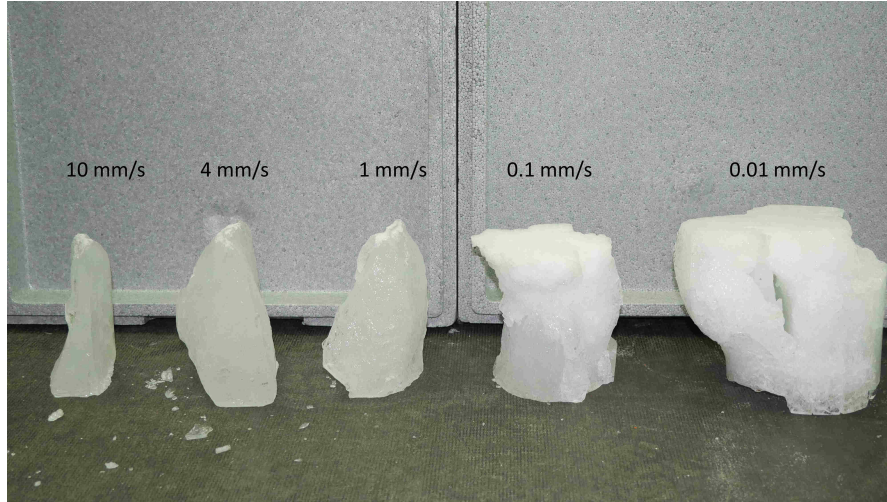


Figure 3.16.: Largest spall after the test of different test speeds at a normalized gap height $G/D = 1$ (specimen diameter: 100 mm; specimen length=200 mm)

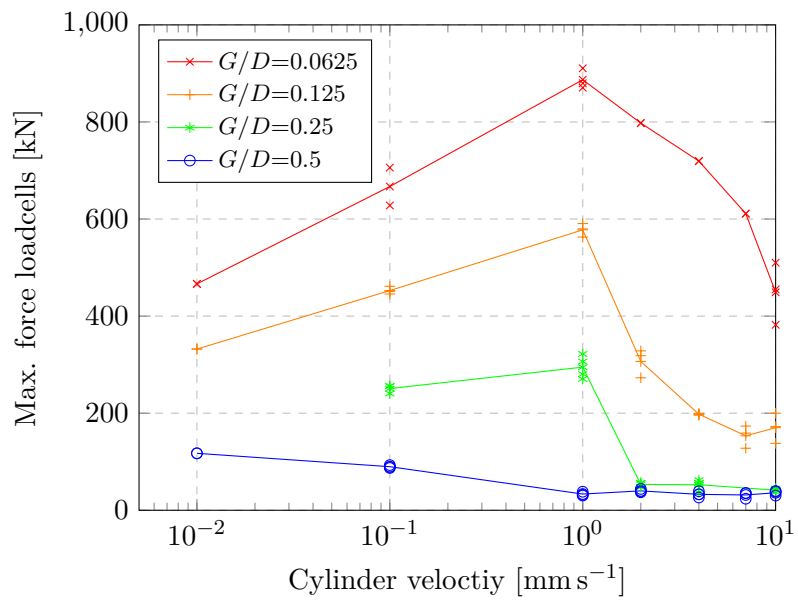


Figure 3.17.: Maximum force of selected ice extrusion tests plotted against the cylinder velocity (diameter: 200 mm, cone angle: 20°). The dots mark the measured values. The lines represent the mean value

further analysis of the results in this thesis will focus on brittle ice behaviour. Ductile loading cases are essentially expected for ships without forward speed e.g. in the harbour or stuck into the ice.

A comparison of several brittle force-displacement curves at different normalised gap heights is given in Figure 3.18. To compare the three tested scales in one plot the nominal pressure p_{nom} is used, which is calculated by the actual force F divided by the nominal contact area A_{nom} . D is still the specimen diameter.

$$p_{nom} := \frac{F}{A_{nom}} \quad (3.9)$$

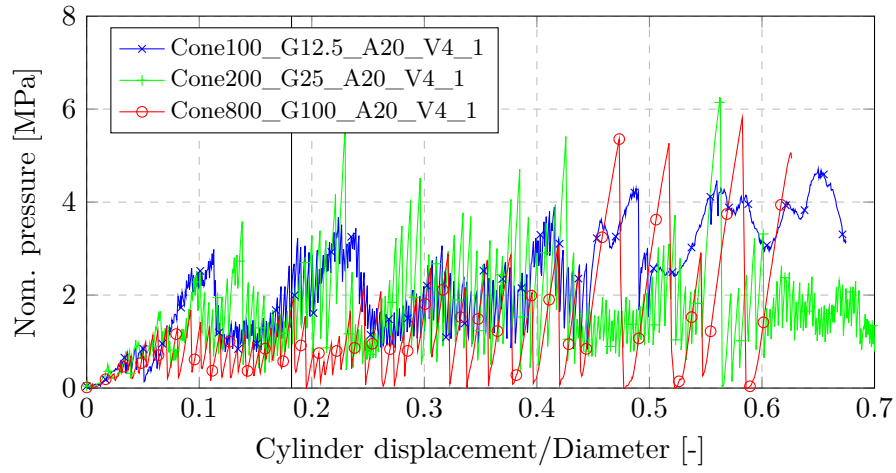
$$A_{nom} := \frac{1}{4} D^2 \cdot \pi \quad (3.10)$$

The tests with a normalised gap height G/D of 0.5 and 0.25 reached their maximum force before the cylindrical part of the specimen has been gained. However, the behaviour with a smaller normalised gap height of $G/D = 0.125$ was significantly different. Here, the maximum load was reached not at the beginning but rather in the cylindrical part of the specimen. This is accompanied by a significant increase in the maximum force. This behaviour can be explained by the increasing resistance to clear the contact area during the ice crushing process.

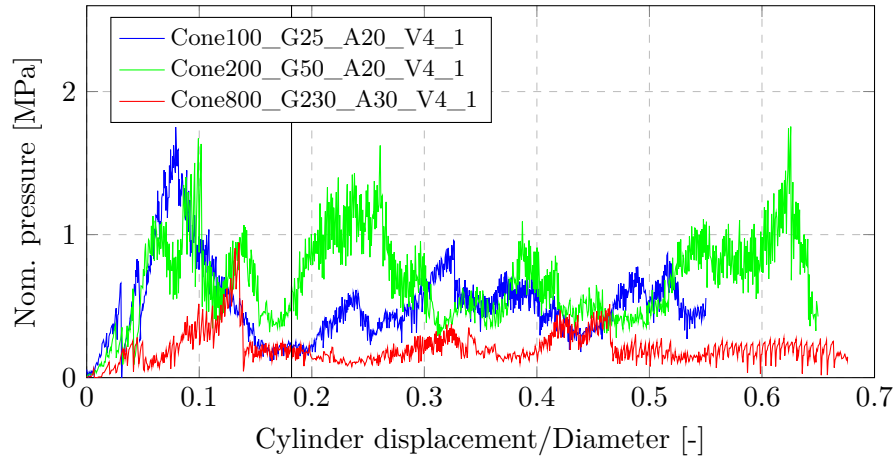
The same effect can also be seen in Figure 3.19. Here is the maximum force plotted against the three investigated cone angles. The cylindrical reference group with a respective cone angle of 0° is given for comparison. For large G/D ratios (low confinement) the peak force of the conical specimens was generally lower than the peak force of the cylindrical ones. However, for small gap heights $G/D \leq 0.125$ the load difference between cylindrical and conical specimens disappeared. In turn, a slight decrease in force was observed with increasing cone angles at large gap heights. The force decrease with increasing cone angle is explained by the specimen shape and increased stress concentration in case of a sharper initial geometry. This effect does not seem to be important for the crushing dominated failures at $G/D \leq 0.125$, since the maximum forces occur in the cylindrical part of the specimen, which is independent of the initial geometry.

Moreover, the results of different sample diameters were compared. The comparison is shown in Figure 3.20. For a better interpretation, the only tests with 0.1 mm s^{-1} (all ductile failure) as well as tests with 4 mm s^{-1} (all brittle failure) are selected in the plot. Again, the normalised gap height G/D is chosen as the abscissa and the maximum nominal pressures as ordinate. The curves of the different specimen diameters are surprisingly similar, despite a difference in nominal contact area by a factor of 64. Basically, as described above, an increase in force with decreasing G/D -ratio was observed.

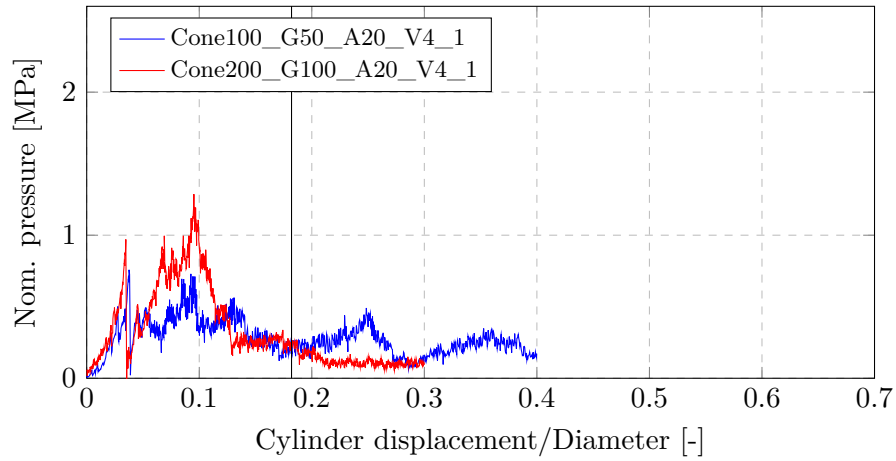
The measured maximum forces in ductile mode at 1 mm s^{-1} are greater than the certain brittle ones at 4 mm s^{-1} . Since ductile forces are strongly velocity dependent, even potentially higher loads until reaching the transition velocity are possible. In addition, a transition from brittle to ductile/transient behaviour seems to be observed at extremely high confinement (compare $D = 200 \text{ mm}$ $V = 4 \text{ mm s}^{-1}$).



(a) $G/D=0.125$



(b) $G/D=0.25$



(c) $G/D=0.5$

Figure 3.18.: Exemplary comparison of the nominal pressure curves at a cylinder speed of 4 mm s^{-1} for different normalised gap heights and specimen diameters. The vertical black line indicates the height of the conical tip

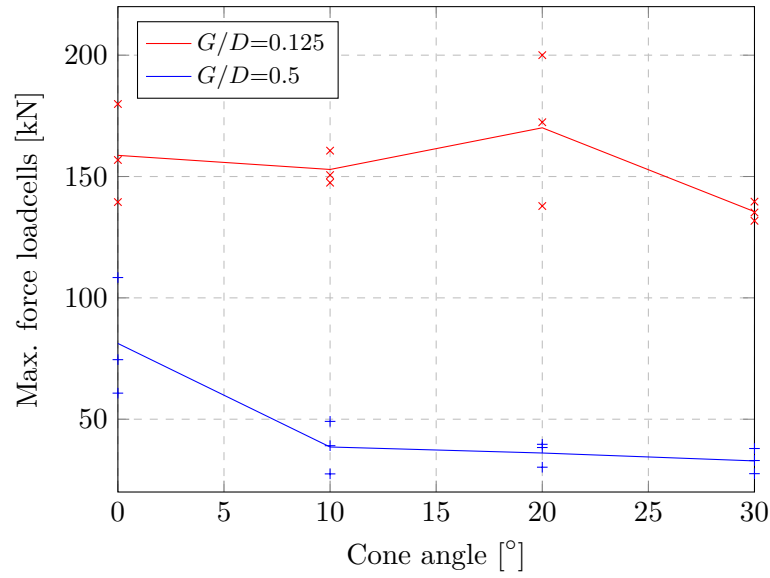


Figure 3.19.: Maximum force of 200 mm ice extrusion tests for different cone angles against a quasi rigid structure with a cylinder velocity of 4 mm s^{-1} . The dots mark the measured values. The lines represent the mean value

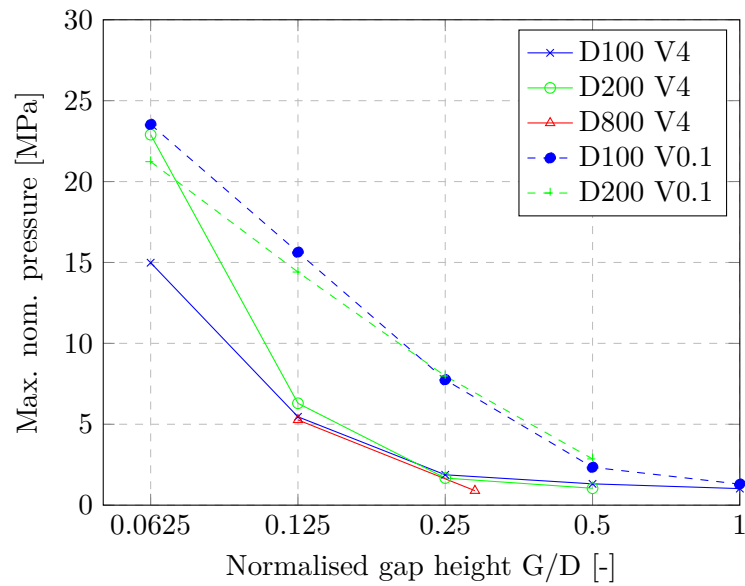


Figure 3.20.: The maximum nominal pressure of the ice extrusion tests against quasi rigid structures over the normalised gap height G/D for specimens with a cone angle of 20° (the cone angle of the 800 mm specimens at $G/D=0.2875$ is deviating 30°). Each point is the mean value of the respective group

Furthermore, pressure melting was observed at approximately 100 MPa nominal pressure within the experiments with a closed gap ($G = 0$). During these experiments, water was cyclically extruded from the remaining very small slits. The result was in accordance with the equations of state for Ice Ih (Feistel and Wagner 2006). Feistel and Wagner indicate the melting pressure at -9.16°C at 102 MPa. The temperature of the sample was not measured during and after the experiment. However, a temperature rise in the sample would be quite plausible.

Finally, the TekScan ice pressure measurements will be evaluated. As the calibration is quite demanding (compare section 3.3), the TekScan data obtained was used first to evaluate the ratio of loaded area. The loaded area ratio is defined as the loaded area measured by TekScan A_{TS} divided by the nominal contact area A_{nom} .

$$\frac{A_{TS}}{A_{nom}} = \frac{n_{SenselDO \geq 3} \cdot A_{Sensel}}{\frac{1}{4}D^2 \cdot \pi} \quad (3.11)$$

$n_{SenselDO \geq 3}(F_{max})$ gives the number of loaded sensels and A_{Sensel} the area of each intersection of the I-Scan sensor. Only sensels with a load of at least 3 digits digital output are considered loaded. 3 digits is the default threshold value in the I-Scan software.

The results are given in Figure 3.21. In the plot the loaded area ratio at maximum force is evaluated. The loaded area of the brittle tests was far below of the active area of ductile tests. Only slight differences between the samples with 100 mm and 200 mm diameter were determined. Also the results of the 800 mm tests were in the same range. A significant influence of the gap height could be seen. With increasing confinement, the loaded area also increased. In the case of brittle results, the loaded area increased from 20% to 40% to approximately 60% for small normalised gap heights. The ductile tests loaded up to 120% of the normalised contact area. Overall, the results for $G/D=0.5$ are quite comparable with the lake ice experiments of Takeuchi et al. (2001).

Furthermore, using the post-test calibration developed in section 3.3, the tests Cone200_G25_A20_V10_1 and Cone200_G50_A20_V10_1 were calibrated, since both tests were used for validation of the numerical ice material model presented in chapter 4. The results of both calibrated measurements are presented in Figure 3.22 and Figure 3.23. The corresponding optimized calibration factors for the linear and exponential calibration approach are given together with the normalised mean average error (nMAE) in Table 3.3.

Table 3.3.: Post-test calibration results of two Tekscan measurements with linear (Equation 3.1) and exponential (Equation 3.3) approach

| Test run | F_{median} kN | a_{lin} $\frac{\text{MPa}}{\text{digit}}$ | $nMAE_{lin}$ % | a_{exp} $\frac{\text{MPa}}{\text{digit}}$ | b_{exp} - | $nMAE_{exp}$ % |
|-----------------------|--------------------|--|-------------------|--|----------------|-------------------|
| Cone200_G25_A20_V10_1 | 52.9 | 0.1267 | 23.32 | 4.0926 | 1.0133 | 8.56 |
| Cone200_G50_A20_V10_1 | 15.4 | 0.1091 | 28.72 | 6.3560 | 1.0104 | 10.78 |

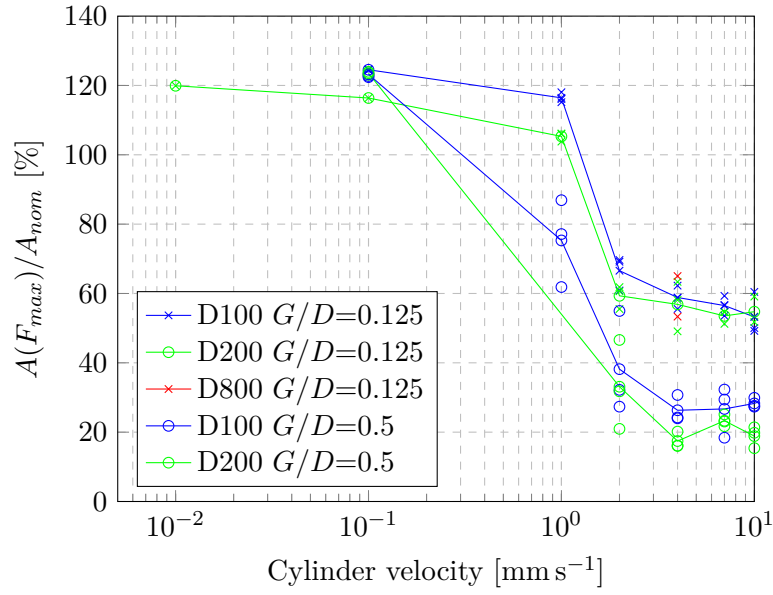


Figure 3.21.: Contact ratio at maximum force against cylinder velocity. The dots mark the measured values. The lines represent the mean value

According to the residual plot in the upper left corner in Figure 3.22 and Figure 3.23 the post-test calibration were converged in both cases for the exponential approach (Equation 3.3). Comparing the results linear and exponential approaches, the nMAE is more than halved in case of the exponential approach (compare Table 3.3). The nMAE used for the assessment was normalised with the median of the global force. The force was measured with the load cells. Furthermore, it can be clearly seen in the second plot in the top as well as in the force-time plot in Figure 3.22 and Figure 3.23 that the exponential approach represents the measured force curve F_{LC} better than the linear approach.

Finally the calibrated pressure distribution at maximum force for both tests is given in top right of the respective plot. In the measurement, the distinctly uneven pressure distribution in the centre can be seen. Significant load-bearing parts have broken off at the edge of the specimen. As expected, the loaded area is larger for the smaller gap height. However, the maximum pressures were in the same range of 55 MPa to 60 MPa.

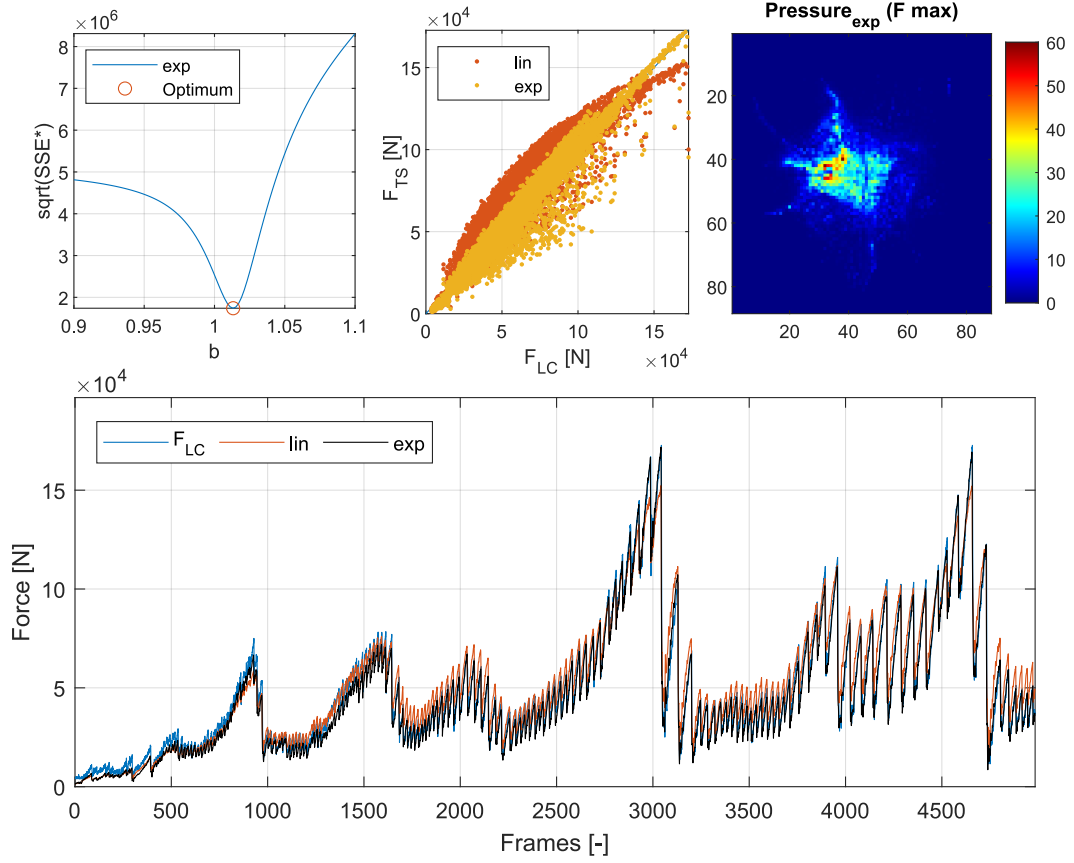


Figure 3.22.: I-Scan calibration of a brittle ice extrusion test Cone200_G25_A20_V10_1 (diameter: 200 mm, gap height: 25 mm, cone angle: 25°, velocity: 10 mm s⁻¹); Left top: Residual plot for the exponential calibration function Equation 3.3 according to Equation 3.7; Center top: Load cell F_{LC} vs. I-Scan Force F_{TS} of the optimum solution for the linear Equation 3.1 and exponential calibration function Equation 3.3; Left top: Exponentially calibrated pressure measurement at maximum load; Bottom: Comparison of the total force measured by the load cells F_{LC} with the resultant sensor force F_{TS} with an exponential Equation 3.3 and linear calibration approach Equation 3.1

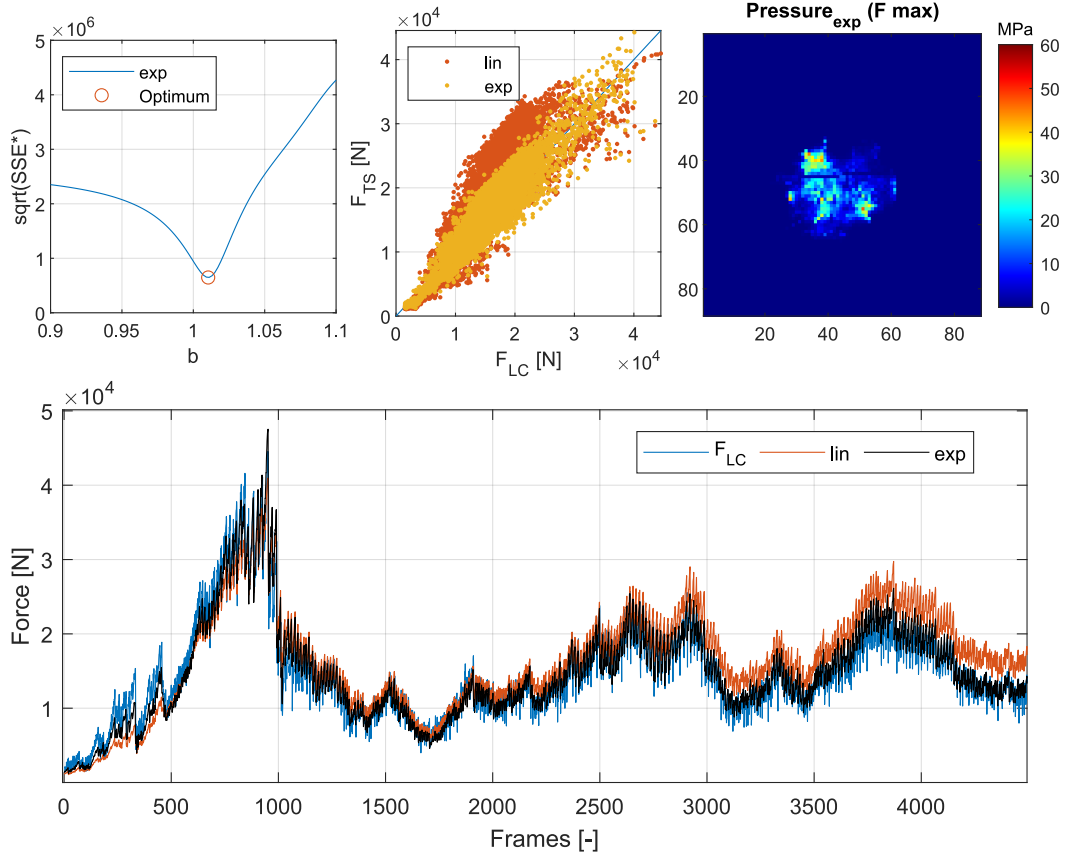


Figure 3.23.: I-Scan calibration of a brittle ice extrusion test Cone200_G50_A20_V10_1 (diameter: 200 mm, gap height: 50 mm, cone angle: 25° , velocity: 10 mm s^{-1}); Left top: Residual plot for the exponential calibration function Equation 3.3 according to Equation 3.7; Center top: Load cell F_{LC} vs. I-Scan Force F_{TS} of the optimum solution for the linear Equation 3.1 and exponential calibration function Equation 3.3; Left top: Exponentially calibrated pressure measurement at maximum load; Bottom: Comparison of the total force measured by the load cells F_{LC} with the resultant sensor force F_{TS} with an exponential Equation 3.3 and linear calibration approach Equation 3.1

3.5. Ice Extrusion Tests - Deformable Structures

Within this thesis three large-scale ice extrusion tests against deformable ship-like structures are considered. The test set-up and tested panels are described in section 3.1. All considered brittle tests were conducted with a nominal cylinder velocity of 4 mm s^{-1} and a cone angle of 20° . The test parameters of the considered deformable tests together with the achieved maximum forces and according plastic panel deformations are given in Table 3.4. The force displacement curves of the three experiments are shown in Figure 3.24 and a photo during a test is presented in Figure 3.25.

Table 3.4.: Maximum forces and pressures of the deformable large-scale ice extrusion tests with brittle ice behaviour

| Name | Gap height | Max. force | Max. nom. pressure | Max. plas. displ. |
|----------------------------|------------|------------|--------------------|-------------------|
| - | mm | kN | MPa | mm |
| Cone800_Panel1_G100_A20_V4 | 100 | 1858 | 3.70 | 87 |
| Cone800_Panel2_G200_A20_V4 | 200 | 455 | 0.91 | 5.7 |
| Cone800_Panel2_G100_A20_V4 | 100 | 2014 | 4.01 | 84 |

The large-scale tests again had to be carried out in two strokes, as the maximum cylinder displacement was limited to 400 mm. Thus the test was stopped after 375 mm and the piston under the large yellow crossbar was lengthened by a threaded rod. Unlike before, in the case of the deformable structure it is not possible to neglect individual force peaks after the conversion break, since they are potentially responsible for additional plastic deformation of the panel. Therefore, the entire force curve was considered in the evaluation, although it is possible that the ice heals during the waiting period between the first and second stroke of each test, which may explain the high first force peak of the second stroke.

A single experiment was conducted with an initial gap height of 100 mm on Panel 1. In case of Panel 1 the first contact of the conical specimen was in the centre of a plate field. A maximum force of 1858 kN was reached. During the test the panel was significantly deformed. A maximum plastic deformation of the plate of 87 mm together with according deformations and buckling of the frames was measured. Different photos of the deformed Panel 1 are given in Figure 3.26.

The panel deformations of all deformable tests were measured with a distance laser sensor. Using a linear drive, the laser sensor was moved across the panel in the transverse direction every 100 mm. The in Matlab post-processed results of the laser sensor for Panel 1 are shown in Figure 3.27. The largest plastic deformations of up to 87 mm were measured in the loaded area between frame 3 (F3) and frame 4 (F4).

On Panel 2 two brittle tests were conducted. Panel 2 differed from Panel 1 by a modified frame arrangement. In case of Panel 2 the tip of the ice specimen encounters directly on a frame. The gap height of the first test was 200 mm. For the second test,

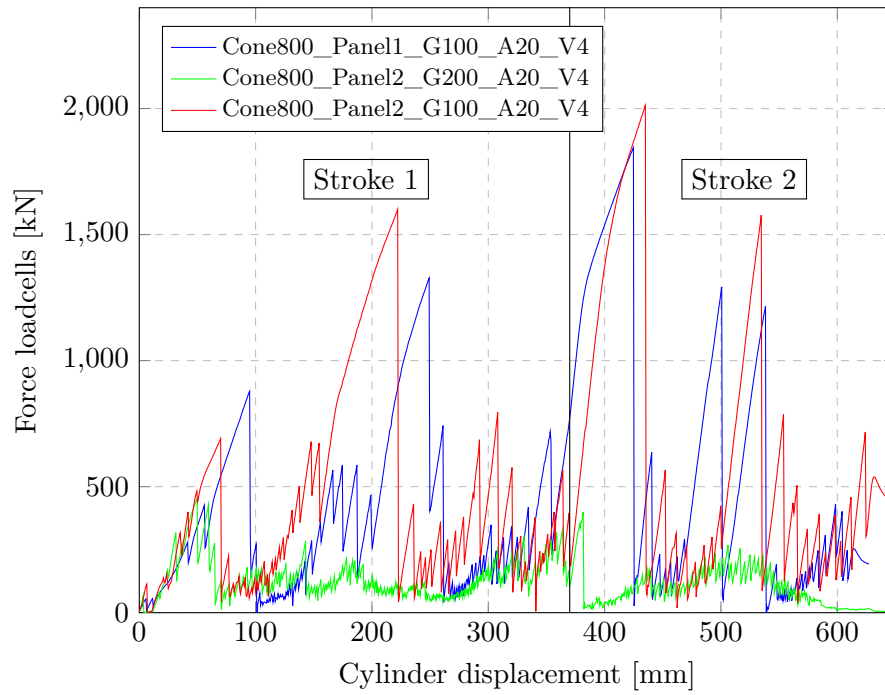
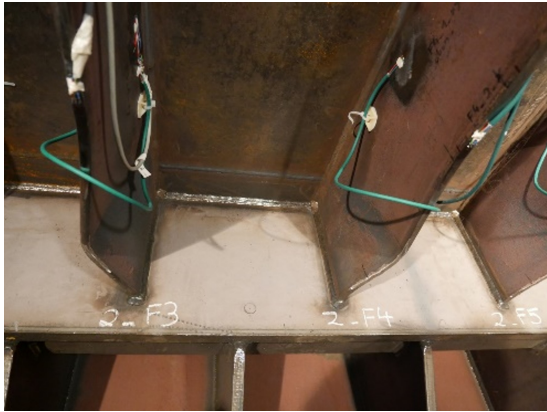


Figure 3.24.: Force-displacement curves for large-scale ice extrusion tests against deformable ship structures



Figure 3.25.: Ice extrusion test Cone800_Panel2_G200_A20_V4 during testing



(a)



(b)



(c)

Figure 3.26.: Deformed Panel 1 after test Cone800_Panel1_G100_A20_V4

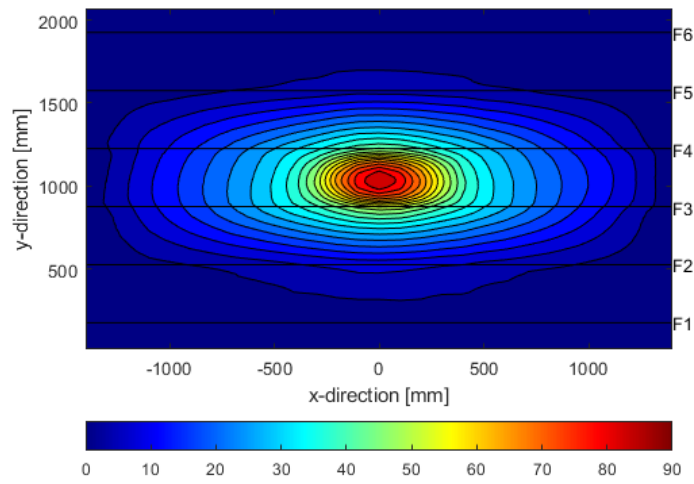


Figure 3.27.: Plastic deformation of Panel 1 after test Cone800_Panel1_G100_A20_V4

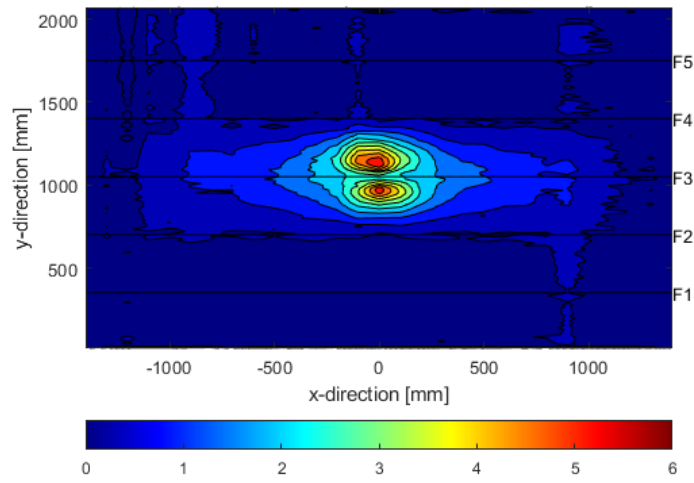


Figure 3.28.: Plastic deformation of Panel 2 after test Cone800_Panel2_G200_A20_V4

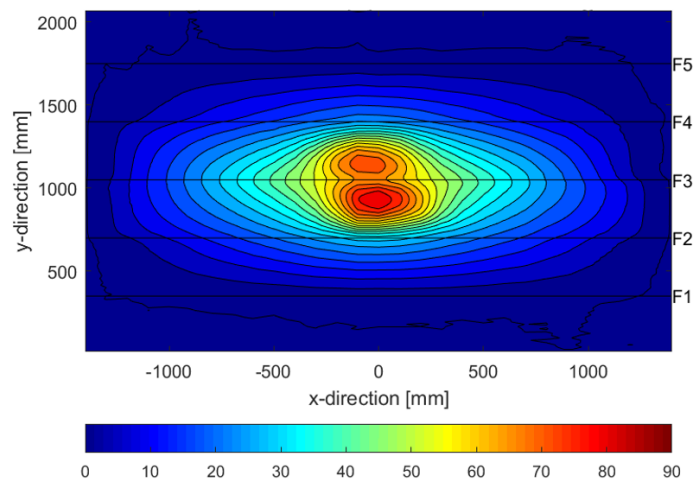


Figure 3.29.: Plastic deformation of Panel 2 after test Cone800_Panel2_G100_A20_V4

the gap height was reduced to 100 mm. Thus, the maximum forces of the first test on Panel 2 reached only 455 kN and increased to 2014 kN in the second test due to the higher confinement.

Again, the plastic deformations of both test runs are presented in Figure 3.28 and Figure 3.29. A maximum plastic deformation of 5.7 mm resulted for the test with 200 mm gap height. The frame F3 deformed considerably less than the plate field. The maximum plastic deformation of the plate after second test was measured with 84 mm. Thus, the maximum plastic deformations for Panel 1 and Panel 2 were at the same level. Thereby frame 3 (F3) of Panel 2 was deformed considerably more than frame 3 (F3) and frame 4 (F4) of Panel 1.

4. The Mohr-Coulomb Nodal Split Ice Model

In this chapter the novel Mohr-Coulomb Nodal Split (MCNS) ice model is presented. The model was published by the author of these thesis (Herrnring; Ehlers, 2021). Significant parts of the chapter are based on the publication. The already published numerical results on the small-scale ice extrusion tests are extended by the simulation of the quasi rigid and deformable large-scale ice extrusion tests.

4.1. Methodology

The development of a versatile and robust ice load model, which can represent spalling, material conservation during failure and the continuous nature of the ice failure processes is the subject of this chapter. The model is intended to be applicable for the simulation of various crushing and spalling dominated ice-structure interaction problems in the range of low (e.g. level ice, ice floes) to high confinement (e.g. iceberg collisions) conditions.

The objective of the development is the presentation of an effective finite element model for small-, and full-scale application, which considers crushing and spalling in a simplified form. For the development and validation of the MCNS ice model, simulated maximum ice forces and contact pressures are compared with experimental results of the previous ice extrusion test series.

Despite a variety of alternative mesh-free methods, FEM is currently considered the most well-developed choice for ice-structure interaction simulations. A big advantage of FEM are many contact algorithms, which allow the coupling of the ice- and structural model. Therefore, the model developed in this paper is implemented into the explicit FEM solver LS-DYNA R11.1.0.

In case of ice-structure interaction it can be assumed that Coulombic faulting due to spalling is the dominating failure mechanism limiting the maximum ice force (compare section 2.2). In addition, the continuum behaviour of ice is also significantly pressure-dependent (Rist; Murrell, 1994).

Thus the MCNS model based on a common Mohr-Coulomb material model. To motivate the ice material behaviour a failure surface will be derived in Figure 4.1. The critical shear stress is plotted against the hydrostatic pressure. The melting pressure for ice at approximately -10°C is achieved at 110 MPa (Feistel et al., 2006). Melting is represented in the MCNS model by element erosion.

The Mohr-Coulomb theory expresses the relation between the shear stress and the normal stress at failure (Hudson et al., 1997). The fundamentals of the Mohr-Coulomb theory are given for example by Gross et al. (2016).

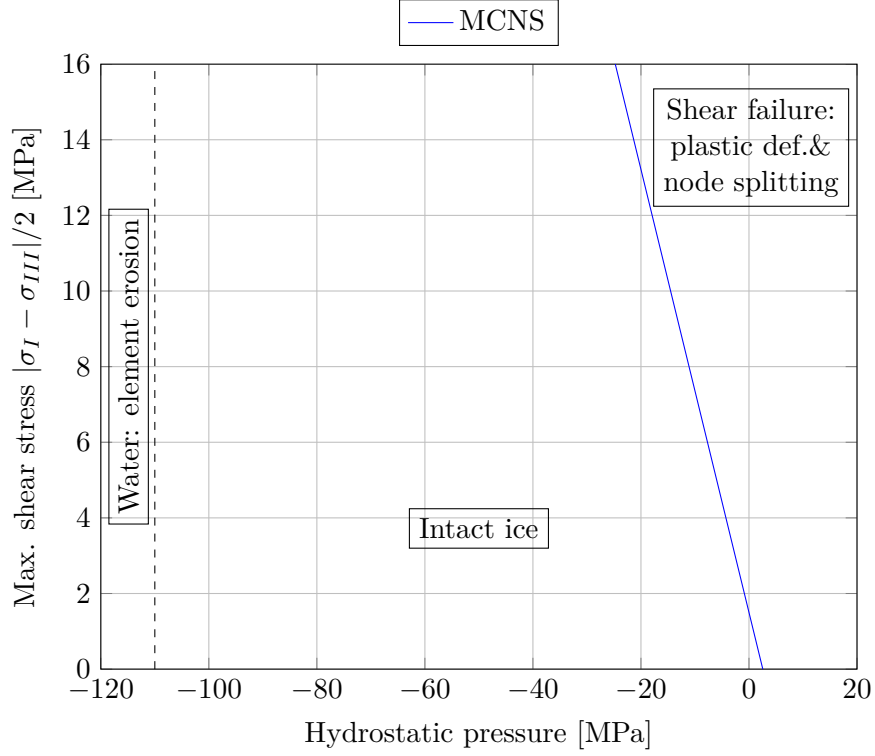


Figure 4.1.: Failure surface of the MCNS model for freshwater ice at $-10\text{ }^{\circ}\text{C}$. The melting pressure is given according to Feistel et al. (2006)

$$|\tau| = -p \tan \rho + c \quad (4.1)$$

According to the Mohr-Coulomb theory the critical shear stress τ depends on the cohesion c , the hydrostatic pressure p and the friction angle ρ . For a given friction angle ρ and the cohesion c the tensile failure stress σ_t and compressive failure stress σ_c are determined via Gross et al. (2016):

$$\sigma_t = 2c \cos \frac{\rho}{1 + \sin \rho} \quad (4.2)$$

$$\sigma_c = 2c \cos \frac{\rho}{1 - \sin \rho} \quad (4.3)$$

The Mohr-Coulomb failure criterion is often used for the description of soils, rocks and concrete materials (Hudson et al., 1997; Gross et al., 2016). The brittle failure of rocks and ice are in many respects similar (C. Renshaw et al., 2001).

The following idealizations are made in the MCNS model with respect to brittle ice-structure interaction problems:

- creep is neglected,

- a thermodynamic adiabatic process with constant material properties is assumed,
- a Mohr-Coulomb failure surface and continuum behaviour is assumed,
- changes (e.g. dynamic recrystallization) of the grain structure are neglected,
- broken ice remains broken; pressure induced healing and sintering processes are neglected.

In the MCNS model an elastic-ideal plastic Mohr-Coulomb Material model is combined with node splitting approach (`*CONSTRAINED_TIED_NODES_FAILURE`). The methodology of the node splitting algorithm is given in Figure 4.2 for the example of a compact tension specimen. For the node splitting approach all elements are detached from their neighbour elements in the preprocessing process. Thus, the nodes of each considered element are independent of the neighbouring element. The coupling is done with dedicated kinematic couplings of coincident nodes. The couplings are deleted when the volume weighted plastic strain in the neighbouring elements exceeds a given critical value. The plastic failure strain in the MCNS model is selected as small as possible to achieve a brittle-like model behaviour. On the other hand is a slight plasticity favourable to stabilize the material model during explicit time integration.

Since the elements remain in the model after failure mass, volume and energy are preserved (Michaloudis, 2019). As the ice-structure interaction is dominated by compressive loads in particular volume preservation in contact zone is of great importance. Michaloudis et al. (2010) showed during different demolition simulations of buildings the importance of volume and mass preservation. The node splitting approach was compared to element erosion technique. Unlike the element erosion technique, the collapse behaviour of the considered buildings could be correctly reproduced with the node-splitting approach. It was concluded that the node splitting approach is especially necessary for compression-dominated problems, whereas for bending problems the conventional element erosion approach is quite reliable.

Although the node splitting approach has many advantages compared to element erosion, the additional computational effort due to a significantly increased number of nodes, couplings, and additional contact faces is not inconsiderable and should only be applied to domains where failure actually has to be considered (Michaloudis, 2019).

For an LS-Dyna keyword deck of the MCNS model the following cards are used:

- **Solver:** Explicit finite element solver LS-Dyna R11.1.0 (double precision, SMP)
- **Element type:** Fully integrated S/R solid elements for poor aspect ratios, `ELFORM=-1`
- **Mesh:** A hexahedron mesh is created as uniformly as possible via splitting of a tetrahedron mesh once. The mesh allows the elements to slide and the fracture paths to be as random as possible. Non-physical stacking of regular detached hexahedron elements is prevented. An exemplary mesh of a cylindrical specimen with a diameter of 200 mm and an element size of 12.5 mm is shown in Figure 4.4.

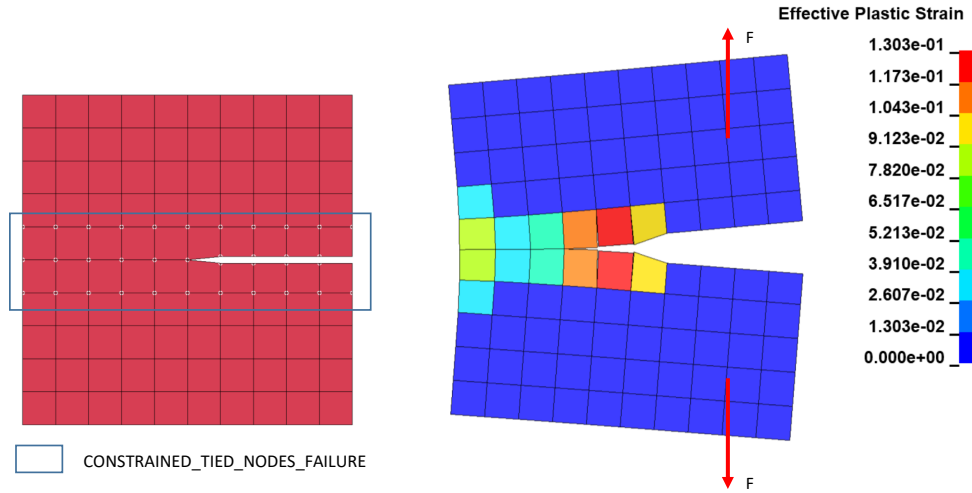


Figure 4.2.: Idealized simulation of a notched specimen with the node splitting technique in LS-Dyna (*CONSTRAINED_TIED_NODES_FAILURE)

If elements must pass through a gap as in case of the ice-extrusion test, the size of the element should not be larger than half the size of the gap.

- **Material model:** *MAT_MOHR_COULOMB - The parameters for granular freshwater ice at approximately -10°C are presented in Table 4.1. The analytical tensile stress is set to 1.72 MPa based on bending test data of G. W. Timco; Brien (1994). The uniaxial compression failure was defined with 5.23 MPa according to Härer (2019) and Kellner; Stender, et al. (2019). The following friction angle and cohesion is determined with Equation 4.2 and Equation 4.3. To model pressure melting, a maximum pressure according to the equation of state of Feistel et al. (2006) is defined with *ADD_EROSION. The melting pressure of -10°C cold freshwater ice is about 110 MPa. To represent pulverization and extrusion phenomena, as observed during crushing at high confinement (Ian Jordaan; G. Timco, 1988; Wells et al., 2011; Herrnring; Kubiczek, et al., 2020), the maximum plastic strain is limited. A critical value of 1 is assumed and also implemented in the *ADD_EROSION card.
- **Failure model:** The failure model is realized by the simple node splitting approach of the LS-Dyna keyword *CONSTRAINED_TIED_NODES_FAILURE. A critical plastic strain at failure of 0.002 was used for all simulations.
- **Ice self-contact:** *CONTACT_SINGLE_SURFACE (SOFT=2, SBOPT=5, DEPTH=5) with a constant friction coefficient of 0.05 is utilized.
- **Time step size:** The critical time step size is reduced precautionary with TSSFAC=0.5.
- **In general:** The best practice recommendations of LS-DYNA® Aerospace Working Group (2017) and Kessler (2014) are used. Further information on the LS-Dyna

keyword inputs can be found in the software documentation (LSTC, 2019a; LSTC, 2019b).

The parameters of the model are derived sequentially as presented in Figure 4.3. The sequence was chosen so that the parameters could be determined as unique as possible.

Table 4.1.: Material parameters for *MAT_MOHR_COULOMB for granular freshwater ice at -10°C

| | | |
|------------------------------|--------------------|-------------------|
| Density | kg m^{-3} | 900 |
| Elastic shear modulus | Pa | 3.5×10^9 |
| Poisson's ratio | - | 0.33 |
| Angle of friction | rad | 0.526 |
| Cohesion value | Pa | 1.5×10^6 |
| Ice-Ice friction coefficient | - | 0.05 |

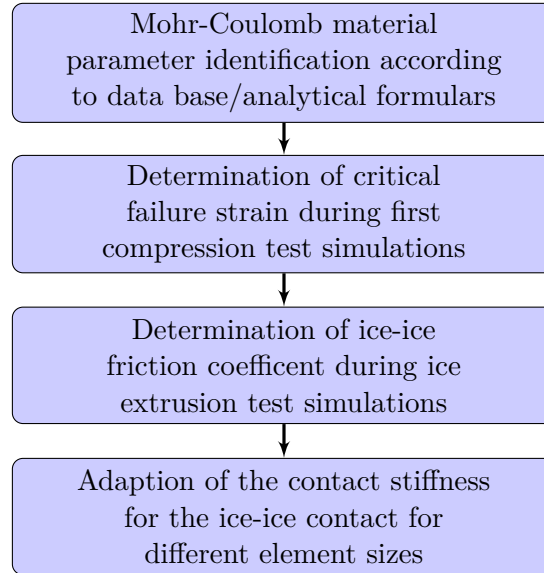


Figure 4.3.: Parameter identification process of the MCNS model

4.2. Contact Modelling

Contact models have a crucial function for the proposed model. During the collision simulation ice elements become detached if the equivalent plastic strain exceeds 0.2%. For these elements, it is necessary to consider contact, and a proper contact formulation is required to transfer mechanical loads.

To simulate the contact problems in an optimal way, only surface-based formulations are used. The ice self-contact (contact between broken ice elements) is represented by a

single surface contact `SOFT=2` with an edge-to-edge treatment. The surface based `SOFT=2` contact is recommended for complex problems in LS-Dyna (LS-DYNA® Aerospace Working Group, 2017). During the first MCNS ice-structure interaction simulations with different element sizes, it became apparent that the contact stiffness has a major influence on the stability of the model. A too high contact stiffness leads to unstable results.

For the investigation of the contact stiffness, numerical tests were conducted. A cylindrical ice model, according to Figure 4.4 is considered. The applied boundary conditions are: a prescribed displacement at the top of the cylinder, a fixed boundary condition in normal direction for the remaining boundary surfaces. The simulations consider two extreme cases. At first, a conventionally assembled finite element mesh without contact is used. Second, a mesh where all elements are detached is studied. In this second case, the forces of adjacent elements are transferred only via the contact algorithm.

As expected, the stiffness of the model decreases in the second case considering the detached elements. For the element size of 12.5 mm the stiffness reduction is 27.6%. This effect is reasonable for ice. During experiments, broken ice is softer than intact ice, due to the cracks that develop on the micro and macro scale (Singh et al., 1996; Xiao, 1997).

The recommended contact stiffness scale factors are given in Table 4.2. With larger elements, the simulations were initially unstable. Therefore, the contact stiffness for the element size of 50 mm has to be reduced to 0.2. How exactly the value was determined is explained in section 4.4. The contact definition could be even found in the section B.

4.3. Verification of the MCNS Model

This section presents the results of the MCNS model based on the parameter set according to Table 4.1 and Table 4.2. In order to verify the MCNS model in well-defined applications uniaxial tensile and compression tests were simulated. A cylindrical specimen (diameter = 200 mm, length = 200 mm) similar to Figure 4.4 is considered. The element size is 12.5 mm. In the simulation a fixed boundary condition for the bottom in axial direction is applied. The top surface of the model is subjected to a controlled translational velocity of 10 mm s^{-1} . The lateral boundaries are all unconstrained.

The simulation results of the model are given in Figure 4.5. The corresponding stress-strain curves are given in Figure 4.6. In particular, the stress shown in Figure 4.6 is calculated by determining the total reaction force of the top nodes divided by the constant nominal cross section area. As expected, the stress strain curves depend on the loading direction due to the used Mohr-Coulomb yield condition. Figure 4.6 shows

Table 4.2.: Recommended contact stiffness scale factors SFS for different element sizes

| Element size [m] | SFS [-] |
|------------------|---------|
| 0.0125 | 1.0 |
| 0.05 | 0.2 |

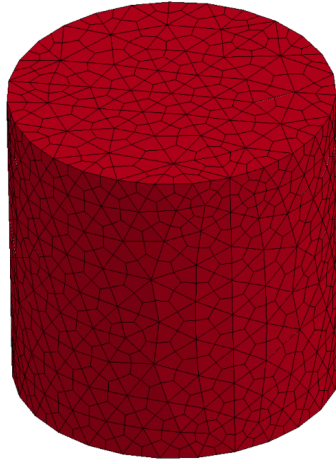


Figure 4.4.: Finite element mesh for a MCNS simulation of a cylindrical specimen with 200 mm diameter

that response of the overall structure can be attributed to the ideal plastic material behaviour. The constant plateau according to Figure 4.6 corresponds to the compressive failure stress σ_c and tensile failure stress σ_t of the used plasticity model. In tension the simulation achieves a maximum stress of 1.69 MPa in comparison to analytical tensile failure stress of 1.73 MPa according to Equation 4.2. The corresponding deviation is 2.3%. In the compressive case the simulation reaches 5.12 MPa. The analytical value of Equation 4.3 is 5.21 MPa. The deviation for the compressive case is specified as 1.73%. The simulation results were independent of the ice-ice friction coefficient.

According to Figure 4.6, depending on the loading direction the post fracture behaviour ranges from virtually no transmitted forces in the case of tension to transmission of forces during compression.

Finally, this section addresses the post-fracture behaviour of the used Mohr-Coulomb material model in case of compressive failure. For the study an idealized failure was simulated of the previously considered compression test, in which at 0.08 s the upper boundary condition was deleted. In Figure 4.7 z-stresses (in axial direction) of the MAT173 material model used in the MCNS Model and the common elastic material model MAT1 are presented.

In the elastic case, tensile and compressive oscillations occur with an amplitude equal to the previous compressive stress. In the case of the Mohr-Coulomb model, internal energy dissipates into plastic deformation and tensile vibration therefore only reach values in the range of maximum tensile strength. This characteristic is important for the MCNS model to obtain a stable numerical behaviour under compressive failure and considering the anisotropic behaviour of ice.

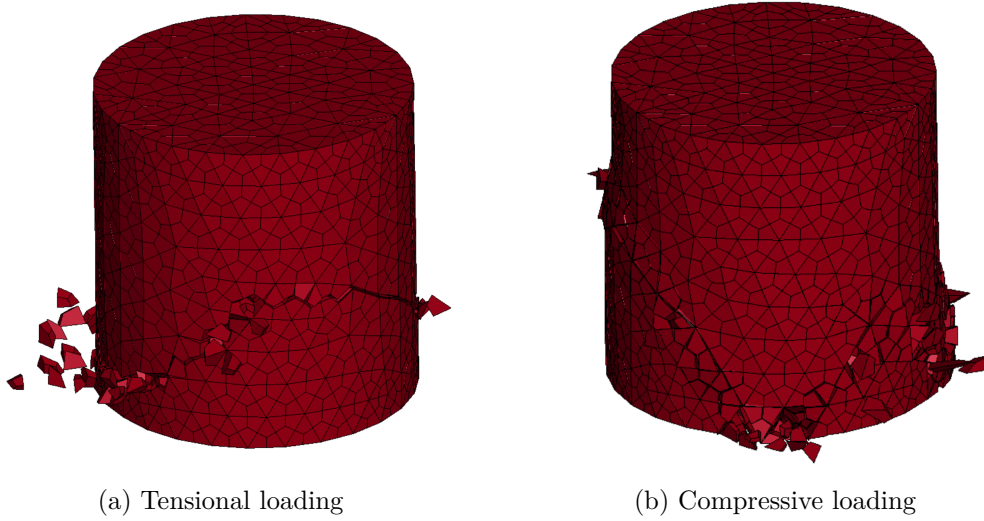


Figure 4.5.: MCNS simulation results for a cylindrical specimen (Diameter = 200 mm, Length = 200 mm) under uniaxial tensional and compressive loading (redrawn after Herrnring; Ehlers, 2021)

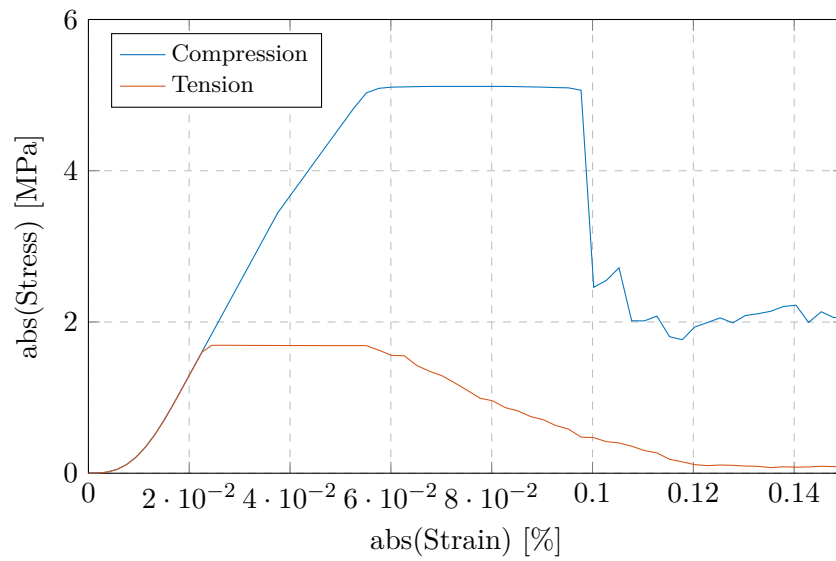


Figure 4.6.: Engineering stress-strain curves of the tensile and compression test simulation (redrawn after Herrnring; Ehlers, 2021)

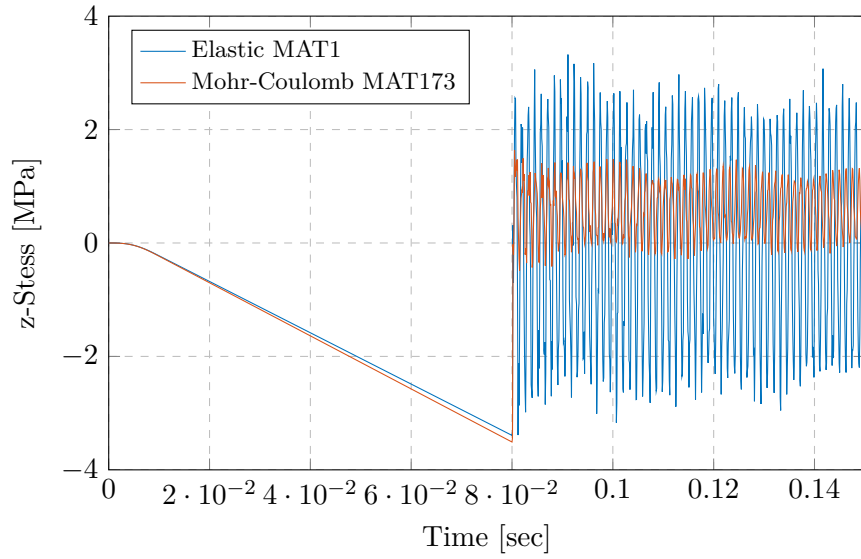


Figure 4.7.: Post failure behaviour for an elastic and the Mohr-Coulomb material MAT173 (redrawn after Herrnring; Ehlers, 2021)

4.4. Ice Extrusion Test Simulations - Quasi Rigid Structures

Having shown that the MCNS model is suitable for simulating uniaxial tensile and compression problems, the model will now be applied to the ice extrusion tests, to answer the question if the model is also able to represent the spalling and crushing of ice. This is done in the first step with 100 mm and 200 mm small-scale ice extrusion tests. In addition, the results of the 800 mm ice extrusion simulations against quasi rigid structures are presented.

The FE-model of the 200 mm ice extrusion tests is shown in Figure 4.8. In general, the structure and the confining pipe are modelled with solid elements. The contact between the pipe and the ice is implemented frictionless, since the pipe was coated with a Teflon foil. An assumed and unchanged coefficient of friction of 0.03 is used for the contact between ice and the test structure. The small coefficient of friction is chosen according to G. W. Timco; Weeks (2010) since the steel structure was covered with a very smooth Dupont Kapton HN500 foil protecting the TekScan pressure sensors. All MCNS simulations of the ice extrusion tests were performed at a velocity of 100 mm s^{-1} to achieve reasonable computation times.

As proposed in the parameter identification process (Figure 4.3), the last unknown parameter is the ice-ice friction coefficient between the detached ice elements. A significant dependence between the ice force and the friction coefficient was found. Whereby the influence increases with falling G/D -ratio. Especially simulations with a G/D -ratio of 0.125 are strongly depended on the ice-ice friction coefficient, since spalling is not a dominating failure mode for high confinement. Therefore, these simulations are used for parameter identification of the ice-ice friction coefficient. In addition also large gap

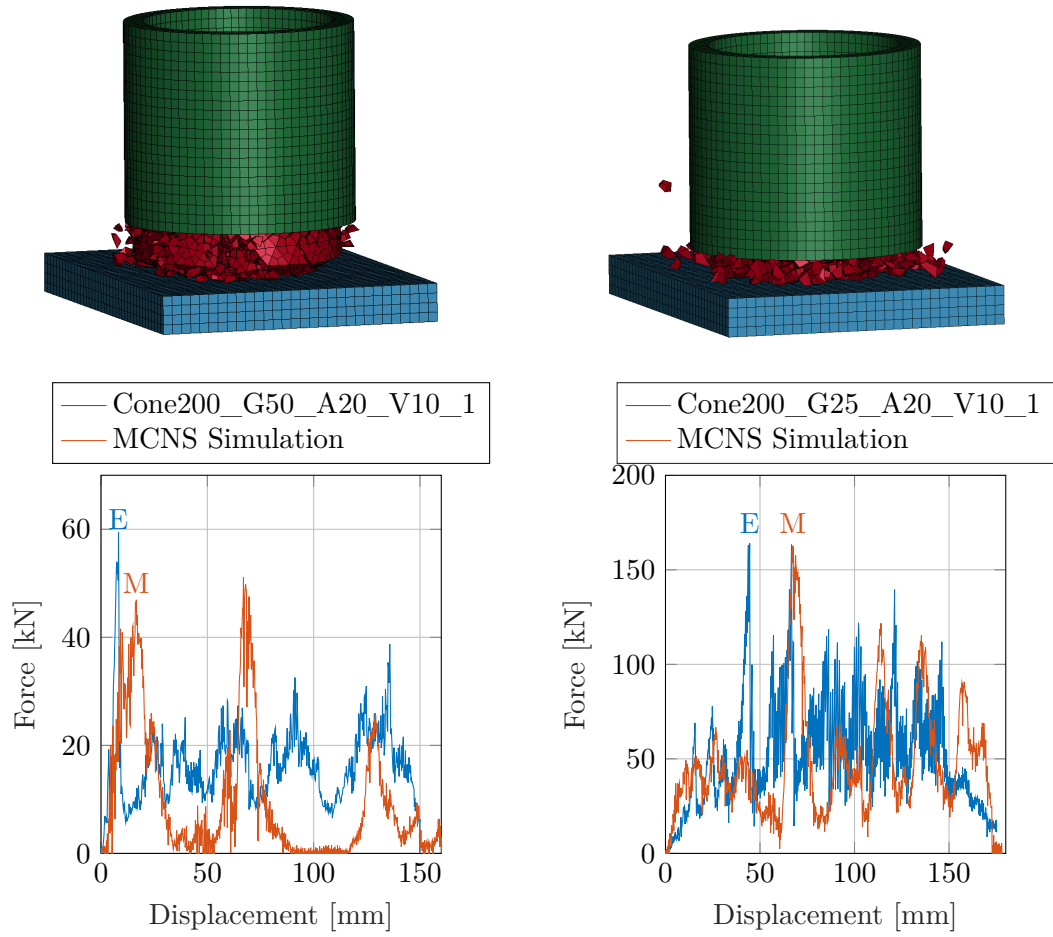


Figure 4.8.: Comparison of experiment and MCNS simulation for two exemplary ice extrusion tests with 200 mm diameter and 20° cone angle. Left: 50 mm gap height; right: 25 mm gap height. The marks E and M indicate the used frames for pressure evaluation in Figure 4.9

heights are simulated, to check the overall accuracy of the model.

A comparison of the experimental and numerical results of the MCNS model with the final parameter set for two different gap heights with a specimen diameter of 200 mm and a cone angle of 20° against a quasi ridged structure is given in Figure 4.8. The ice-ice friction coefficient was finally determined with 0.05.

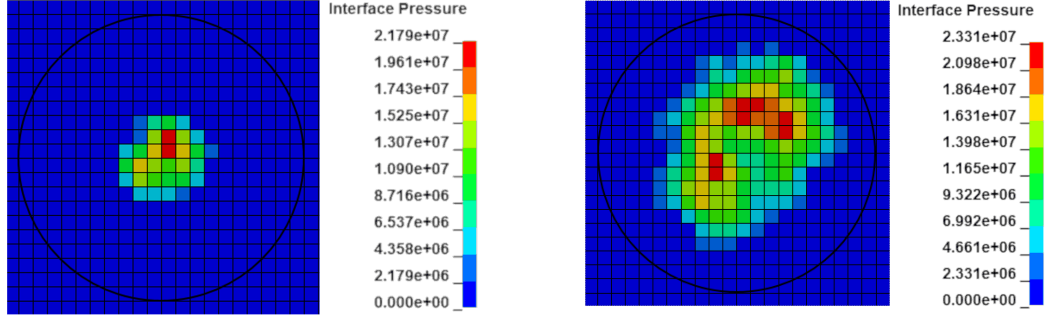
The MCNS model can reproduce satisfactorily the maximum force of both experiments. The simulated ice force increases from approximately 50 kN in case of 50 mm gap height to around 160 kN for 25 mm gap height. This behaviour is fully in line with the experiments and attributed by the confinement effect of the crushing process.

A significant force peak at the beginning characterizes the force curve of the 50 mm experiment. Large spalls are extruded in simulation when the maximum force is reached. Until global spalling occur for the first time, the pressure distribution of the simulation is circular shaped (compare Figure 4.9). Both observations are in line to the experiment. In contrast to the experiment, a second force peak appears in the simulation, which even achieves slightly higher forces than the first. This artefact is caused in the simulation by intact ice being pushed towards the structure. In reality, the damage to the specimen seems to be more extensive in the axial direction, which is not represented in the model. Therefore, only the first peak is used for further evaluation.

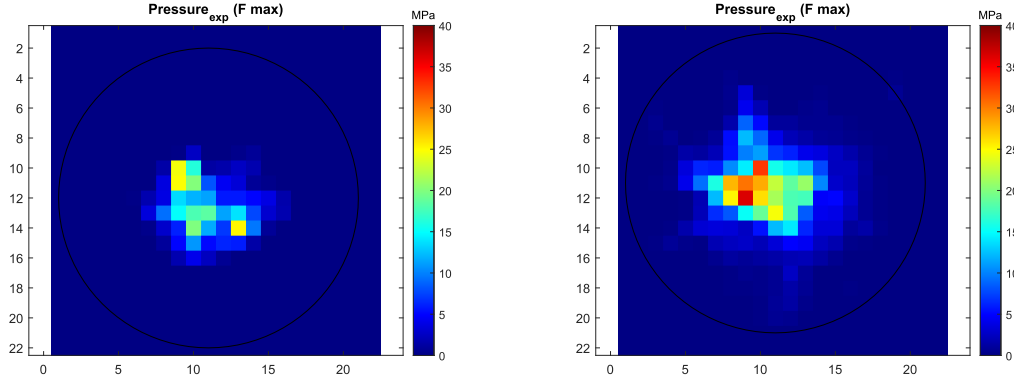
In the case of the smaller gap height of 25 mm, the maximum forces occur during the extrusion and crushing phase in the experiments and even in the simulation. Due to the high confinement, the ice elements were more plastically deformed and a significant part of the elements is eroded according to the pulverization criteria.

In line to the experiments, not only the ice load but also the contact area is increasing. A comparison of two relevant pressure patches of the considered tests is given in Figure 4.9. In the figure, the pressure image of the calibrated TekScan measurement and the contact pressure output of LS-Dyna at the time of the peak force is shown. For better comparison, the TekScan measurements were calibrated with the exponential approach according to the results in Table 3.3. In addition, the pressures of four TekScan sensels each were averaged to ensure a comparable resolution of the sensor and the FE-mesh. The measured and simulated pressure patterns are in the case of the 50 mm gap height in a very good agreement. Even the shape as well as the maximum pressure is reproduced correctly by the MCNS model. In contrast, the simulation of the 50 mm gap height correctly reproduces the loaded area, but the maximum pressures are underestimated. Moreover, the jagged shape of the ice experiment is not reproduced in this certain case.

A detailed evaluation of the loaded contact area for the same simulations is given in Figure 4.10. The figure shows the measured and simulated process–area as well as force–area data. In this evaluation, the TekScan data are only used to determine the real transient contact area. Compared to Herrnring; Ehlers (2021), the plot has been completely revised. First, the results of all three test runs performed for both gap heights were presented to show the very reproducible behaviour of the ice. Secondly, based on the new exponential calibration approach (Equation 3.3) and calibration results (Table 3.3), the lower threshold value was recalculated, resulting in a reduction of the contact area of the MCNS results. Background of the consideration is that in the case of the I-Scan measurement a default noise limit of 3 digits digital output was used. This threshold



(a) MCNS: Cone200_G50_A20, $p_{max}=21.8$ MPa, (b) MCNS: Cone200_G25_A20, $p_{max}=23.3$ MPa



(c) I-Scan: Cone200_G50_A20_V10_1, $p_{max}=25.3$ MPa, (d) I-Scan: Cone200_G25_A20_V10_1, $p_{max}=36.4$ MPa

Figure 4.9.: Comparison of the contact pressures on the structure of the MCNS simulation and the I-Scan pressure measurement for two ice extrusion tests with a diameter of 200 mm and a gap height of 50 mm (left) and 25 mm (right). For better comparison, a circle with a diameter of 200 mm is drawn in each figure. The selected frames for evaluation are indicated in Figure 4.8 with a M in case of (a) and (b) as well as with an E in case of (c) and (d)

value is also utilized during the evaluation of the MCNS results. Since the previously used power approach tended to underestimate the results due to its mathematical behaviour in the low pressure range, the new increased threshold value leads to smaller contact areas (compare also section 3.3).

As explained before, the resolution of the TekScan measurement was coarsened according to the structural FE model during post-processing. The MCNS model reflects the increase of the contact area with increasing confinement very well. Thus, the maximum loaded area increases from less than 60% for a gap height of 50 mm to 90% for a gap height of 25 mm. Especially, in case of the 25 mm simulation the maximum forces of the simulation occur at nearly the same normalised loaded area. Accordingly, the contact pressures are also represented correctly by the MCNS model. In the case of the large gap of 50 mm, the crushing behaviour seems to be a bit too weak.

Following, the large-scale ice extrusion experiments with a diameter of 800 mm were simulated with the MCNS model. The step was necessary to enable ice simulations in ship relevant dimensions. For this purpose the 800 mm, the existing model was scaled by a factor of four. The according element size is 50 mm. Without increasing the element size, the model would no longer be solvable in a reasonable time in SMP.

After applying the settings from the small-scale samples without modification, the solution was found to be unstable after the first global spalling event. As a reaction, the contact stiffness for the ice-ice single surface contact was reduced. A stable solution could already be achieved with a change of the contact stiffness factor *SFS* from 1 to 0.75. Here, the simulation underestimated the experimental force by about 30%. However, as presented in Figure 4.11 with a further reduction of the contact stiffness factor to *SFS*=0.2, the force was increased and a satisfactory agreement with the large-scale experiments was obtained.

Finally, a comparison of the maximum nominal pressures for the ice extrusion tests and the corresponding simulations with 100 mm, 200 mm and 800 mm diameter and different gap heights is given in Figure 4.12. The simulation results of the three scales are in very good agreement with the experimental results. The MCNS model reflects the significantly increasing load capacity in line with increased confinement and allows the simulation of spalling and crushing dominated problems. This is also clearly shown in Figure 4.13, where the failure behaviour of the large-scale simulations for the three investigated gap heights is illustrated.

4.5. Ice Extrusion Test Simulations - Deformable Structures

After the MCNS ice model has demonstrated its profound capabilities in simulating ice loads against rigid structures, the model is also being tested in consideration of deformable ship panels. The test set-up of the considered large-scale ice extrusion is shown in section 3.1 and the panel dimensions are given in Figure 3.6.

The consideration of deformable structures extends the numerical problem substantially. First, a suitable FE-model for thin steel structures must be found. Second, structural damping has to be considered since the weak structure tends to significant

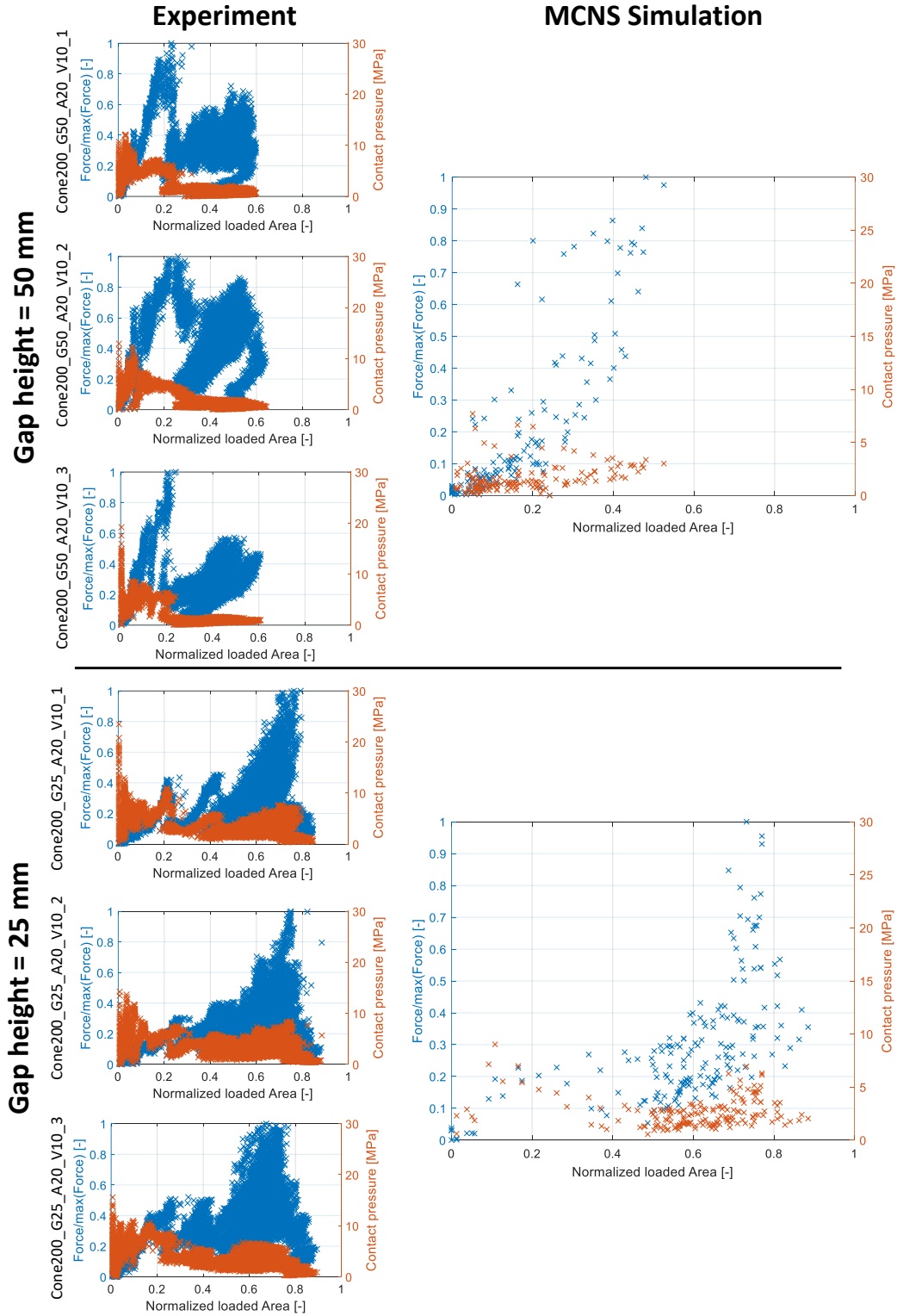


Figure 4.10.: Comparison of the force–area and process–area curves for experiments and MCNS simulations for relevant ice extrusion tests with a specimen diameter of 200 mm, a test speed of 10 mm s^{-1} and a cone angle of 20° for different gap heights

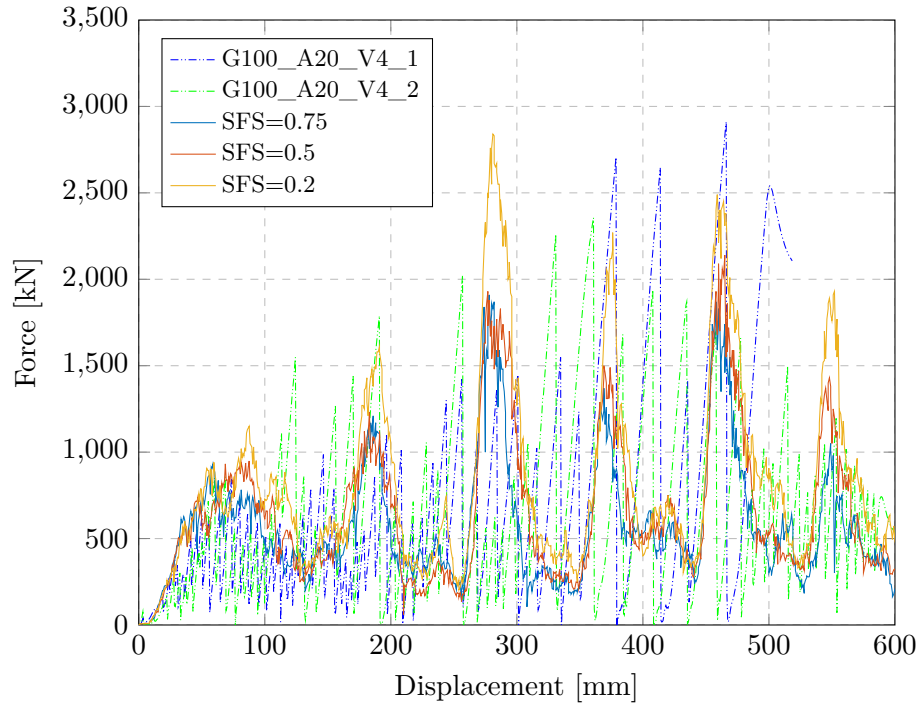


Figure 4.11.: Calibration of an appropriate ice-ice contact stiffness of the large-scale ice extrusion test simulations

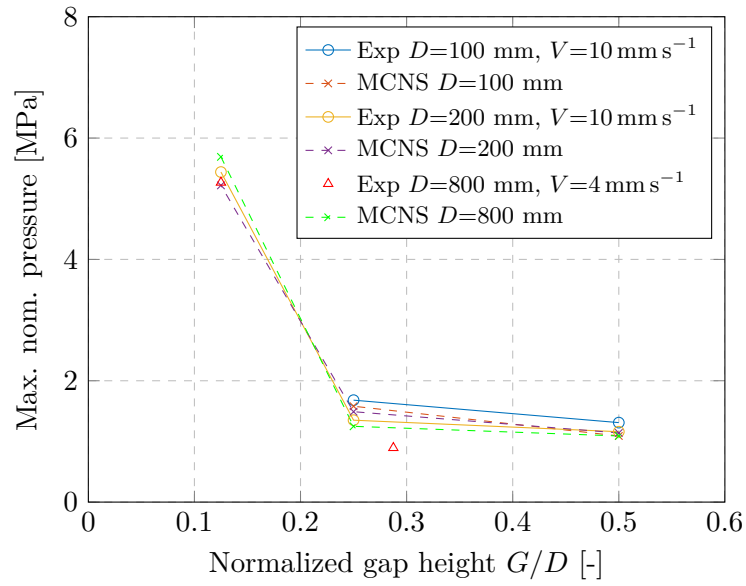


Figure 4.12.: Comparison of experimental and numerical maximum nominal peak pressures for brittle ice extrusion tests in three different scales. The experimental data is given as a mean value of the respective group

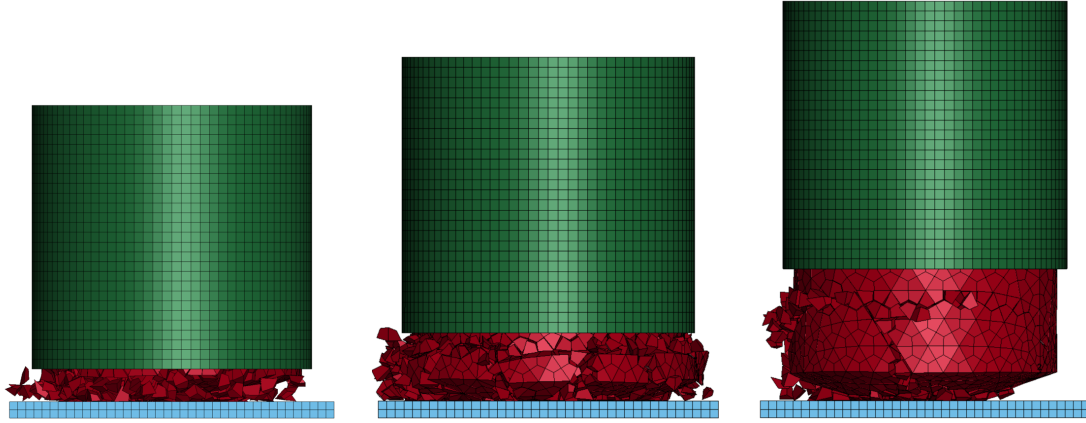


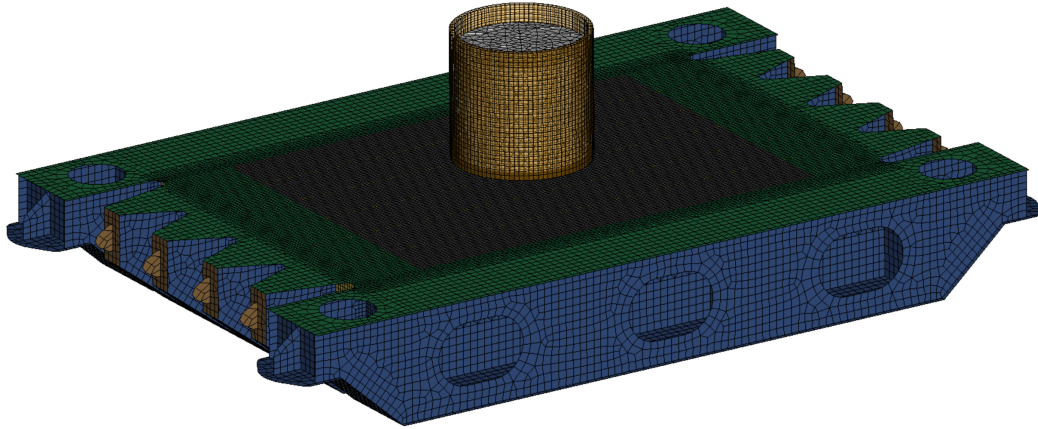
Figure 4.13.: Comparison of the failure behaviour for the three large-scale ice extrusion test simulations. Left: gap height=100 mm, centre: gap height=200 mm, right: gap height=400 mm

vibration during explicit time integration. A large number of studies already exists in the field of ship collision simulation, accordingly the findings of Martens (2014) and Schöttelndreyer (2015), which were validated on the same test rig, are used to set-up the structural FE-model.

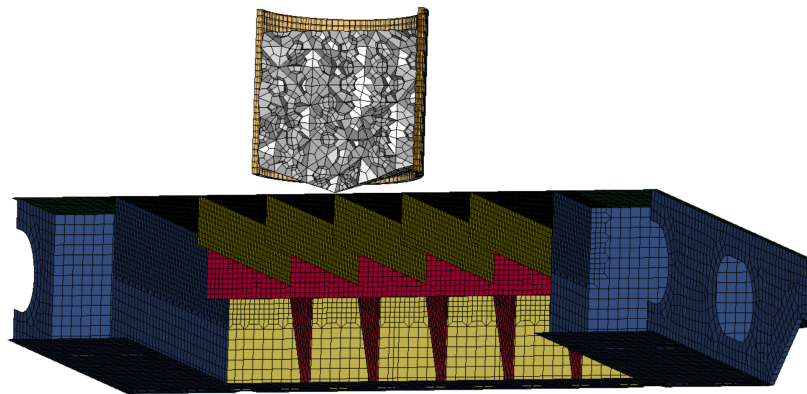
The final FE-model for the ice extrusion tests against Panel 2 is shown in Figure 4.14. The ice model and the confining pipe for the 800 mm conical specimen was taken unchanged from the quasi rigid large-scale simulations (with $SFS=0.2$ for the ice-ice contact). Compared to the previous simulations, the numerical model was extended by the stiffened test panel and the supporting frame. As in the rigid ice-extrusion test simulations, large structural components of the test apparatus such as the crosshead, base beams and abutments were neglected.

The test panel and the supporting frame were modelled with reduced integrated Belytschko-Tsay shell elements. The Belytschko-Tsay element is the default shell formulation in LS-Dyna and was utilized together with Hourglass control. The material behaviour of the test panel, which was fabricated out of S235JR steel, was implemented with the common material model `*MAT_MODIFIED_PIECEWISE_LINEAR_PLASTICITY`. A failure model for the steel structure was not implemented since no rupturing was observed during the experiments. The true stress versus true plastic strain curves, necessary for the material characterisation of the plate and stiffeners, were obtained based on the results of accompanying tensile tests. The steel material curves used in the simulations are given in Figure 4.15. The engineering stress-strain curves were analytically converted into true stress-strain curves until the tensile strength was reached. For more information please refer to the Appendix A.

For the supporting frame in which the ship-like test panel was welded, the numerically more efficient bilinear `*MAT_PLASTIC_KINEMATIC` model was chosen, since no significant plasticity was expected. The keyword decks of all used material models are given in



(a) Side view



(b) Cross-section

Figure 4.14.: Finite element model of the deformable large-scale ice extrusion tests for Panel 2

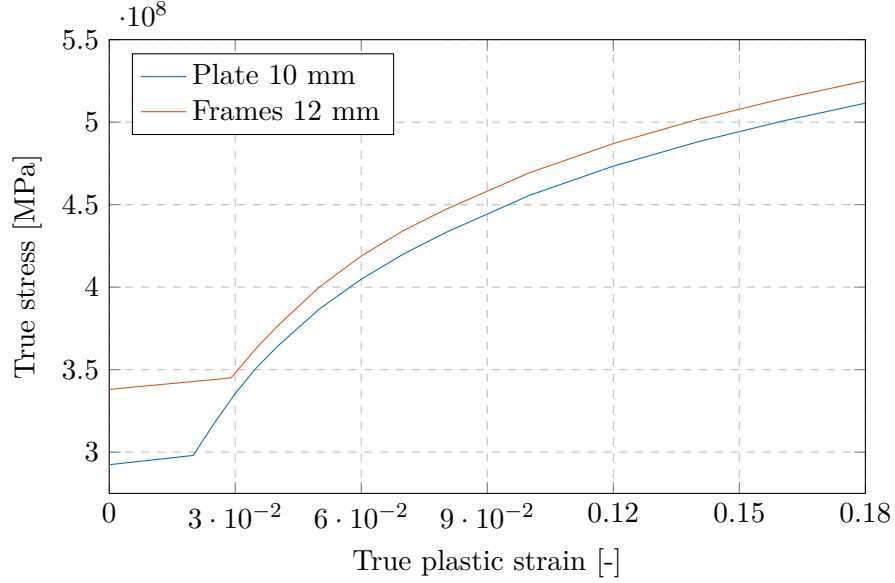


Figure 4.15.: True stress - true plastic strain curves to represent the plastic material behaviour of the simulated steel Panel 2. Frames and the plate are made from steel S235 JR.

Appendix B.

During test simulations, it became apparent that in the case of the deformable structure, large elastic vibrations of the panel are exited due to brittle-like force drops. Significant continuous oscillations of the tested panels were not observed in the experiments, thus a high damping ratio for the structure was implemented into the FE-model (`*DAMPING_PART_MASS_SET` with `sf=1000`). The damping ratio was determined by using a reduced model.

For coupling the ice and the structure the Surface-to-Surface contact formulation was used unchanged. The constant friction coefficient between structure and ice was left unchanged at 0.03 as the deformable structures were still covered with a Kapton foil (compare Figure 3.10).

In this thesis, the simulations of Panel 2 are considered, since two brittle tests with different gap heights are available for comparison. First the results of the simulation of the experiment `Cone800_Panel2_G200_A20_V4` with a gap height of 200 mm will be discussed. The experimental results are explained in section 3.5. A comparison of the simulated force-displacement curve to experimental data is made in Figure 4.16. As already observed in the brittle simulations considering rigid structures at the same G/D -ration, the force curve of the MCNS model under low confinement is characterized by a sequence of single large force peaks. Just as before (compare Figure 4.8 left), the second peak is slightly higher than the first. Presumably, crack propagation in reality takes place on a larger scale and this is not represented by the MCNS model. Therefore, only the first peak will be considered in the following.

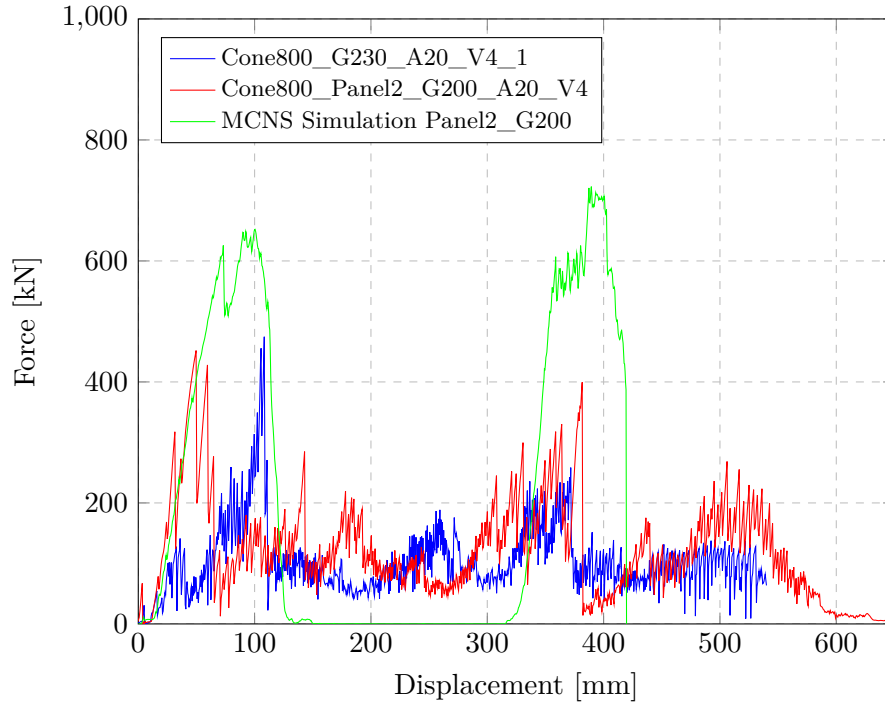


Figure 4.16.: Comparison of experiment and simulation of the deformable ice extrusion test Cone800_Panel2_G200_A20_V4

In comparison to the experimental results the maximum force of the first peak of the MCNS simulation with 652 kN is significantly higher than the measured 455 kN of the experiment. However, the obtained force is nearly identical with the previous rigid MCNS simulation which achieves a maximum force of 627 kN. Furthermore, the experimental results of the 800 mm large-scale samples with a G/D -ratio in the range of 0.25 tend to be in general significantly smaller than the studied small-scale samples with 100 mm and 200 mm diameter, which were used mainly for the parameter characterisation of the MCNS model. Therefore, the force overestimation of the MCNS model is quite reasonable.

The corresponding panel deformations after the first global peak (200 mm cylinder displacement) are shown in Figure 4.17. The plastic deformations are located mainly in the middle of the central frame (Frame 3) and in the both adjacent plate fields. The maximum deformation is 25.3 mm in the plate field and 15.7 mm in the middle of the Frame 3. Both values are much higher compared to the measured maximum plastic deformation of 5.7 mm (compare Figure 3.28).

The corresponding plastic strains after the first global force peak are given in Figure 4.18. The maximal plastic strain is below 5%. Even at the relatively low loads, the largest plastic strains are observed at the frame ends and at the joints between the plate and the frames. To prove the hypothesis that the large structural deformations were caused by the overestimated force, the simulation was run again and the ice model

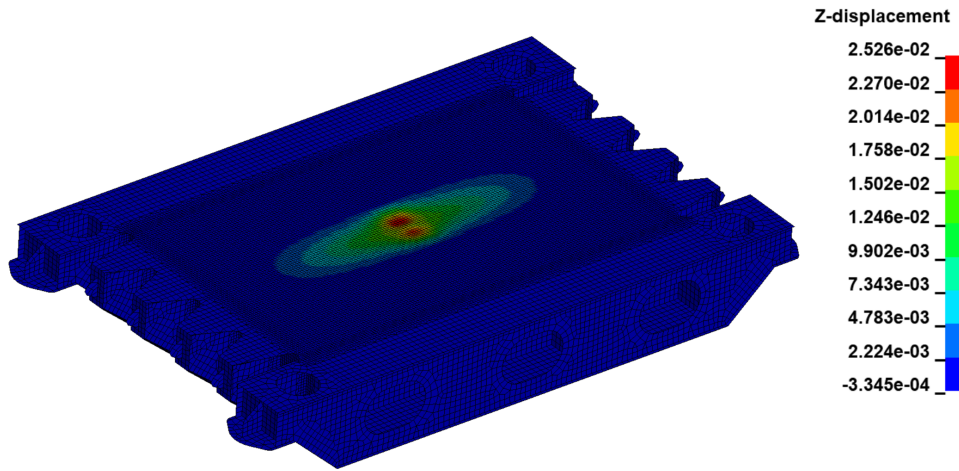


Figure 4.17.: Resulting panel deformation Konus800_G200_Panel2 for a displacement of 200 mm

was stopped and moved back when the maximum force of the experiment with 455 kN was reached. The resulting maximum plastic deformation was now 8.04 mm. Thus, the MCNS simulation overestimates the measured deformation at the same load level by only 2.3 mm.

Finally, the experiment Cone800_Panel2_G100_A20_V4 with a reduced gap height of 100 mm was simulated. The force displacement curve is presented in Figure 4.19. In line with the experiment, the MCNS simulation achieves a lower ice load in comparison to the rigid reference experiment (blue curve). As discussed in the experimental chapter, this behaviour can be explained by the gap opening evoked by the structural deformation.

Comparing the experimental and the MCNS curve, the third force peak of the experiment in particular reaches a considerably higher value than the simulation. However, this force peak occurred in the experiment directly after the conversion pause of approximately 20 min between the first and second stroke. It can be assumed that the ice properties for the first peak of the second stroke were influenced by e.g. re-freezing of cracks and tend to lead to higher loads. However, if the third force peak is neglected with its 2014 kN, the MCNS simulation is still underestimating the experimental results with a simulated maximum of 1240 kN compared to measured 1612 kN.

For many applications, such as the simulation of an iceberg collision, the technical interest is primarily on the initial force increase, since it can be assumed that the ice feature does not fail globally. In this respect the MCNS simulation gives a good representation of the force increase and seems to overestimate the first force peak which can be considered as conservative.

Due to the underestimated ice load, the resulting deformation of the structure is also lower than observed. The deformed panel shape and the associated plastic strains are

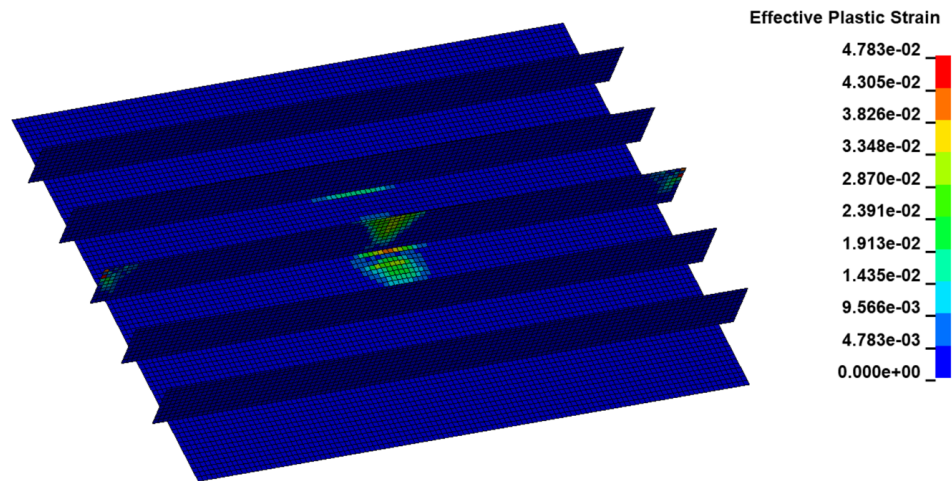


Figure 4.18.: Plastic equivalent strain of the MCNS simulation for Konus800_G200_Panel2 for a displacement of 200 mm

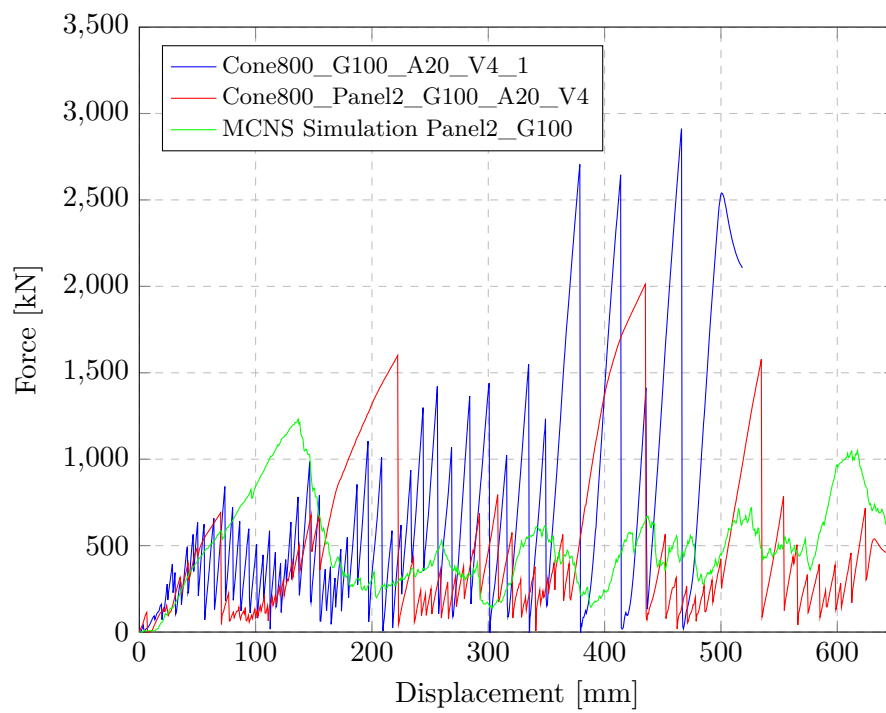


Figure 4.19.: Comparison of experiment and simulation of the deformable ice extrusion test Cone800_Panel2_G100_A20_V4

plotted in Figure 4.20 and Figure 4.21. In the simulation a maximum plastic deformation of 52.4 mm was reached. Whereas, the measured maximum displacement in experiment was 84 mm. Again, the qualitative behaviour of the plate deformation is correctly represented (compare for this also Figure 3.29). The maximum plastic strain with 13.3% does not exceed the implemented material curve. As shown in Figure 4.21 the maximum plastic strains together with frame buckling are resulted at the ends of the frames in the simulation. The same observations were also made in the experiment. In addition, there is a high bending load on the central frame as well as local plastic effects at the joints between plate and frames for frame 2 and 4.

An impression of the ice behaviour during the ice-structure interaction process is given in Figure 4.22. Broken and detached ice elements are extruded to the free edge. The ice deforms in a compliant manner around the frame, creating the final plate deformation.

Finally, the buckling and deformation behaviour of the frames is evaluated in Figure 4.23. In the figure the measured and the simulated frame deformations after the test are compared. The frame deformations and buckling modes are correctly reproduced by the MCNS model. However, the simulated plastic deformations of the frames are lower than measured, which is even related to the lower simulated ice load.

4.6. Double Pendulum Test Simulation

To show the applicability and transferability of the MCNS model also to energy limited problems a double pendulum experiment of R. Gagnon et al. (2020) was simulated. During the test, two counter-rotating pendulums of equal speed and weight collide. An ice sample is attached to one of the pendulums. The second pendulum is equipped with a flat acrylic plate, which is part of a pressure measuring device. The cone diameter was 1 m. and the cone angle 30° . The effective impact mass of both colliding bodies was approximately 4330 kg each. The impact speed of the simulated test “May22_2014” was given with 4.1 m s^{-1} . A plot of the failure pattern at $t=0.025 \text{ s}$ is presented in Figure 4.24.

In the FE-model, the same element size of 50 mm is utilized as in the simulations of the large-scale ice extrusion tests before. Material parameters, the MCNS set-up and also the contact stiffness factor *SFS* of the *CONTACT_SINGLE_SURFACE was kept unchanged at 0.2, compared to previous simulations.

As observed in the experiments, the sample fails crushing dominated. Large ice pieces were not detached. To compare the experimental force-time curve with the simulation results, the contact reaction force is computed. The simulated and measured curves are given in Figure 4.25. Both the force level as well as the qualitative behaviour were reproduced by the MCNS model.

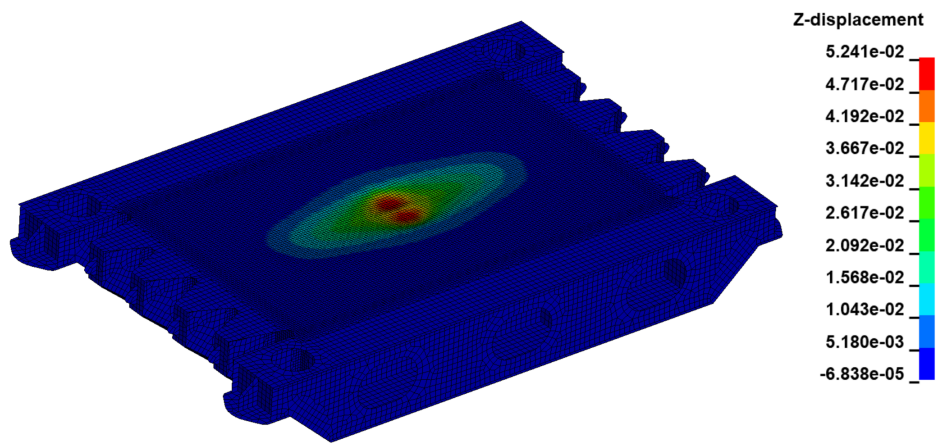


Figure 4.20.: Resulting panel deformation Cone800_Panel2_G100_A20_V4

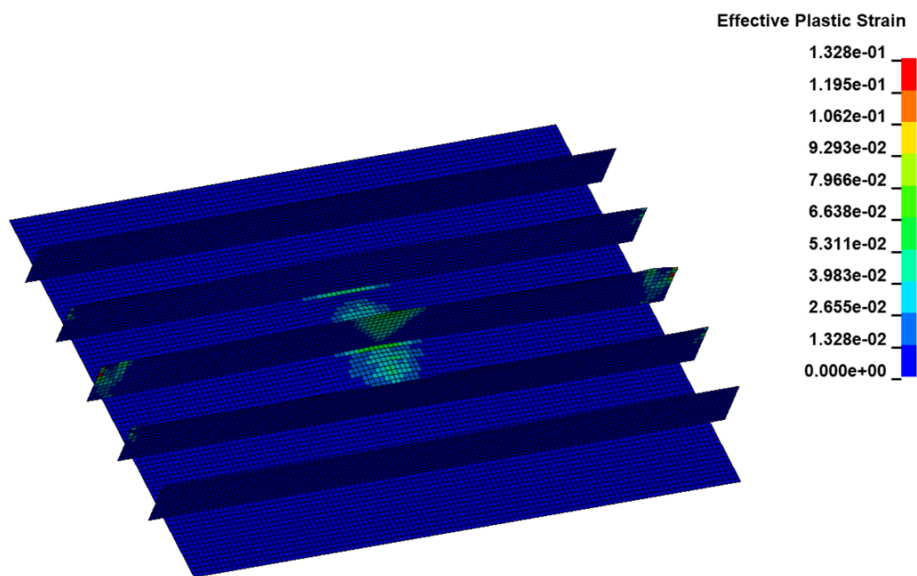


Figure 4.21.: Resulting plastic equivalent strain of the MCNS simulation for Cone800_Panel2_G100_A20_V4

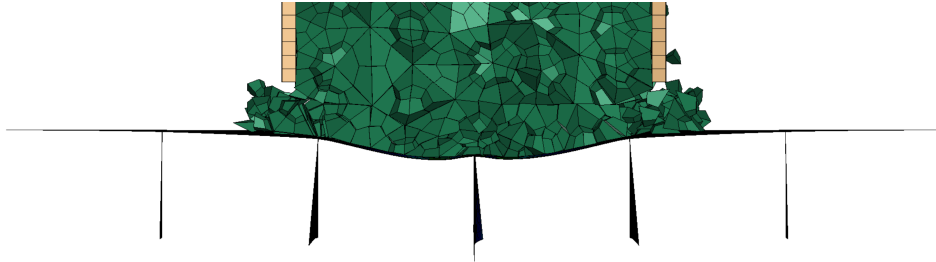


Figure 4.22.: Cross-section of the deformed panel at maximum force of the first global force peak for Cone800_Panel2_G100_A20_V4

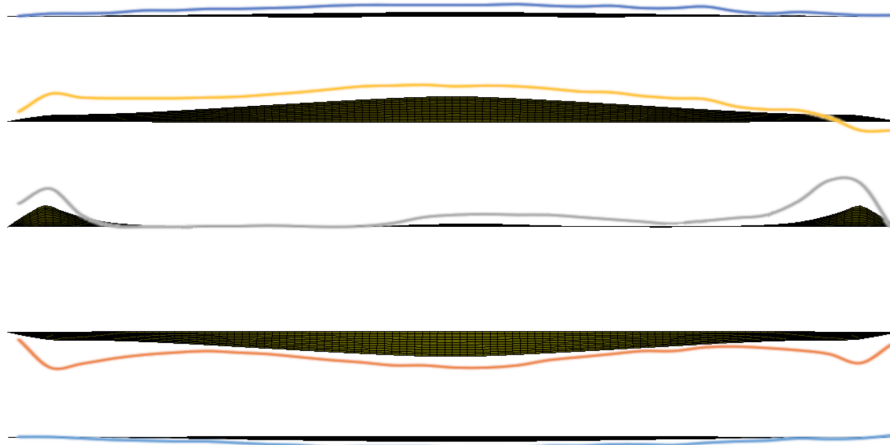


Figure 4.23.: Comparison of measured (lines) and simulated (FE-result) plastic frame deformations after the experiment Cone800_Panel2_G100_A20_V4 (deformation scale factor 5)

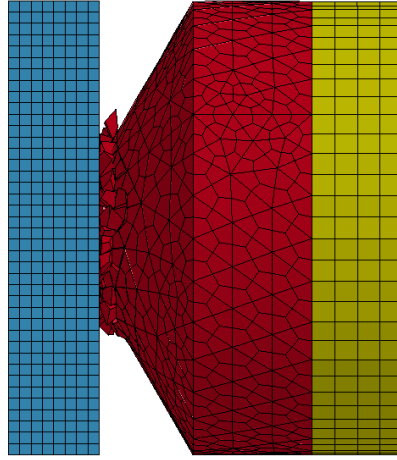


Figure 4.24.: Animation of the simulation results of the double pendulum test for $t=0.025$ s

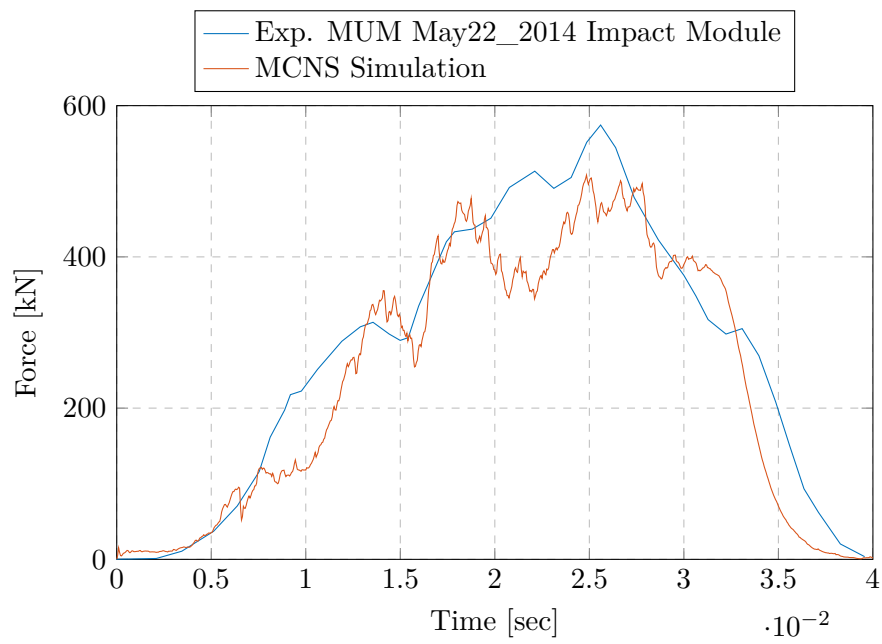


Figure 4.25.: Comparison of the measured force-time curve for the impact module of the Double Pendulum Experiment “MAY22_2014” (R. Gagnon et al., 2020) with the contact forces of the MCNS model

5. Discussion

The presented experimental results and numerical simulations allow a comprehensive insight into the ice-structure interaction process. Crushing and spalling ultimately limits the ice force acting on the structure and is therefore of great relevance in assessing the actual possible ice load.

Within the ice extrusion tests it was experimentally shown that the nominal pressures of the crushing and spalling process mainly depend on the confinement and the test velocity. The test velocity dominates the failure mode (brittle/ductile). To a lesser extent, the confinement has also an influence on the transition velocity. In the ice extrusion test experiments, the confinement was represented by the normalised gap height G/D . At high confinements the transition from ductile to brittle failure behaviour occurred at higher velocities.

The G/D -ratio itself is mainly important for the load level. With a reduction of the gap height the confinement is increased and the ice is prevented from being cleared out of the contact domain. As a result, the load increases.

Moreover, the failure mechanisms are changing accordingly to the confinement of the ice. At large normalised gap heights, spalling occurred, resulting in a completely brittle failure. The smaller the gap, the smaller the spalls became. Also the portion of pulverised ice increased. For extreme ratios as $G/D=0.0625$ only powder was extruded. According to Schulson; Duval (2009) and Golding (2011) a change from Coulombic dominated faulting, for low confinements respectively large normalised gap heights, to Plastic faulting for at high confinement is expected. In case of Coulombic faulting spalling is the dominating failure mechanism. With decreasing gap height spalling is more and more suppressed the Plastic failure mechanism together with pulverisation of the ice gets more dominant. The pulverised ice will be extruded since the shear stiffness decreases under increasing pressure (Stephen J. Jones, 1982) and at a certain point the damaged layer gets unstable. This is also accompanied by a more plastic-like force response of the ice.

The tested cone angles of 30°, 20° and 10° did lead to a small change in the maximum forces for large normalised gap heights. This is in line with results of Tuhkuri (1995). However, cylindrical specimens (without a tip) allow considerably higher ice loads under unconfined conditions, but produce more uniform pressure patch and thus represent a different loading case. However, for high G/D -ratios the initial ice shape has no influence on the global peak forces within the ice extrusion tests, since the maximum forces occurred only in the cylindrical part of the specimen.

As shown in Figure 3.20, the influence of the specimen diameter on the nominal pressures and thus the pressure-area effect seems to be marginal for the investigated case. The nominal pressures of the different specimen diameters are almost the same

at the same G/D -ratio and test speed. It should be noted that the ratio between the gap area ($\pi \cdot D/2 \cdot G$) and the nominal contact area was kept constant for the different specimen diameters by the choice of equal G/D -ratios. Overall, the confinement situation of the ice is considerably more important for the ice load than the area of the contact surface.

Caused by spalling the experimental results indicate a clear trend of a reduced contact area in case of brittle failure. The obtained values in Figure 3.21 for a low confinement situation are fully in line with Takeuchi et al. (2001). In brittle mode and a G/D of 0.5 approximately 15% to 35% of the nominal area is loaded at maximum force. This is also in line with load assumption in the FSICR rules (Finnish Transport Safety Agency, 2017). With increasing confinement, the loaded area also increases, which could be for example evident in case of an iceberg collision.

Compared to the rigid tests, the ice forces of the deformable ice extrusion tests are lower, in case of a significant deformation of the test panel (compare Figure 5.1). This observation is explained by the increase of the gap height and corresponding decrease of the ice confinement during the test, which is resulted by the structural deformation of the panel. Therefore, the ice loads of rigid and deformable tests cannot be directly compared because of different confinement conditions.

Nevertheless, it can be seen that the failure frequency is reduced in the case of the deformable structures. The observation is in accordance with Browne et al. (2013). It is assumed that this behaviour is attributable to the lower structural stiffness of the panel compared to the quasi-rigid structure.

The obtained experimental results were also compared with literature values. Tuhkuri (Tuhkuri, 1993; Tuhkuri, 1995) conducted ice-structure interaction experiments with a similar concept to the ice extrusion test. During the tests confined wedge shaped freshwater ice blocks were pushed against different test structures. The ice temperature was also -10°C . To compare the results a cone respectively wedge angle of 30° and a test velocity of 10 mm s^{-1} were chosen for the ice extrusion test and the reference data of Tuhkuri. The results are given in Figure 5.2. To calculate the normalised gap height, the specimen diameter was still used for the ice extrusion tests and the ice block thickness in case of the experiments of Tuhkuri. In both data sets, an increase in ice load for decreasing gap heights could be seen. In general, the maximum nominal pressures of both test series were in the same range.

Based on the results of the ice extrusion test a new ice material model was developed. Overall, the MCNS model achieves a good representation of spalling and crushing dominated problems. The dependency between the nominal contact pressures of the ice-extrusion tests and the gap height was well represented, with unchanged and consistent material properties. The model is applicable against rigid and deformable structures as well as for force and energy limited problems.

Most model parameters have a physical meaning and are associated with specific physical processes. Spalling, continuum deformation, pressure melting, the ice self-contact and pulverization were considered in the MCNS model. As shown in the experiments all these mechanisms are essential for the ice-structure interaction process. Spalling reduces the contact area considerably compared to the nominal area and thus causes an

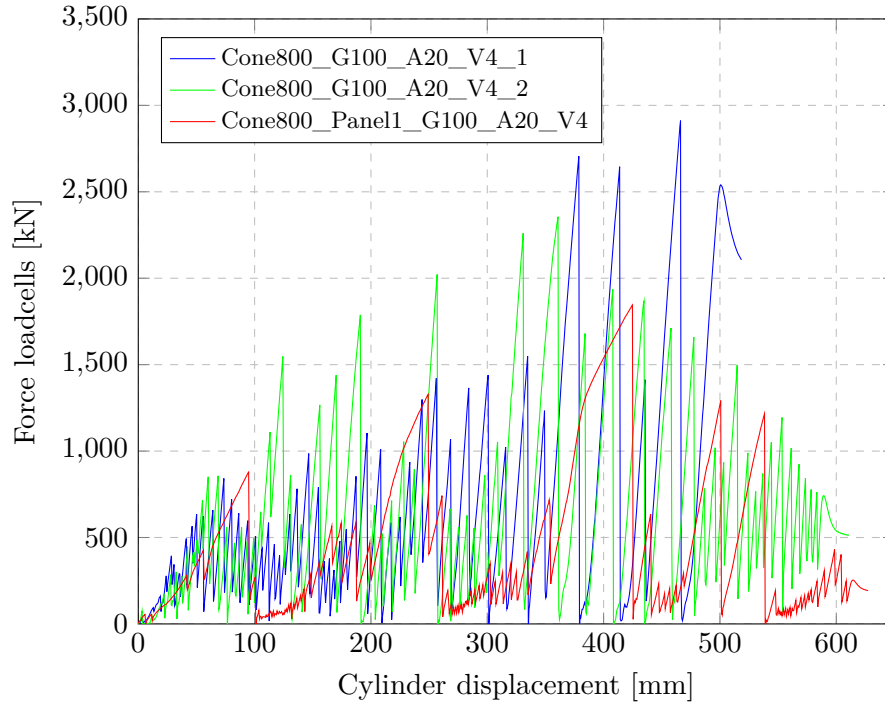


Figure 5.1.: Comparison rigid and deformable large-scale ice extrusion tests

increase of the real contact pressure. Previous models were unable to reproduce this effect (Mokhtari et al., 2022). Furthermore, the deformable MCNS simulations show the need for a proper ice material model. For example, rigid or elastic ice models could hardly reflect the compliant material behaviour of ice (compare Figure 4.22). Only the combination of crushing and spalling implemented in MCNS allows an accurate estimate of the maximum ice forces for a specific collision-scenario. By neglecting spalling failure the forces would be much too conservative, especially in case of low confined ice.

However, it must be clearly stated that some parts of the MCNS model have been largely simplified and assumed. This applies to the continuum behaviour of the crushed ice material, the friction coefficient for the ice-ice contact, and the pulverization mechanism. Accordingly, the parameters used, provide a basis for further modelling and analyses.

To motivate the real ice behaviour the MCNS model is plotted against experimental data in Figure 5.3. On the right side a strong increase in the maximum shear stress with increasing hydrostatic pressure can be seen. After the certain point the shear stress is not further increasing. This is accompanied by a change from brittle to plastic failure (Stephen J. Jones, 1982; Mizuno, 1998). Golding (2011) explains the change of the material behaviour by different failure mechanisms. At high confinement the ice fails due to Plastic faulting. The material behaviour gets ductile because frictional sliding is suppressed. Whereas for low confinements and hydrostatic pressures, Coulombic shear faulting can be found (Schulson; Duval, 2009; C. E. Renshaw et al., 2014). Along with

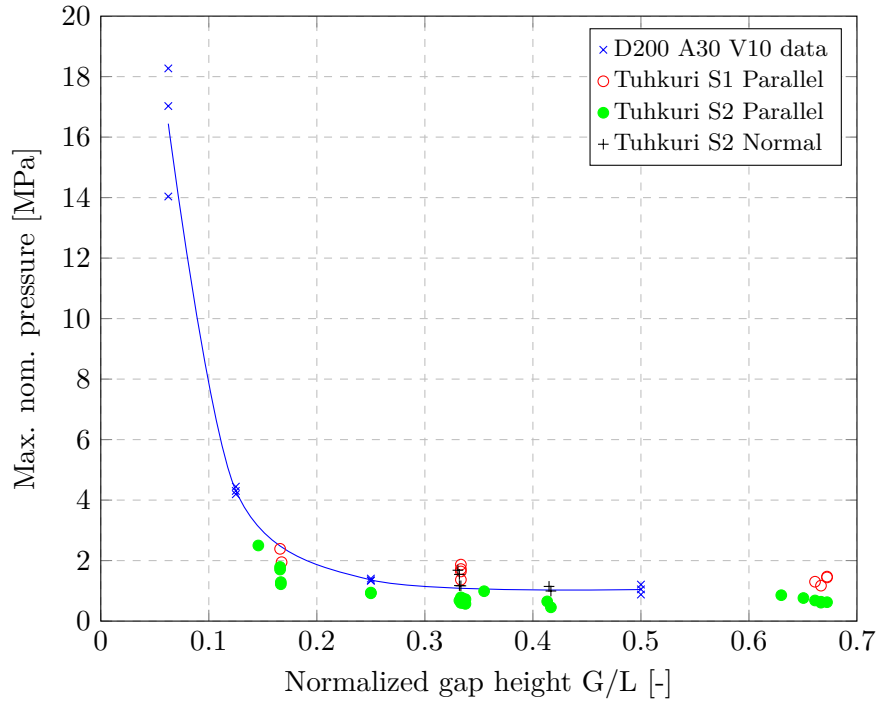


Figure 5.2.: Comparison of the ice extrusion tests against results of Tuhkuri (Tuhkuri, 1993; Tuhkuri, 1995). Only tests with a test speed of 10 mm and a cone respectively wedge angle of 30° are considered

Coulombic behaviour are strong force drops and the typical brittle-like force curve is apparent. This observations are consistent with the extrusion tests results.

Furthermore, a decreasing tendency of the maximum shear stresses with increasing hydrostatic pressure in the plastic domain is observed. This behaviour can probably be explained as the ice becomes more and more fluid-like the closer it gets to the melting pressure. Possible reasons for the effect could be increased dynamic recrystallisation and accompanying grain boundary melting processes under high pressure. The enhanced fluid-like behaviour of ice is also consistent with own observations during the ice extrusion experiments. To achieve high pressures above approximately 70 MPa, the smallest gaps must be closed, otherwise the ice escapes.

Unlike observed in the experiments by Stephen J. Jones (1982) and Mizuno (1998), a maximum shear stress is not considered in the MCNS model. This idealisation of the MCNS model is likely to be conservative under high confinement conditions.

As discussed in the state of the art chapter C. E. Renshaw et al. (2014) describes for fully unconfined ice failure a change from Coulombic shear failure to axial splitting (e.g. in case unconfined uniaxial compression test). The axial splitting mechanism is mostly driven by mode I failure and outgoing from wing cracks (Golding, 2011). Axial splitting is not represented in the MCNS model. Therefore, the MCNS model will overestimate the strength for problems driven by axial splitting.

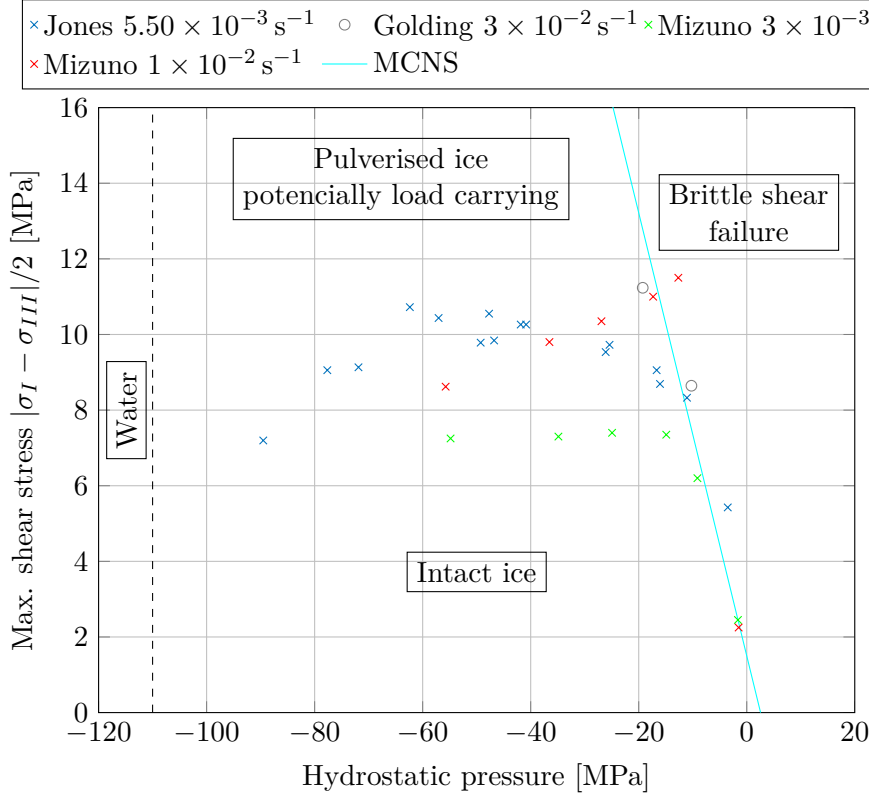


Figure 5.3.: A plot of the peak shear stress over peak pressure for experimental results of Stephen J. Jones (1982), Mizuno (1998), and Golding (2011) for polycrystalline ice between -11.5°C and -10°C . The hydrostatic pressure is given as $1/3 \cdot (\sigma_I + \sigma_{II} + \sigma_{III})$. The melting pressure is given according to Feistel et al. (2006)

As shown in the Figure 4.11 the contact stiffness and the selected contact algorithms have a crucial influence on the results of the MCNS model. Due to the complex contact conditions, the MCNS model is numerically more expansive than conventional FE models. Nevertheless, the time-step sizes are within a normal range. However, the fraction of broken ice appears to be too large compared to the experimental observations at high confinement. In the future it may be possible to improve the physical representation of failure and reduce the influence of the ice-ice contact, if the failure strain within the `*CONSTRAINED_TIED_NODES_FAILURE` card is modelled as a function of the stress state. The failure model GISSMO, which was developed for the simulation of vehicle collisions, allows this functionality (Neukamm, 2018). GISSMO enables to model the failure strain in dependency to the triaxiality. This allows the definition of an increased failure strain in triaxial compression together with the low and still brittleness-like value for tension-dominated stress conditions.

Moreover, the simulation of ice crushing processing against deformable ship panels has proved to be challenging. The results regarding the first inertial global spalling event

are more robust than the ones in the following crushing phase. The results for the low confined deformable ice-extrusion test simulation were conservatively overestimated in respect to the forces and panel deformations. In the case of the significant confinement, the ice load was unfortunately underestimated. Nevertheless, the structural behaviour could already be reproduced qualitatively correctly. In addition, the limitation should have no influence on the simulations of collisions with an single unconfined ice feature. This was also demonstrated by the successful simulation of the double pendulum experiment in section 4.6.

During the deformable ice extrusion tests it was shown that the frames tend to buckle due to the point-like loading. Bulb profiles or T-profiles may be favourable compared to the used slender flat bars.

For the efficient simulation of real full-scale ship-ice interaction problems, most likely the elements used in this thesis are too small. Therefore, a methodology will be proposed in the following to condition the MCNS model for arbitrary element sizes based on the presented data:

1. Select the structural and ice domain to be simulated.
2. Create the finite element model. To limit computation time, the MCNS model should only be used in areas where significant deformation and failure of the ice is expected. Away from the contact domain, the ice can be modelled without node splitting and a simple elastic material model.
3. Verify and calibrate the MCNS material model in case of a new element size against the quasi rigid ice extrusion test results (Figure 3.20). The nominal ice pressures expect to be nearly independent of the diameter. Therefore, the experimental dimensions and force curves can be scaled. A scaled version of the rigid ice extrusion test presented in the dissertation can be simulated. In the event of deviations, it is advisable to tune first the contact stiffness of the ice-ice contact.
4. Run the simulations in SMP. The use of MPP is at the moment not verified.
5. Set-up and run the final full-scale ship-ice interaction according to the recommendations in this thesis section 4.1 and together with the new verified parameters.

6. Conclusion

In this thesis, the results of the newly developed ice extrusion test and MCNS ice model were presented. The core idea of the ice extrusion test is to investigate a continuous ice-structure interaction process and enable high ice loads during laboratory tests. The transition from ductile to brittle failure was observed above a velocity of 1 mm s^{-1} . A comprehensive test campaign showed a strong dependence between the nominal ice pressure (crushing strength) and the normalised gap height. For a large normalised gap height, which is equivalent to low confinement condition, the brittle ice failure is dominated by spalling. With decreasing normalised gap height, the ice becomes constrained in the contact zone which increases the crushing strength due to a larger confinement. At high confinement the spalling of ice is suppressed. The ice fails via pure crushing and the global behaviour becomes more plastic.

For the actual loading of ship structures, the effective contact area of the ice is of great importance. In the case of nearly unconfined conditions, as expected in case of a collision with an ice floe, only 15% to 35% of the nominal area was pressurized in brittle mode. For high confined ice, the effective loaded area increased up to 60% of the nominal contact area.

In the experiments, a clear influence of the nominal contact area on the ice pressures could not be detected. In this work the nominal contact area of the largest to the smallest specimen was varied with a factor of 64. However, the maximum nominal peak pressures were almost the same for constant test speeds and the same normalized gap height. According to the experimental results, for brittle ice failure the confinement is the most significant influencing factor on the load level. This observation needs to be further investigated with respect to the commonly used pressure-area approach used for example in the ISO19006 (International Organization for Standardization, 2010).

Based on these experimental results, the novel MCNS ice model has been developed for different low and medium confined ice-structure interaction problems. The MCNS model has been implemented and utilized in the explicit finite element solver LS-Dyna. The model was successfully validated against the small- and large-scale ice extrusion and double pendulum tests. The simulation results could satisfactorily reproduce loads and contact areas. Based on the proposed conditioning process, full-scale ice-ship simulations are feasible in the future. Due to the utilized nodal split technique, the MCNS modelling strategy enables the simulation of spalling, which is commonly not considered in ice-structure interaction simulations. Of course, the MCNS model is still not perfect and needs further development. The complex contact definition remains challenging and poses risks in terms of robust results. A proposal to reduce the fraction of detached failed elements was documented. In addition, an extension of the model to include maximum shear stress associated with high hydrostatic pressures would be desirable.

Bibliography

- LS-DYNA® AEROSPACE WORKING GROUP, 2017. *Modeling Guidelines Document*. No. 17-1. Available also from: <https://awg.lstc.com/tiki-index.php?page=Resources>.
- AMDAHL, J., 2019. Impact from ice floes and icebergs on ships and offshore structures in Polar Regions. In: *IOP Conference Series: Materials Science and Engineering*. Vol. 700, p. 012039. Available from DOI: 10.1088/1757-899X/700/1/012039.
- AMIRI, Ardalan, 2018. Similar Overestimation of Sandstone Bending Strength by Coupled FEM-SPH Based Linear Drucker Prager and Discrete Element Based Bonded Particles: Calibration & Diagnosis. In: *15th Annual International Conference on Modelling and Simulation (ICMS)*. Ottawa, Canada.
- ASHBY, M. F.; JONES, David R. H., 1986. *Engineering materials 2: An introduction to microstructures, processing and design*. Vol. v.39. Oxford: Pergamon. International series on materials science and technology. ISBN 0-08-032532-7.
- ASTM INTERNATIONAL, 2013. *E0112-13: Test Methods for Determining Average Grain Size*. West Conshohocken, PA. Available from DOI: 10.1520/E0112-13.
- BANDA, O.; GOERLANDT, F.; MONTEWKA, J.; KUJALA, P., 2014. Winter navigation at the Baltic Sea: An analysis of accidents occurred during winters 2002–2003 & 2009–2013. In: NOWAKOWSKI, Tomasz; MŁYŃCZAK, Marek; JODEJKO-PIETRUCZUK, Anna; WERBIŃSKA-WOJCIECHOWSKA, Sylwia (eds.). *Safety and Reliability: Methodology and Applications*. CRC Press. Vol. 1, pp. 83–92. ISBN 978-1-138-02681-0. Available from DOI: 10.1201/b17399-14.
- BERGSTRÖM, Martin; BROWNE, Thomas; EHLERS, Sören; HELLE, Inari; HERRN-RING, Hauke; KHAN, Faisal; KUBICZEK, Jan; KUJALA, Pentti; KÖRGESAAR, Mihkel; LEIRA, Bernt Johan; PARVIAINEN, Tuuli; POLOJÄRVI, Arttu; SUOMI-NEN, Mikko; TAYLOR, Rocky; TUHKURI, Jukka; VANHATALO, Jarno; VEITCH, Brian, 2022. A comprehensive approach to scenario-based risk management for Arctic waters. *Ship Technology Research*, pp. 1–29. ISSN 0937-7255. Available from DOI: 10.1080/09377255.2022.2049967.
- BETTIN, Horst; SPIEWECK, Frank, 1990. Die Dichte des Wassers als Funktion der Temperatur nach Einführung der Internationalen Temperaturskala von 1990. *PTB Mitteilungen*. Vol. 100, no. 03, pp. 195–196.
- BOBARU, Florin, 2020. The performance of peridynamic and phase-field models in dynamic brittle fracture. In: *Workshop on Experimental and Computational Fracture Mechanics 2020*, p. 7.

- BOCK UND POLACH, Franz R. U. von; KLEIN, Marco; KUBICZEK, Jan; KELLNER, Leon; BRAUN, Moritz; HERRNRING, Hauke, 2019. State of the Art and Knowledge Gaps on Modelling Structures in Cold Regions. In: *Proceedings of the International Conference on Offshore Mechanics and Arctic Engineering*. Vol. OMAE2019-95085. Available from DOI: 10.1115/OMAE2019-95085.
- BOCK UND POLACH, Rüdiger von; EHLERS, Sören, 2013. Model scale ice — Part B: Numerical model. *Cold Regions Science and Technology*. Vol. 94, pp. 53–60. ISSN 0165232X. Available from DOI: 10.1016/j.coldregions.2013.06.009.
- BRIMACOMBE, Jill M.; WILSON, David R.; HODGSON, Antony J.; HO, KAREN C. T.; ANGLIN, Carolyn, 2009. Effect of Calibration Method on Tekscan Sensor Accuracy. *Journal of Biomechanical Engineering*. Vol. 131, no. 3, pp. 1–4. ISSN 01480731. Available from DOI: 10.1115/1.3005165.
- BROWNE, T.; TAYLOR, R.; JORDAAN, I.; GÜRTNER, A., 2013. Small-scale ice indentation tests with variable structural compliance. *Cold Regions Science and Technology*. Vol. 88, pp. 2–9. ISSN 0165232X. Available from DOI: 10.1016/j.coldregions.2012.12.006.
- BRUNEAU, S.; COLBOURNE, B.; DRAGT, R.; DILLENBURG, A.; RITTER, S.; PILLING, M.; SULLIVAN, A., 2013. Laboratory indentation tests simulating ice-structure interactions using cone-shaped ice samples and steel plates. In: *Proceedings of the 22nd International Conference on Port and Ocean Engineering under Arctic Conditions*.
- BURG, J.P.; WILSON, C.J.L.; MITCHELL, J.C, 1986. Dynamic recrystallization and fabric development during the simple shear deformation of ice. *Journal of Structural Geology*. Vol. 8, no. 8, pp. 857–870. ISSN 0191-8141. Available from DOI: 10.1016/0191-8141(86)90031-3.
- CANADIAN COAST GUARD, 2012. *Ice Navigation in Canadian Waters*. Ottawa, Ontario. ISBN 978-1-100-20610-3.
- COLE, David M., 1979. Preparation of polycrystalline ice specimens for laboratory experiments. *Cold Regions Science and Technology*. Vol. 1, no. 2, pp. 153–159. ISSN 0165232X. Available from DOI: 10.1016/0165-232X(79)90007-7.
- CROASDALE, K. R.; MORGENSTERN, N. R.; NUTTALL, J. B., 1977. Indentation tests to investigate ice pressures on vertical piers. *Journal of Glaciology*. Vol. 19, no. 81, pp. 301–312. Available from DOI: 10.3189/S0022143000029361.
- DANILOV, Peter B., 2021. Cargo Volume and Transit Traffic on the NSR Increased in 2021. *High North News* [online] [visited on 2021-11-30]. Available from: <https://www.highnorthnews.com/en/cargo-volume-and-transit-traffic-nsr-increased-2021>.
- DERRADJI-AOUAT, Ahmed, 2003. Multi-surface failure criterion for saline ice in the brittle regime. *Cold Regions Science and Technology*. Vol. 36, no. 1-3, pp. 47–70. ISSN 0165232X. Available from DOI: 10.1016/S0165-232X(02)00093-9.

- ELVIN, Alex A., 1996. Number of grains required to homogenize elastic properties of polycrystalline ice. *Mechanics of Materials* [online]. Vol. 22, no. 1, pp. 51–64 [visited on 2018-01-06]. ISSN 01676636. Available from DOI: 10.1016/0167-6636(95)00024-0.
- ERCEG, Boris; TAYLOR, Rocky; EHLERS, Sören; LEIRA, Bernt J., 2014. A Response Comparison of a Stiffened Panel Subjected to Rule-Based and Measured Ice Loads. In: vol. Volume 10: Polar and Arctic Science and Technology. International Conference on Offshore Mechanics and Arctic Engineering. Available from DOI: 10.1115/OMAE2014-23874.
- FEISTEL, Rainer; WAGNER, Wolfgang, 2006. A New Equation of State for H₂O Ice Ih. *Journal of Physical and Chemical Reference Data*. Vol. 35, no. 2, pp. 1021–1047. ISSN 0047-2689. Available from DOI: 10.1063/1.2183324.
- FELLIN, Wolfgang, 2013. *Einführung in Eis-, Schnee- und Lawinenmechanik*. Berlin, Heidelberg: Springer Vieweg. ISBN 3642259626.
- FINNISH TRANSPORT SAFETY AGENCY, 2017. *Finnish-Swedish Ice Class Regulations 2017*. Helsinki.
- FREDERKING, R; JORDAAN, IJ; MCCALLUM, JS, et al., 1990. Field tests of ice indentation at medium scale, Hobson's Choice Ice Island, 1989. In: *Proceedings of 10th International Symposium on Ice*. Espoo, Finland. Vol. 2, pp. 931–944.
- GAGNON, R.; ANDRADE, S. L.; QUINTON, B.; DALEY, C.; COLBOURNE, B., 2020. Pressure distribution data from large double-pendulum ice impact tests. *Cold Regions Science and Technology*. Vol. 175. ISSN 0165232X. Available from DOI: 10.1016/j.coldregions.2020.103033.
- GAGNON, R. E., 1994. Generation of melt during crushing experiments on freshwater ice. *Cold Regions Science and Technology*. Vol. 22, no. 4, pp. 385–398. ISSN 0165232X. Available from DOI: 10.1016/0165-232X(94)90022-1.
- GAGNON, R. E., 1999. Consistent observations of ice crushing in laboratory tests and field experiments covering three orders of magnitude in scale. In: *International Conference on Port and Ocean Engineering under Arctic Conditions*. Espoo, Finland, pp. 858–869.
- GAGNON, R. E., 2011. A numerical model of ice crushing using a foam analogue. *Cold Regions Science and Technology*. Vol. 65, no. 3, pp. 335–350. ISSN 0165232X. Available from DOI: 10.1016/j.coldregions.2010.11.004.
- GAGNON, R. E.; GAMMON, P. H., 1995. Triaxial experiments on iceberg and glacier ice. *Journal of Glaciology*. Vol. 41, no. 139, pp. 528–540. ISSN 0022-1430. Available from DOI: 10.1017/S0022143000034869.
- GOERLANDT, Floris; GOITE, Habtamnesh; VALDEZ BANDA, Osiris A.; HÖGLUND, Anders; AHONEN-RAINIO, Paula; LENSU, Mikko, 2017. An analysis of wintertime navigational accidents in the Northern Baltic Sea. *Safety Science*. Vol. 92, pp. 66–84. ISSN 09257535. Available from DOI: 10.1016/j.ssci.2016.09.011.

- GOLD, L., 1977. Engineering Properties of Fresh-Water Ice. *Journal of Glaciology*. Vol. 19, no. 81, pp. 197–212. Available from DOI: 10.3189/S0022143000215608.
- GOLDING, Narayana, 2011. *Compressive Shear Faulting in Ice Loaded Triaxially: The Influence of Confinement*. Hanover, New Hampshire. Doctoral Thesis. Thayer School of Engineering.
- GRENNERAT, F.; MONTAGNAT, M.; CASTELNAU, O.; VACHER, P.; MOULINEC, H.; SUQUET, P.; DUVAL, P., 2012. Experimental characterization of the intragranular strain field in columnar ice during transient creep. *Acta Materialia* [online]. Vol. 60, no. 8, pp. 3655–3666 [visited on 2017-08-02]. ISSN 13596454. Available from DOI: 10.1016/j.actamat.2012.03.025.
- GROSS, Dietmar; SEELIG, Thomas, 2016. *Bruchmechanik: Mit einer Einführung in die Mikromechanik*. Berlin, Heidelberg: Springer. ISBN 978-3-662-46736-7.
- GUDIMETLA, P. S. Reddy; COLBOURNE, Bruce; DALEY, Claude; BRUNEAU, Stephen E.; GAGNON, Robert, 2012. Strength and Pressure Profiles of Conical Ice Crushing Experiments. In: *SNAME International Conference and Exhibition on Performance of Ships and Structures in Ice*. Banff, Alberta, Canada. Available from DOI: 10.5957/ICETECH-2012-132.
- GÜRTNER, Arne, 2009. *Experimental and Numerical Investigations of Ice-Structure Interaction*. Trondheim. Doctoral thesis. NTNU.
- HÄNNINEN, Samuli, 2005. *Incidents and accidents in winter navigation in the Baltic Sea, winter 2002-2003*. Vol. no 54. [Helsinki] and [Tukholma]: Finnish Maritime Administration and Swedish Maritime Administration. Research report / Winter Navigation Research Board. ISBN 9789514921049.
- HÄRER, Robin, 2019. *Compression tests of laboratory-made freshwater ice*. Hamburg: Institute for Ship Structural Design and Analysis. Available from DOI: 10.15480/882.2728. Project Thesis. Hamburg University of Technology.
- HERRNRING, Hauke; EHLERS, Sören, 2021. A Finite Element Model for Compressive Ice Loads Based on a Mohr-Coulomb Material and the Node Splitting Technique. *Journal of Offshore Mechanics and Arctic Engineering*. Vol. 144, no. 2. Available from DOI: 10.1115/1.4052746.
- HERRNRING, Hauke; KELLNER, Leon; KUBICZEK, Jan M.; EHLERS, Sören, 2018. Simulation of Ice-Structure Interaction with CZM-Elements. In: *German LS-DYNA Forum 2018*. Bamberg, Germany.
- HERRNRING, Hauke; KUBICZEK, Jan M.; EHLERS, Sören, 2020. The Ice Extrusion Test: A novel Test Setup for the Investigation of Ice-Structure Interaction – Results and Validation. *Ships and Offshore Structures*. Vol. 15, no. sup1, pp. 1–9. ISSN 1744-5302. Available from DOI: 10.1080/17445302.2020.1713437.
- HOBBS, Peter Victor, 2010. *Ice physics*. Oxford: Oxford Univ. Press. Oxford classic texts in the physical sciences. ISBN 9780199587711.

- HUDSON, John; HARRISON, John, 1997. *Engineering Rock Mechanics: An Introduction to the Principles*. Elsevier. ISBN 9780080438641. Available from DOI: 10.1016/B978-0-08-043864-1.X5000-9.
- HUMPERT, Malte, 2020. Cargo Volume on Northern Sea Route Remains Stable at 32m tons in 2020. *High North News* [online] [visited on 2021-11-30]. Available from: <https://www.highnorthnews.com/en/cargo-volume-northern-sea-route-remains-stable-32m-tons-2020>.
- IAATO, 2019. *Tourism in Antarctica, 2019*.
- INCE, Serdar Turgut; KUMAR, Ankush; PAIK, Jeom Kee, 2016. A new constitutive equation on ice materials. *Ships and Offshore Structures*. Vol. 12, no. 5, pp. 610–623. ISSN 1744-5302. Available from DOI: 10.1080/17445302.2016.1190122.
- INCE, Serdar Turgut; KUMAR, Ankush; PARK, Dae Kyeom; PAIK, Jeom Kee, 2017. An advanced technology for structural crashworthiness analysis of a ship colliding with an ice-ridge: Numerical modelling and experiments. *International Journal of Impact Engineering*. Vol. 110, pp. 112–122. Available from DOI: 10.1016/j.ijimpeng.2017.02.014.
- INTERNATIONAL ASSOCIATION OF CLASSIFICATION SOCIETIES, 2019. *Requirements concerning POLAR CLASS*.
- INTERNATIONAL MARITIME ORGANIZATION, 2016a. *Guidance on methodologies for assessing operational capabilities and limitations in ice*.
- INTERNATIONAL MARITIME ORGANIZATION, 2016b. *International code for ships operating in polar waters (POLAR CODE)*.
- INTERNATIONAL ORGANIZATION FOR STANDARDIZATION, 2010. *ISO 19906:2010: Petroleum and natural gas industries – Arctic offshore structures*. Berlin: Beuth Verlag GmbH.
- INTERNATIONAL ORGANIZATION FOR STANDARDIZATION, 2016. *ISO 6892-1:2016: Metallic materials - Tensile testing - Part 1: Method of test at room temperature; German version DIN EN ISO 6892-1:2016*. Berlin: Beuth Verlag GmbH.
- ISSC, 2015. *ISSC Report: Arctic technology*. Cascais, Portugal.
- J.H. CURRIER; E.M. SCHULSON AND W.F. ST. LAWRENCE, 1983. *A study on the tensile strength of ice as a function of grain size*. CRREL Report 83-14.
- JOHNSTON, M. E.; CROASDALE, Ken R.; JORDAAN, Ian J., 1998. Localized pressures during ice–structure interaction: relevance to design criteria. *Cold Regions Science and Technology*. Vol. 27, pp. 105–117. ISSN 0165232X. Available from DOI: 10.1016/S0165-232X(97)00026-8.
- JONES, Stephen J., 1982. The Confined Compressive Strength of Polycrystalline Ice. *Journal of Glaciology*. Vol. 28, no. 98, pp. 171–178. ISSN 0022-1430. Available from DOI: 10.1017/S0022143000011874.

- JONES, Stephen J., 2007. A review of the strength of iceberg and other freshwater ice and the effect of temperature. *Cold Regions Science and Technology*. Vol. 47, no. 3, pp. 256–262. ISSN 0165232X. Available from DOI: 10.1016/j.coldregions.2006.10.002.
- JORDAAN, Ian; LI, Chuanke; SUDOM, Denise; STUCKEY, Paul; RALPH, Freeman, 2005. Principles for local and global ice design using pressure-area relationships. In: *Proceedings of the International Conference on Port and Ocean Engineering Under Arctic Conditions*.
- JORDAAN, Ian; TIMCO, Garry, 1988. Dynamics of the ice-crushing process. *Journal of Glaciology*. Vol. 34, no. 118, pp. 318–326. Available from DOI: 10.3189/S0022143000007085.
- JORDAAN, Ian J., 2001. Mechanics of ice–structure interaction. *Engineering Fracture Mechanics*. Vol. 68, no. 17-18, pp. 1923–1960. ISSN 00137944. Available from DOI: 10.1016/S0013-7944(01)00032-7.
- KÄMÄRÄINEN, Jorma; RISKA, Kaj, 2017. Ice Class Rules and International Regulations. In: *Encyclopedia of Maritime and Offshore Engineering*. John Wiley&Sons, pp. 1–10. ISBN 9781118476406. Available from DOI: 10.1002/9781118476406.emoe.018.
- KELLNER, Leon, 2022. *Analyzing the complexity of ice with explainable machine learning for the development of an ice material model*. Available from DOI: 10.15480/882.4076. Doctoral thesis. Technische Universität Hamburg.
- KELLNER, Leon; LU, Wenjun; SÖREN, Ehlers; HØYLAND, Knut V., 2021. Study on the Cohesive Edge Crack in a Square Plate with the Cohesive Element Method. *International Journal of Fracture* [online]. Vol. 231, no. 1, pp. 21–41 [visited on 2020-12-30]. Available from DOI: 10.1007/s10704-021-00560-9.
- KELLNER, Leon; STENDER, Merten; BOCK UND POLACH, Rüdiger U. Franz von; HERRNRING, Hauke; EHLERS, Sören; HOFFMANN, Norbert; HØYLAND, Knut V., 2019. Establishing a common database of ice experiments and using machine learning to understand and predict ice behavior. *Cold Regions Science and Technology*. Vol. 162, pp. 56–73. ISSN 0165232X. Available from DOI: 10.1016/j.coldregions.2019.02.007.
- KESSLER, Daniel, 2014. *Best Practise in Crash Analysis and LS-Dyna Tools*. Bamberg. LS-Dyna Forum Bamberg.
- KIM, E.; GOLDING, N.; SCHULSON, E. M.; LØSET, S.; RENSHAW, C. E., 2012. Mechanisms governing failure of ice beneath a spherically-shaped indenter. *Cold Regions Science and Technology*. Vol. 78, pp. 46–63. ISSN 0165232X. Available from DOI: 10.1016/j.coldregions.2012.01.011.
- KIM, Ekaterina; AMDAHL, Jørgen, 2016. Discussion of assumptions behind rule-based ice loads due to crushing. *Ocean Engineering*. Vol. 119, pp. 249–261. ISSN 00298018. Available from DOI: 10.1016/j.oceaneng.2015.09.034.

- KIM, Hyunwook; DALEY, Claude; COLBOURNE, Bruce, 2015. A numerical model for ice crushing on concave surfaces. *Ocean Engineering*. Vol. 106, pp. 289–297. ISSN 00298018. Available from DOI: 10.1016/j.oceaneng.2015.07.020.
- KOLARI, Kari, 2007. *Damage mechanics model for brittle failure of transversely isotropic solids: Finite element implementation*. Espoo. Doctoral thesis. Helsinki University of Technology.
- KOLARI, Kari, 2017. A complete three-dimensional continuum model of wing-crack growth in granular brittle solids. *International Journal of Solids and Structures*. Vol. 115–116, pp. 27–42. ISSN 00207683. Available from DOI: 10.1016/j.ijsolstr.2017.02.012.
- KOLARI, Kari; KURKELA, Juha, 2012. *Ship-Ice Collision Analysis*. No. VTT-R-07666-12.
- KUBICZEK, Jan M.; BURCHARD, Kim S.; EHLERS, Sören; SCHÖTTELNDREYER, Martin, 2017. Material relationship identification for finite element analysis at intermediate strain rates using optical measurements. In: *Progress in the Analysis and Design of Marine Structures*. CRC Press, pp. 459–468.
- KUBICZEK, Jan M.; HERRNRING, Hauke; KELLNER, Leon; RUCKERT, Phil; EHLERS, Sören, 2022. Ice pressure measurements with TekScan - sensor behavior, calibration and application limits. In: *Proceedings of the ASME 2022 41st International & Conference on Ocean, Offshore and Arctic Engineering OMAE 2022*.
- KUJALA, Pentti, 1991. *Damage statistics of ice-strengthened ships in the Baltic Sea 1984-1987*. Espoo.
- KURDYUMOV, V. A.; KHEISIN, D. E., 1976. Hydrodynamic model of the impact of a solid on ice. *Soviet Applied Mechanics*. Vol. 12, no. 10, pp. 1063–1068. ISSN 0038-5298. Available from DOI: 10.1007/BF00885056.
- LANDE ANDRADE, Sthéfano; ELRUBY, Ahmed Y.; HIPDITCH, Evan; DALEY, Claude G.; QUINTON, Bruce W. T., 2022. Full-scale ship-structure ice impact laboratory experiments: experimental apparatus and initial results. *Ships and Offshore Structures*, pp. 1–15. ISSN 1744-5302. Available from DOI: 10.1080/17445302.2022.2032993.
- LI, Xiaoyang; OTSUKA, Natsuhiko, 2019. Overview of recent shipping activities along the Northern Sea Route. In: *Proceedings of the 8th CECAR*. Tokyo, Japan.
- LIU, Zhenhui; AMDAHL, Jørgen; LØSET, Sveinung, 2011. Plasticity based material modelling of ice and its application to ship-iceberg impacts. *Cold Regions Science and Technology*. Vol. 65, no. 3, pp. 326–334. ISSN 0165232X. Available from DOI: 10.1016/j.coldregions.2010.10.005.
- LLOYD’S REGISTER, 2016. *The International Code for Ships Operating in Polar Waters: A regulatory interpretation guide*.
- LSTC, 2019a. *LS-DYNA Keyword User’s Manual: Volume I*. Ed. by LIVERMORE SOFTWARE TECHNOLOGY CORPORATION.

- LSTC, 2019b. *LS-DYNA Theory Manual*. Ed. by LIVERMORE SOFTWARE TECHNOLOGY CORPORATION.
- LU, Wei; LI, Mingyang; VAZIC, Bozo; OTERKUS, Selda; OTERKUS, Erkan; WANG, Qing, 2020. Peridynamic Modelling of Fracture in Polycrystalline Ice. *Journal of Mechanics*. Vol. 2, pp. 1–12. Available from DOI: 10.1017/jmech.2019.61.
- MÄÄTTÄNEN, Mauri; MARJAVAARA, Pieti; SAARINEN, Sami; LAAKSO, Matti, 2011. Ice crushing tests with variable structural flexibility. *Cold Regions Science and Technology*. Vol. 67, no. 3, pp. 120–128. ISSN 0165232X. Available from DOI: 10.1016/j.coldregions.2011.03.004.
- MACKEY, T.; WELLS, J.; JORDAAN, I.; DERRADJI-AOUAT, A., 2007. Experiments on the fracture of polycrystalline ice. In: *Proceedings of the International Conference on Port and Ocean Engineering Under Arctic Conditions*. Dalian, China, pp. 339–349.
- MARCHENKO, Nataliya, 2014. Floating ice induced ship casualties. In: *Proceedings of the 22nd IAHR International Symposium on Ice*. Singapore, pp. 908–915. Available from DOI: 10.3850/978-981-09-0750-1.
- MARTENS, Ingo, 2014. *Konstruktive Aspekte beim Entwurf von Bugwülsten zur Verbesserung des Energieaufnahmevermögens bei Schiffskollisionen*. Available from DOI: 10.15480/882.1192. Doctoral thesis. Technische Universität Hamburg.
- MASTERSON, D. M.; FREDERKING, R. M. W.; WRIGHT, B.; KARNA, T.; MADDOCK, W. P., 2007. A revised ice pressure-area curve. In: *Proceedings of the International Conference on Port and Ocean Engineering under Arctic Conditions, POAC*, pp. 305–314.
- MASTERSON, D.M.; JORDAAN, Ian; FREDERKING, R.; SPENCER, Paul, 1993. Description of multi-year ice indentation tests at Hobson’s choice ice island - 1990. *Proceedings of the International Conference on Offshore Mechanics and Arctic Engineering - OMAE*. Vol. 4, pp. 145–155.
- MELANSON, P. L.; MEGLIS, I. L.; JORDAAN, I. J.; STONE, B. M., 1999. Microstructural change in ice: I. Constant-deformation-rate tests under triaxial stress conditions. *Journal of Glaciology*. Vol. 45, pp. 417–422. Available from DOI: 10.3189/S0022143000001271.
- MICHALOUDIS, Georgios, 2019. *Numerical Modeling of Embedded Interfaces based on Frictional Contact Formulations with a Covariant Description*. Munich. Doctoral Thesis. Universität der Bundeswehr München.
- MICHALOUDIS, Georgios; BLANKENHORN, Gunther; MATTERN, Steffen; SCHWEIZERHOF, Karl, 2010. Modelling Structural Failure with Finite Element Analysis of Controlled Demolition of Buildings by Explosives Using LS-DYNA. In: NAGEL, Wolfgang E.; KRÖNER, Dietmar B.; RESCH, Michael M. (eds.). *High Performance Computing in Science and Engineering '09*. Berlin, Heidelberg: Springer Berlin Heidelberg, pp. 539–551. ISBN 978-3-642-04664-3. Available from DOI: 10.1007/978-3-642-04665-0_37.

- MINISTRY OF DEFENCE, 2022. *The UK's Defence Contribution in the High North* [online]. [visited on 2022-04-29]. Available from: <https://www.gov.uk/government/publications/the-uks-defence-contribution-in-the-high-north>.
- MIZUNO, Yukiko, 1998. Effect of Hydrostatic Confining Pressure on the Failure Mode and Compressive Strength of Polycrystalline Ice. *The Journal of Physical Chemistry B*. Vol. 102, no. 2, pp. 376–381. ISSN 1520-6106. Available from DOI: 10.1021/jp963163b.
- MOKHTARI, Mojtaba; KIM, Ekaterina; AMDAHL, Jørgen, 2022. Pressure-dependent plasticity models with convex yield loci for explicit ice crushing simulations. *Marine Structures*. Vol. 84, p. 103233. ISSN 09518339. Available from DOI: 10.1016/j.marstruc.2022.103233.
- NEUKAMM, Frieder, 2018. *Lokalisierung und Versagen von Blechstrukturen*. Available from DOI: 10.18419/opus-10082. Doctoral Thesis. Universität Stuttgart.
- NOWACKI, Horst, 2010. Five decades of Computer-Aided Ship Design. *Computer-Aided Design*. Vol. 42, no. 11, pp. 956–969. ISSN 00104485. Available from DOI: 10.1016/j.cad.2009.07.006.
- OÑATE, Eugenio; OWEN, Roger, 2011. *Particle-Based Methods: Fundamentals and Applications*. Vol. 25. Dordrecht: Springer Science+Business Media B.V. Computational Methods in Applied Sciences. ISBN 978-94-007-0734-4. Available from DOI: 10.1007/978-94-007-0735-1.
- PALMER, A. C.; DEMPSEY, J. P.; MASTERSON, D. M., 2009. A revised ice pressure-area curve and a fracture mechanics explanation. *Cold Regions Science and Technology*. Vol. 56, no. 2-3, pp. 73–76. ISSN 0165232X. Available from DOI: 10.1016/j.coldregions.2008.11.009.
- PETROVIC, J. J., 2003. Review Mechanical properties of ice and snow. *Journal of Materials Science*. Vol. 38, no. 1, pp. 1–6. ISSN 00222461. Available from DOI: 10.1023/A:1021134128038.
- POPOV; FADDEYEV; KHEYSIN; YAKOVLEV, 1969. *Strength of sailing ships in ice: Technical translation*. Leningrad. No. FSTC-HT-23-96-68.
- QUINTON, Bruce WT; DALEY, Claude G; GAGNON, Robert E, 2012. Realistic moving ice loads and ship structural response. In: *The Twenty-second International Offshore and Polar Engineering Conference*. OnePetro.
- RALSTON, Terrance D., 1977. Yield and plastic deformation in ice crushing failure. *Sea Ice Processes and Models, Proceedings of the Arctic Ice Dynamics Joint Experiment, edited by RS Pritchard*, pp. 234–245.
- RENSHAW, Carl; SCHULSON, Erland, 2001. Universal behaviour in compressive failure of brittle materials. *NATURE*. Vol. 412, pp. 897–900. Available from DOI: 10.1038/35091045.
- RENSHAW, Carl E.; GOLDING, Narayana; SCHULSON, Erland M., 2014. Maps for brittle and brittle-like failure in ice. *Cold Regions Science and Technology*. Vol. 97, pp. 1–6. ISSN 0165232X. Available from DOI: 10.1016/j.coldregions.2013.09.008.

- RISKA, Kaj, 1991. Observations of the line-like nature of ship-ice contact. In: *Proceedings of the 11th International Conference on Port and Ocean Engineering under Arctic Conditions*. St. John's, Canada.
- RISKA, Kaj, 2010. *Design of Ice Breaking Ships*. Eolss Publishers, Oxford, UK.
- RISKA, Kaj, 2022. Ice Action on Ship Hull: What Do We Know and What Do We Miss? In: TUHKURI, Jukka; POLOJÄRVI, Arttu (eds.). *IUTAM Symposium on Physics and Mechanics of Sea Ice*. Cham: Springer International Publishing, pp. 103–129. ISBN 978-3-030-80439-8.
- RIST, M. A.; JONES, S. J.; SLADE, T. D., 1994. Microcracking and shear fracture in ice. *Annals of Glaciology*. Vol. 19, pp. 131–137. ISSN 0260-3055. Available from DOI: 10.3189/1994AoG19-1-131-137.
- RIST, M. A.; MURRELL, S.A.F, 1994. Ice triaxial deformation and fracture. *Journal of Glaciology*. Vol. 40, no. 135, pp. 305–318. ISSN 0022-1430. Available from DOI: 10.1017/S0022143000007395.
- ROSE, Jerry G; STITH, Jason C, 2004. Pressure measurements in railroad trackbeds at the rail/tie interface using Tekscan sensors. In: *American Railway Engineering and Maintenance-of-Way Assoc. 2004 Annual Conference PROCEEDINGS, Nashville, TN, September*.
- RÖSLER, Joachim; HARDERS, Harald; BÄKER, Martin, 2016. *Mechanisches Verhalten der Werkstoffe*. 5th ed. Wiesbaden: Springer Vieweg. ISBN 9783658137953. Available from DOI: 10.1007/978-3-658-13795-3.
- SANDERSON, Timothy J.O., 1988. *Ice mechanics: Risks to offshore structures*. London: Graham & Trotman. ISBN 086010785X.
- SATO, Koichi; OKAFUJI, Takashi, 2013. Study on Strength of LNG Carrier against Ice Impact. *Journal of the Japan Society of Naval Architects and Ocean Engineers* [online]. Vol. 18, pp. 63–71 [visited on 2017-06-17]. Available from DOI: 10.2534/jjasnaoe.18.63.
- SAVAGE, S. B.; SAYED, M.; FREDERKING, R.M.W., 1992. Two-dimensional extrusion of crushed ice. Part 2: analysis. *Cold Regions Science and Technology*. Vol. 21, no. 1, pp. 37–47. ISSN 0165232X. Available from DOI: 10.1016/0165-232X(92)90004-E.
- SAYED, Mohamed; FREDERKING, Robert M.W., 1992. Two-dimensional extrusion of crushed ice. Part 1: experimental. *Cold Regions Science and Technology*. Vol. 21, no. 1, pp. 25–36. ISSN 0165232X. Available from DOI: 10.1016/0165-232X(92)90003-D.
- SAZIDY, Mahmud Sharif, 2015. *Development of velocity dependent ice flexural failure model and application to safe speed methodology for polar ships*. St John's. Doctoral Thesis. Memorial University of Newfoundland.
- SCHNEIDER, Daniel; SCHOOFF, Ephraim; HUANG, Yunfei; SELZER, Michael; NESTLER, Britta, 2016. Phase-field modeling of crack propagation in multiphase systems. *Computer Methods in Applied Mechanics and Engineering*. Vol. 312, pp. 186–195. Available from DOI: 10.1016/j.cma.2016.04.009.

- SCHÖTTELNDREYER, Martin, 2015. *Füllstoffe in der Konstruktion: Ein Konzept zur Verstärkung von Schiffsseitenhüllen*. Available from DOI: 10.15480/882.1258. Doctoral thesis. Technische Universität Hamburg.
- SCHULSON, Erland M., 1999. The structure and mechanical behavior of ice. *JOM*. Vol. 51, no. 2, pp. 21–27. ISSN 1047-4838. Available from DOI: 10.1007/s11837-999-0206-4.
- SCHULSON, Erland M.; DUVAL, Paul, 2009. *Creep and fracture of ice*. Cambridge: Cambridge Univ. Press. ISBN 9780521806206.
- SCHWARZ, J.; FREDERKING, R.; GAVRILLO, V.; PETROV, I.G.; HIRAYAMA, K.-I.; MELLOR, M.; TRYDE, P.; VAUDREY, K.D., 1981. Standardized testing methods for measuring mechanical properties of ice. *Cold Regions Science and Technology*. Vol. 4, no. 3, pp. 245–253. ISSN 0165-232X. Available from DOI: 10.1016/0165-232X(81)90007-0.
- SINGH, S. K.; JORDAAN, I. J., 1996. Triaxial tests on crushed ice. *Cold Regions Science and Technology*. Vol. 24, no. 2, pp. 153–165. ISSN 0165232X.
- SODHI, D.; TAKEUCHI, T.; NAKAZAWA, N.; AKAGAWA, S.; SAEKI, H., 2006. Ice pressure measured during joia indentation tests. In: *Proceedings of the 18th IAHR International Symposium on Ice*. Japan, pp. 199–206.
- SODHI, Devinder S., 2001. Crushing failure during ice–structure interaction. *Engineering Fracture Mechanics*. Vol. 68, no. 17-18, pp. 1889–1921. ISSN 00137944. Available from DOI: 10.1016/S0013-7944(01)00038-8.
- SOLAKIVI, Tomi; KIISKI, Tuomas; OJALA, Lauri, 2019. On the cost of ice: estimating the premium of Ice Class container vessels. *Maritime Economics & Logistics*. Vol. 21, no. 2, pp. 207–222. ISSN 1479-2931. Available from DOI: 10.1057/s41278-017-0077-5.
- STONE, B. M.; JORDAAN, I. J.; XIAO, J.; JONES, S. J., 1997. Experiments on the damage process in ice under compressive states of stress. *Journal of Glaciology*. Vol. 43, no. 143, pp. 11–25. Available from DOI: 10.3189/S002214300000277X.
- SUOMINEN, Mikko; KUJALA, Pentti; ROMANOFF, Jani; REMES, Heikki, 2017. The effect of the extension of the instrumentation on the measured ice-induced load on a ship hull. *Ocean Engineering*. ISSN 00298018. Available from DOI: 10.1016/j.oceaneng.2017.09.056.
- SUQUET, P.; MOULINEC, H.; CASTELNAU, O.; MONTAGNAT, M.; LAHELLEC, N.; GRENNERAT, F.; DUVAL, P.; BRENNER, R., 2012. Multi-scale modeling of the mechanical behavior of polycrystalline ice under transient creep. *Procedia IUTAM*. Vol. 3, pp. 76–90. ISSN 22109838. Available from DOI: 10.1016/j.piutam.2012.03.006.
- TABIEI, Ala; ZHANG, Wenlong, 2016. Evaluation of Various Numerical Methods in LS-Dyna for 3D Crack Propagation. *14th International LS-Dyna Users Conference* [online] [visited on 2019-05-28].

- TAKEUCHI, Takahiro; NAKAZAWA, Naoki; KAWAMURA, Muneo; SAKAI, Masafumi; AKAGAWA, Satoshi; SAEKI, Hiroshi, 2001. Examination of fractors affecting total ice load using medium-scale field indentation test data. *International Journal of Offshore and Polar Engineering*. Vol. 11, no. 3. ISSN 1053-5381.
- TEKSCAN, INC., 2016. *I-Scan® equilibration & calibration practical suggestions*.
- TEKSCAN, INC., 2017. *I-Scan® high-speed I-Scan user manual: Tactile Force & Pressure Measurement System version 7.6x*.
- TIMCO, G. W., 2011. Isolated ice floe impacts. *Cold Regions Science and Technology*. Vol. 68, no. 1-2, pp. 35–48. ISSN 0165232X. Available from DOI: 10.1016/j.coldregions.2011.04.008.
- TIMCO, G. W.; BRIEN, S. O., 1994. Flexural strength equation for sea ice. *Cold Regions Science and Technology*. Vol. 22, no. 3, pp. 285–298. ISSN 0165232X. Available from DOI: 10.1016/0165-232X(94)90006-X.
- TIMCO, G. W.; SUDOM, D., 2013. Revisiting the Sanderson pressure–area curve: Defining parameters that influence ice pressure. *Cold Regions Science and Technology*. Vol. 95, pp. 53–66. ISSN 0165232X. Available from DOI: 10.1016/j.coldregions.2013.08.005.
- TIMCO, G. W.; WEEKS, W. F., 2010. A review of the engineering properties of sea ice. *Cold Regions Science and Technology*. Vol. 60, no. 2, pp. 107–129. ISSN 0165232X. Available from DOI: 10.1016/j.coldregions.2009.10.003.
- TUHKURI, Jukka, 1993. *Laboratory test of ship structures under ice loading: Volumes 1*. Espoo.
- TUHKURI, Jukka, 1995. Experimental observations of the brittle failure process of ice and ice-structure contact. *Cold Regions Science and Technology*. Vol. 23, no. 3, pp. 265–278. ISSN 0165232X. Available from DOI: 10.1016/0165-232X(94)00018-S.
- WANG, Feng; ZHOU, Li; ZOU, Zao-jian; WANG, Yang; LIU, Yi, 2019. Study of continuous icebreaking process with cohesive element method. *Brodogradnja*. Vol. 70, no. 3, pp. 93–114. Available from DOI: 10.21278/brod70306.
- WELLS, J.; JORDAAN, I.; DERRADJI-AOUAT, A.; TAYLOR, R., 2011. Small-scale laboratory experiments on the indentation failure of polycrystalline ice in compression: Main results and pressure distribution. *Cold Regions Science and Technology*. Vol. 65, no. 3, pp. 314–325. ISSN 0165232X. Available from DOI: 10.1016/j.coldregions.2010.11.002.
- WORLD METEOROLOGICAL ORGANIZATION, 2015. *Sea Ice Nomenclature*. WMO publication, no. 259.
- WU, Youcai; WU, C. T.; HU, Wei, 2018. Parametric and Convergence Studies of the Smoothed Particle Galerkin (SPG) Method in Semi-brittle and Ductile Material Failure Analyses. *International LS-Dyna User Conference* [online] [visited on 2020-03-09].
- XIAO, Jing, 1997. *Damage and Fracture of Brittle Viscoelastic Solids with Application to Ice Load Models*. St. John's. Doctoral thesis. Memorial University of Newfoundland.

- YU, Zhaolong; LU, Wenjun; VAN DEN BERG, Marnix; AMDAHL, Jørgen; LØSET, Sveinung, 2021. Glacial ice impacts: Part II: Damage assessment and ice-structure interactions in accidental limit states (ALS). *Marine Structures*. Vol. 75, p. 102889. ISSN 09518339. Available from DOI: 10.1016/j.marstruc.2020.102889.
- ZIELESNY, Achim, 2016. *From Curve Fitting to Machine Learning: An Illustrative Guide to Scientific Data Analysis and Computational Intelligence*. Vol. 109. 2nd ed. 2016. Cham and s.l.: Springer International Publishing. Intelligent Systems Reference Library. ISBN 9783319325453. Available from DOI: 10.1007/978-3-319-32545-3.
- ZIEMER, Gesa, 2019. Utilization of TekScan sensors to investigate local ice pressure in scale model tests. In: *Proceedings of the 6th International Conference on Advanced Model Measurement Technology for The Maritime Industry*. Rome, Italy.

A. Tensile Test Results for Panel1 and Panel2

The quasi static tensile tests of the panel materials are conducted in accordance to DIN EN ISO 6892-1 (International Organization for Standardization, 2016) under ambient conditions, to characterise the steel material behaviour for the deformable MCNS simulations in section 4.5. In total 15 tests of the 10 mm plate material were available. No significant difference was found between tests lengthwise or crosswise to the rolling direction (Tests: 11-18, 21-28). In the case of the 12 mm flat bar material used as frames, four specimens were tested in lengthwise direction. The specimen geometries are given in Figure A.1.

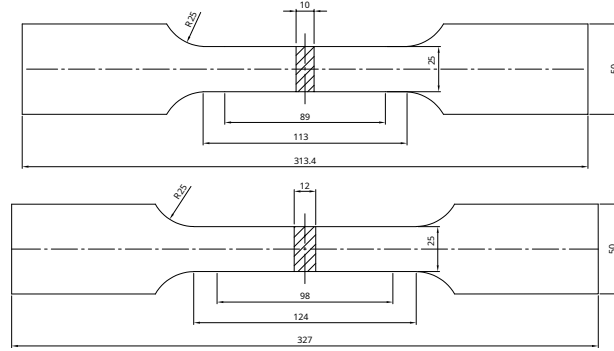


Figure A.1.: Tensile test geometries of the 10 mm plate material (top) and the 12 mm flat bar material (bottom)

For determining the true stress σ - true plastic strain ϵ_p curves, which are the necessary input for the used material model `*MAT_MODIFIED_PIECEWISE_LINEAR_PLASTICITY`, the tensile test data (engineering strain e , engineering stress $R = F/S_0$) is converted until the tensile strength by the following equations:

$$\epsilon_p = \ln(1 + e) - \epsilon_{eL} \approx \ln(1 + e) - \frac{R_{eL}}{E} \quad (\text{A.1})$$

$$\sigma = \frac{F}{S_0} (1 + e) \quad (\text{A.2})$$

The equations are further explained e.g. by Kubiczek; Burchard, et al. (2017). Based on the obtained true stress - true plastic strain curves, the material curves for the LS-Dyna simulations are determined manually. Special attention was paid to a smooth

first and second derivative, which is advantageous for the explicit time integration. The finally used material curves (in red) are presented together with the experimental true stress - true plastic strain curves in Figure A.2 and Figure A.3.

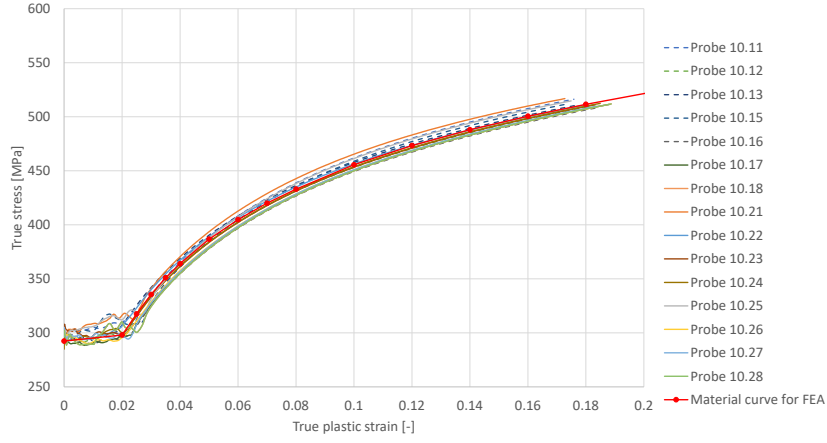


Figure A.2.: True stress - true plastic strain curves of the 10 mm plate material

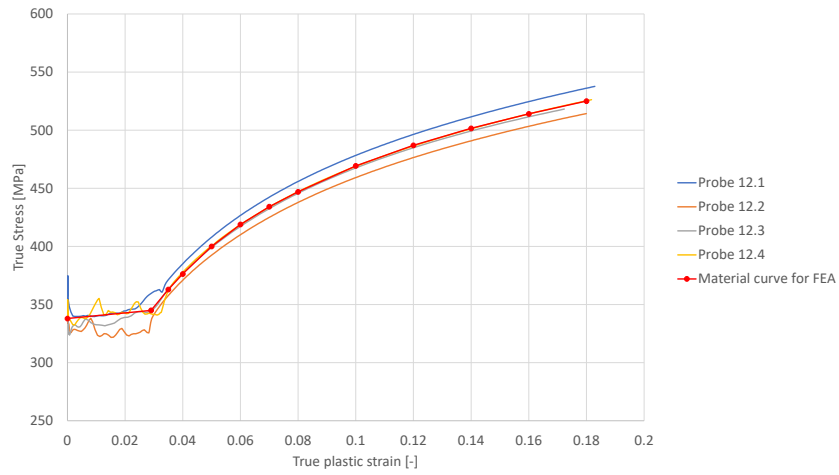


Figure A.3.: True stress - true plastic strain curves of the 12 mm flat bar material

B. LS-Dyna Keyword Decks of Used Material Models

The material models are given in SI units.

MCNS Ice Material Model

```
*MAT_MOHR_COULOMB_TITLE
MCNS Ice
$#      mid      ro      gmod      rnu      phi      cval      psi
      1      900.03.500000E9      0.33      0      0.526      1500000      0.0
$#      nplanes      lccpdr      lccpt      lccjdr      lccjt      lcsfac
      0      0      0      0      0      0      0
$#      gmoddp      gmodgr      lcgmp      lcphiep      lcpsiep      lcgms      cvalgr      aniso
      0.0      0.0      0.0      0.0      0.0      0.0      0.0      1.0
*MAT_ADD_EROSION
$#      mid      excl      mxpres      mneps      effeps      voleps      numfip      ncs
      1      0.0      1.1E8      0.0      -1.0      0.0      1.0      1.0
$#      mnpres      sigp1      sigvm      mxeps      epssh      sigth      impulse      failtm
      0.0      0.0      0.0      0.0      0.0      0.0      0.0      0.0
$#      idam      dmgtyp      lcsdg      ecrit      dmgepx      dcrit      fadexp      lcregd
      0      0.0      0      0.0      1.0      0.0      1.0      0
$#      lcflid      epsthin      engcrt      radcrt
      0      13092      0.0      0.0      0.0

*SECTION_SOLID_TITLE
Section Solid MCNS
$#      secid      elform      aet
      9      -1      0

$Exemplary CONSTRAINED_TIED_NODES_FAILURE definition
*CONSTRAINED_TIED_NODES_FAILURE
$#      nsid      eppf      etype
      1      0.002      1

*CONTACT_AUTOMATIC_SINGLE_SURFACE_ID
$#      cid      title
      0IceIce
$#      ssid      msid      sstyp      mstyp      sboxid      mboxid      spr      mpr
      1      0      3      0      0      0      0      0
$#      fs      fd      dc      vc      vdc      penchk      bt      dt
      0.05      0.0      0.0      0.0      20.0      0      0.01.00000E20
$#      sfs      sfm      sst      mst      sfst      sfmt      fsf      vsf
      0.2      1.0      0.0      0.0      1.0      1.0      1.0      1.0
$#      soft      sofsc1      lcidab      maxpar      sbopt      depth      bsort      frcfrq
      2      0.02      0      0.0      5.0      5      0      0
$#      penmax      thkopt      shlthk      snlog      isym      i2d3d      sldthk      sldstf
      0.0      0      0      0      0      0      0.0      0.0
$#      igap      ignore      dprfac      dtstif      edgek      unused      flangl      cid_rcf
      1      0      0.01.00000E-6      0.0      0.0      0.0      0
```

Simplified Steel Material Model

*MAT_PLASTIC_KINEMATIC_TITLE

Mat3 Steel

| \$# | mid | ro | e | pr | sigy | etan | beta |
|-----|-----|---------|----------|------|----------|------|------|
| | 2 | 7850.02 | 10000E11 | 0.33 | 550000E8 | 0.0 | 0.0 |
| \$# | src | srp | fs | vp | | | |
| | 0.0 | 0.0 | 0.0 | 0.0 | | | |

Steel Material Model - 10 mm Plate of Panel 1 and Panel 2

*MAT_MODIFIED_PIECEWISE_LINEAR_PLASTICITY_TITLE

MAT24 S255JR 10 mm Plate

| \$# | mid | ro | e | pr | sigy | etan | fail | tdel |
|-----|------|---------|----------|------|------|---------|--------|--------|
| | 10 | 7850.02 | 10000E11 | 0.3 | 0.0 | 0.0 | 0.356 | 0.0 |
| \$# | c | p | lcss | lcsr | vp | epsthin | epsmaj | numint |
| | 0.0 | 0.0 | 10 | 0 | 0.0 | 0.0 | 0.0 | 0.0 |
| \$# | eps1 | eps2 | eps3 | eps4 | eps5 | eps6 | eps7 | eps8 |
| | 0.0 | 0.0 | 0.0 | 0.0 | 0.0 | 0.0 | 0.0 | 0.0 |
| \$# | es1 | es2 | es3 | es4 | es5 | es6 | es7 | es8 |
| | 0.0 | 0.0 | 0.0 | 0.0 | 0.0 | 0.0 | 0.0 | 0.0 |

*DEFINE_CURVE_TITLE

material

\$Materialkurve S255JR 10mm

| \$ | LCID | SIDR | SFA | SFO | OFFA | OFFO | DATTYP | |
|-----|------|-------|------------------|-----|------|------|--------|-------|
| \$# | lcid | sidr | sfa | sfo | offa | offo | dattyp | lcint |
| | 10 | 0 | 1.0 | 1.0 | 0.0 | 0.0 | 0 | 0 |
| \$# | | a1 | | o1 | | | | |
| | | 0.0 | 2.9239798400e+08 | | | | | |
| | | 0.02 | 2.9800000000e+08 | | | | | |
| | | 0.025 | 3.1750000000e+08 | | | | | |
| | | 0.03 | 3.3550000000e+08 | | | | | |
| | | 0.035 | 3.5100000000e+08 | | | | | |
| | | 0.04 | 3.6400000000e+08 | | | | | |
| | | 0.05 | 3.8670000000e+08 | | | | | |
| | | 0.06 | 4.0480000000e+08 | | | | | |
| | | 0.07 | 4.2000000000e+08 | | | | | |
| | | 0.08 | 4.3300000000e+08 | | | | | |
| | | 0.1 | 4.5560000000e+08 | | | | | |
| | | 0.12 | 4.7335001600e+08 | | | | | |
| | | 0.14 | 4.8800000000e+08 | | | | | |
| | | 0.16 | 5.0050000000e+08 | | | | | |
| | | 0.18 | 5.1150000000e+08 | | | | | |
| | | 1.0 | 9.2000000000e+08 | | | | | |

Steel Material Model - 12 mm Flat Bar Stiffeners of Panel 1 and Panel 2

*MAT_MODIFIED_PIECEWISE_LINEAR_PLASTICITY_TITLE

MAT24 S255JR 12 mm Frames

| \$# | mid | ro | e | pr | sigy | etan | fail | tdel |
|-----|------|---------|----------|------|------|---------|--------|--------|
| | 12 | 7850.02 | 10000E11 | 0.3 | 0.0 | 0.0 | 0.356 | 0.0 |
| \$# | c | p | lcss | lcsr | vp | epsthin | epsmaj | numint |
| | 0.0 | 0.0 | 12 | 0 | 0.0 | 0.0 | 0.0 | 0.0 |
| \$# | eps1 | eps2 | eps3 | eps4 | eps5 | eps6 | eps7 | eps8 |
| | 0.0 | 0.0 | 0.0 | 0.0 | 0.0 | 0.0 | 0.0 | 0.0 |
| \$# | es1 | es2 | es3 | es4 | es5 | es6 | es7 | es8 |
| | 0.0 | 0.0 | 0.0 | 0.0 | 0.0 | 0.0 | 0.0 | 0.0 |

```

*DEFINE_CURVE_TITLE
material
$Materialkurve S255JR 12mm
$  LCID  SIDR  SFA  SFO  OFFA  OFFO  DATTYP
$#  lcid  sidr  sfa  sfo  offa  offo  dattyp  lcint
    12    0    1.0  1.0    0.0    0.0    0    0
$#      a1      o1
    0.0  3.3800000000e+08
  0.029  3.4500000000e+08
  0.035  3.6300000000e+08
  0.04   3.7630000000e+08
  0.05   4.0000000000e+08
  0.06   4.1890000000e+08
  0.07   4.3420000000e+08
  0.08   4.4700000000e+08
  0.1    4.6930000000e+08
  0.12   4.8700000000e+08
  0.14   5.0160000000e+08
  0.16   5.1404000000e+08
  0.18   5.2500000000e+08
  1.0    9.3000000000e+08

```

C. Ice Extrusion Test Results - Quasi Rigid Structures

In the following table all considered ice extrusion tests against quasi rigid structures are listed. The test parameters are explained in Figure 3.1.

The maximum force F_{max} and the maximum nominal pressure $p_{nom\ max}$ for each test are given. The maximum nominal pressure is calculated according to the following formula:

$$p_{nom\ max} = \frac{F_{max}}{\frac{1}{4} \cdot D^2 \cdot \pi} \quad (C.1)$$

| ID | Test run | Diameter | Gap height | Cone Angle | Velocity | G/D | F_max | p_nom_max |
|----|----------------------------|----------|------------|------------|----------|--------|--------|-----------|
| | | mm | mm | ° | mm/s | - | kN | MPa |
| 1 | Cone100_G0_A20_V01_3_PVC | 100 | 0 | 20 | 0.1 | 0 | 817.77 | 104.12 |
| 2 | Cone100_G0_A20_V01_4 | 100 | 0 | 20 | 0.1 | 0 | 786.31 | 100.12 |
| 3 | Cone100_G0_A20_V1 | 100 | 0 | 20 | 1 | 0 | 684.77 | 87.19 |
| 4 | Cone100_G0_A20_V4 | 100 | 0 | 20 | 4 | 0 | 617.25 | 78.59 |
| 5 | Cone100_G0_A20_V10 | 100 | 0 | 20 | 10 | 0 | 706.27 | 89.93 |
| 6 | Cone100_G6_25_A20_V001 | 100 | 6.25 | 20 | 0.01 | 0.0625 | 130.64 | 16.63 |
| 7 | Cone100_G6_25_A20_V01_1 | 100 | 6.25 | 20 | 0.1 | 0.0625 | 165.37 | 21.06 |
| 8 | Cone100_G6_25_A20_V01_2 | 100 | 6.25 | 20 | 0.1 | 0.0625 | 193.86 | 24.68 |
| 9 | Cone100_G6_25_A20_V01_3 | 100 | 6.25 | 20 | 0.1 | 0.0625 | 191.02 | 24.32 |
| 10 | Cone100_G6_25_A20_V01_4 | 100 | 6.25 | 20 | 0.1 | 0.0625 | 189.05 | 24.07 |
| 11 | Cone100_G6_25_A20_V1_1 | 100 | 6.25 | 20 | 1 | 0.0625 | 175.27 | 22.32 |
| 12 | Cone100_G6_25_A20_V1_2 | 100 | 6.25 | 20 | 1 | 0.0625 | 184.35 | 23.47 |
| 13 | Cone100_G6_25_A20_V1_3 | 100 | 6.25 | 20 | 1 | 0.0625 | 196.26 | 24.99 |
| 14 | Cone100_G6_25_A20_V1_4 | 100 | 6.25 | 20 | 1 | 0.0625 | 248.70 | 31.67 |
| 15 | Cone100_G6_25_A20_V1_5 | 100 | 6.25 | 20 | 1 | 0.0625 | 232.18 | 29.56 |
| 16 | Cone100_G6_25_A20_V1_6 | 100 | 6.25 | 20 | 1 | 0.0625 | 243.24 | 30.97 |
| 17 | Cone100_G6_25_A20_V1_7_PVC | 100 | 6.25 | 20 | 1 | 0.0625 | 237.50 | 30.24 |
| 18 | Cone100_G6_25_A20_V2_1 | 100 | 6.25 | 20 | 2 | 0.0625 | 186.82 | 23.79 |
| 19 | Cone100_G6_25_A20_V2_2 | 100 | 6.25 | 20 | 2 | 0.0625 | 186.25 | 23.71 |
| 20 | Cone100_G6_25_A20_V2_3 | 100 | 6.25 | 20 | 2 | 0.0625 | 184.22 | 23.46 |
| 21 | Cone100_G6_25_A20_V4_1 | 100 | 6.25 | 20 | 4 | 0.0625 | 116.89 | 14.88 |
| 22 | Cone100_G6_25_A20_V4_2 | 100 | 6.25 | 20 | 4 | 0.0625 | 120.75 | 15.37 |
| 23 | Cone100_G6_25_A20_V4_3 | 100 | 6.25 | 20 | 4 | 0.0625 | 115.41 | 14.69 |
| 24 | Cone100_G6_25_A20_V7_1 | 100 | 6.25 | 20 | 7 | 0.0625 | 100.45 | 12.79 |
| 25 | Cone100_G6_25_A20_V7_2 | 100 | 6.25 | 20 | 7 | 0.0625 | 100.96 | 12.85 |
| 26 | Cone100_G6_25_A20_V7_3 | 100 | 6.25 | 20 | 7 | 0.0625 | 108.44 | 13.81 |
| 27 | Cone100_G6_25_A20_V10_1 | 100 | 6.25 | 20 | 10 | 0.0625 | 87.19 | 11.10 |
| 28 | Cone100_G6_25_A20_V10_2 | 100 | 6.25 | 20 | 10 | 0.0625 | 88.66 | 11.29 |
| 29 | Cone100_G6_25_A20_V10_3 | 100 | 6.25 | 20 | 10 | 0.0625 | 85.92 | 10.94 |
| 30 | Cone100_G12_5_A20_V001 | 100 | 12.5 | 20 | 0.01 | 0.125 | 84.26 | 10.73 |
| 31 | Cone100_G12_5_A20_V01_1 | 100 | 12.5 | 20 | 0.1 | 0.125 | 123.56 | 15.73 |
| 32 | Cone100_G12_5_A20_V01_2 | 100 | 12.5 | 20 | 0.1 | 0.125 | 166.06 | 21.14 |
| 33 | Cone100_G12_5_A20_V01_3 | 100 | 12.5 | 20 | 0.1 | 0.125 | 121.61 | 15.48 |
| 34 | Cone100_G12_5_A20_V01_4 | 100 | 12.5 | 20 | 0.1 | 0.125 | 123.87 | 15.77 |
| 35 | Cone100_G12_5_A20_V1_1 | 100 | 12.5 | 20 | 1 | 0.125 | 155.50 | 19.80 |
| 36 | Cone100_G12_5_A20_V1_2 | 100 | 12.5 | 20 | 1 | 0.125 | 155.50 | 19.80 |
| 37 | Cone100_G12_5_A20_V1_3 | 100 | 12.5 | 20 | 1 | 0.125 | 155.94 | 19.86 |
| 38 | Cone100_G12_5_A20_V1_4 | 100 | 12.5 | 20 | 1 | 0.125 | 148.87 | 18.95 |
| 39 | Cone100_G12_5_A20_V2_1 | 100 | 12.5 | 20 | 2 | 0.125 | 84.35 | 10.74 |
| 40 | Cone100_G12_5_A20_V2_2 | 100 | 12.5 | 20 | 2 | 0.125 | 87.13 | 11.09 |
| 41 | Cone100_G12_5_A20_V2_3 | 100 | 12.5 | 20 | 2 | 0.125 | 85.25 | 10.85 |
| 42 | Cone100_G12_5_A20_V4_1 | 100 | 12.5 | 20 | 4 | 0.125 | 37.11 | 4.72 |
| 43 | Cone100_G12_5_A20_V4_2 | 100 | 12.5 | 20 | 4 | 0.125 | 47.36 | 6.03 |
| 44 | Cone100_G12_5_A20_V4_3 | 100 | 12.5 | 20 | 4 | 0.125 | 44.19 | 5.63 |
| 45 | Cone100_G12_5_A20_V7_1 | 100 | 12.5 | 20 | 7 | 0.125 | 34.14 | 4.35 |
| 46 | Cone100_G12_5_A20_V7_2 | 100 | 12.5 | 20 | 7 | 0.125 | 28.67 | 3.65 |
| 47 | Cone100_G12_5_A20_V7_3 | 100 | 12.5 | 20 | 7 | 0.125 | 34.18 | 4.35 |
| 48 | Cone100_G12_5_A20_V10_1 | 100 | 12.5 | 20 | 10 | 0.125 | 23.84 | 3.04 |
| 49 | Cone100_G12_5_A20_V10_2 | 100 | 12.5 | 20 | 10 | 0.125 | 26.62 | 3.39 |
| 50 | Cone100_G12_5_A20_V10_3 | 100 | 12.5 | 20 | 10 | 0.125 | 25.00 | 3.18 |
| 51 | Cone100_G12_5_A20_V10_4 | 100 | 12.5 | 20 | 10 | 0.125 | 32.72 | 4.17 |
| 52 | Cone100_G25_A20_V001 | 100 | 25 | 20 | 0.01 | 0.25 | 49.60 | 6.32 |
| 53 | Cone100_G25_A20_V01_1 | 100 | 25 | 20 | 0.1 | 0.25 | 55.35 | 7.05 |

| ID | Test run | Diameter | Gap height | Cone Angle | Velocity | G/D | F_max | p_nom_max |
|-----|------------------------|----------|------------|------------|----------|------|-------|-----------|
| | | mm | mm | ° | mm/s | - | kN | MPa |
| 54 | Cone100_G25_A20_V01_2 | 100 | 25 | 20 | 0.1 | 0.25 | 63.15 | 8.04 |
| 55 | Cone100_G25_A20_V01_3 | 100 | 25 | 20 | 0.1 | 0.25 | 64.27 | 8.18 |
| 56 | Cone100_G25_A20_V1_1 | 100 | 25 | 20 | 1 | 0.25 | 73.73 | 9.39 |
| 57 | Cone100_G25_A20_V1_2 | 100 | 25 | 20 | 1 | 0.25 | 69.07 | 8.79 |
| 58 | Cone100_G25_A20_V1_3 | 100 | 25 | 20 | 1 | 0.25 | 59.61 | 7.59 |
| 59 | Cone100_G25_A20_V2_1 | 100 | 25 | 20 | 2 | 0.25 | 17.96 | 2.29 |
| 60 | Cone100_G25_A20_V2_2 | 100 | 25 | 20 | 2 | 0.25 | 15.96 | 2.03 |
| 61 | Cone100_G25_A20_V2_3 | 100 | 25 | 20 | 2 | 0.25 | 18.19 | 2.32 |
| 62 | Cone100_G25_A20_V4_1 | 100 | 25 | 20 | 4 | 0.25 | 13.78 | 1.75 |
| 63 | Cone100_G25_A20_V4_2 | 100 | 25 | 20 | 4 | 0.25 | 16.32 | 2.08 |
| 64 | Cone100_G25_A20_V4_3 | 100 | 25 | 20 | 4 | 0.25 | 14.12 | 1.80 |
| 65 | Cone100_G25_A20_V7_1 | 100 | 25 | 20 | 7 | 0.25 | 14.55 | 1.85 |
| 66 | Cone100_G25_A20_V7_2 | 100 | 25 | 20 | 7 | 0.25 | 14.86 | 1.89 |
| 67 | Cone100_G25_A20_V7_3 | 100 | 25 | 20 | 7 | 0.25 | 11.05 | 1.41 |
| 68 | Cone100_G25_A20_V10_1 | 100 | 25 | 20 | 10 | 0.25 | 12.20 | 1.55 |
| 69 | Cone100_G25_A20_V10_2 | 100 | 25 | 20 | 10 | 0.25 | 11.89 | 1.51 |
| 70 | Cone100_G25_A20_V10_3 | 100 | 25 | 20 | 10 | 0.25 | 14.42 | 1.84 |
| 71 | Cone100_G50_A20_V001 | 100 | 50 | 20 | 0.01 | 0.5 | 25.78 | 3.28 |
| 72 | Cone100_G50_A20_V01_1 | 100 | 50 | 20 | 0.1 | 0.5 | 21.56 | 2.75 |
| 73 | Cone100_G50_A20_V01_2 | 100 | 50 | 20 | 0.1 | 0.5 | 30.72 | 3.91 |
| 74 | Cone100_G50_A20_V01_3 | 100 | 50 | 20 | 0.1 | 0.5 | 26.40 | 3.36 |
| 75 | Cone100_G50_A20_V01_4 | 100 | 50 | 20 | 0.1 | 0.5 | 24.37 | 3.10 |
| 76 | Cone100_G50_A20_V01_5 | 100 | 50 | 20 | 0.1 | 0.5 | 20.18 | 2.57 |
| 77 | Cone100_G50_A20_V1_1 | 100 | 50 | 20 | 1 | 0.5 | 14.11 | 1.80 |
| 78 | Cone100_G50_A20_V1_2 | 100 | 50 | 20 | 1 | 0.5 | 10.63 | 1.35 |
| 79 | Cone100_G50_A20_V1_3 | 100 | 50 | 20 | 1 | 0.5 | 11.72 | 1.49 |
| 80 | Cone100_G50_A20_V2_1 | 100 | 50 | 20 | 2 | 0.5 | 11.81 | 1.50 |
| 81 | Cone100_G50_A20_V2_2 | 100 | 50 | 20 | 2 | 0.5 | 10.63 | 1.35 |
| 82 | Cone100_G50_A20_V2_3 | 100 | 50 | 20 | 2 | 0.5 | 11.25 | 1.43 |
| 83 | Cone100_G50_A20_V4_1 | 100 | 50 | 20 | 4 | 0.5 | 10.13 | 1.29 |
| 84 | Cone100_G50_A20_V4_2 | 100 | 50 | 20 | 4 | 0.5 | 11.73 | 1.49 |
| 85 | Cone100_G50_A20_V4_3 | 100 | 50 | 20 | 4 | 0.5 | 9.16 | 1.17 |
| 86 | Cone100_G50_A20_V7_1 | 100 | 50 | 20 | 7 | 0.5 | 9.69 | 1.23 |
| 87 | Cone100_G50_A20_V7_2 | 100 | 50 | 20 | 7 | 0.5 | 9.81 | 1.25 |
| 88 | Cone100_G50_A20_V7_3 | 100 | 50 | 20 | 7 | 0.5 | 10.61 | 1.35 |
| 89 | Cone100_G50_A20_V10_1 | 100 | 50 | 20 | 10 | 0.5 | 10.12 | 1.29 |
| 90 | Cone100_G50_A20_V10_2 | 100 | 50 | 20 | 10 | 0.5 | 9.99 | 1.27 |
| 91 | Cone100_G50_A20_V10_3 | 100 | 50 | 20 | 10 | 0.5 | 10.04 | 1.28 |
| 92 | Cone100_G100_A00_V01_1 | 100 | 100 | 0 | 0.1 | 1 | 40.16 | 5.11 |
| 93 | Cone100_G100_A00_V01_2 | 100 | 100 | 0 | 0.1 | 1 | 38.93 | 4.96 |
| 94 | Cone100_G100_A00_V01_3 | 100 | 100 | 0 | 0.1 | 1 | 39.04 | 4.97 |
| 95 | Cone100_G100_A00_V1_1 | 100 | 100 | 0 | 1 | 1 | 24.38 | 3.10 |
| 96 | Cone100_G100_A00_V1_2 | 100 | 100 | 0 | 1 | 1 | 30.39 | 3.87 |
| 97 | Cone100_G100_A00_V1_3 | 100 | 100 | 0 | 1 | 1 | 26.91 | 3.43 |
| 98 | Cone100_G100_A00_V2_1 | 100 | 100 | 0 | 2 | 1 | 31.22 | 3.97 |
| 99 | Cone100_G100_A00_V2_2 | 100 | 100 | 0 | 2 | 1 | 40.43 | 5.15 |
| 100 | Cone100_G100_A00_V2_3 | 100 | 100 | 0 | 2 | 1 | 23.07 | 2.94 |
| 101 | Cone100_G100_A00_V4_1 | 100 | 100 | 0 | 4 | 1 | 39.49 | 5.03 |
| 102 | Cone100_G100_A00_V4_2 | 100 | 100 | 0 | 4 | 1 | 36.82 | 4.69 |
| 103 | Cone100_G100_A00_V4_3 | 100 | 100 | 0 | 4 | 1 | 29.19 | 3.72 |
| 104 | Cone100_G100_A00_V7_1 | 100 | 100 | 0 | 7 | 1 | 21.60 | 2.75 |
| 105 | Cone100_G100_A00_V7_2 | 100 | 100 | 0 | 7 | 1 | 25.61 | 3.26 |
| 106 | Cone100_G100_A00_V7_3 | 100 | 100 | 0 | 7 | 1 | 17.76 | 2.26 |

| ID | Test run | Diameter | Gap height | Cone Angle | Velocity | G/D | F_max | p_nom_max |
|-----|-------------------------|----------|------------|------------|----------|--------|--------|-----------|
| | | mm | mm | ° | mm/s | - | kN | MPa |
| 107 | Cone100_G100_A00_V10_1 | 100 | 100 | 0 | 10 | 1 | 23.88 | 3.04 |
| 108 | Cone100_G100_A00_V10_2 | 100 | 100 | 0 | 10 | 1 | 23.22 | 2.96 |
| 109 | Cone100_G100_A00_V10_3 | 100 | 100 | 0 | 10 | 1 | 20.77 | 2.65 |
| 110 | Cone100_G100_A20_V001 | 100 | 100 | 20 | 0.01 | 1 | 15.90 | 2.02 |
| 111 | Cone100_G100_A20_V01_1 | 100 | 100 | 20 | 0.1 | 1 | 10.79 | 1.37 |
| 112 | Cone100_G100_A20_V01_2 | 100 | 100 | 20 | 0.1 | 1 | 9.35 | 1.19 |
| 113 | Cone100_G100_A20_V01_3 | 100 | 100 | 20 | 0.1 | 1 | 10.47 | 1.33 |
| 114 | Cone100_G100_A20_V1_1 | 100 | 100 | 20 | 1 | 1 | 6.67 | 0.85 |
| 115 | Cone100_G100_A20_V1_2 | 100 | 100 | 20 | 1 | 1 | 7.54 | 0.96 |
| 116 | Cone100_G100_A20_V1_3 | 100 | 100 | 20 | 1 | 1 | 8.73 | 1.11 |
| 117 | Cone100_G100_A20_V4_2 | 100 | 100 | 20 | 4 | 1 | 8.59 | 1.09 |
| 118 | Cone100_G100_A20_V4_3 | 100 | 100 | 20 | 4 | 1 | 7.48 | 0.95 |
| 119 | Cone100_G100_A20_V10_1 | 100 | 100 | 20 | 10 | 1 | 6.52 | 0.83 |
| 120 | Cone100_G100_A20_V10_2 | 100 | 100 | 20 | 10 | 1 | 8.22 | 1.05 |
| 121 | Cone100_G100_A20_V10_3 | 100 | 100 | 20 | 10 | 1 | 6.13 | 0.78 |
| 122 | Cone200_G12_5_A20_V001 | 200 | 12.5 | 20 | 0.01 | 0.0625 | 466.35 | 14.84 |
| 123 | Cone200_G12_5_A20_V01 | 200 | 12.5 | 20 | 0.1 | 0.0625 | 706.01 | 22.47 |
| 124 | Cone200_G12_5_A20_V01_1 | 200 | 12.5 | 20 | 0.1 | 0.0625 | 628.00 | 19.99 |
| 125 | Cone200_G12_5_A20_V1_1 | 200 | 12.5 | 20 | 1 | 0.0625 | 870.70 | 27.72 |
| 126 | Cone200_G12_5_A20_V1_2 | 200 | 12.5 | 20 | 1 | 0.0625 | 910.50 | 28.98 |
| 127 | Cone200_G12_5_A20_V1_3 | 200 | 12.5 | 20 | 1 | 0.0625 | 879.73 | 28.00 |
| 128 | Cone200_G12_5_A20_V2_1 | 200 | 12.5 | 20 | 2 | 0.0625 | 797.65 | 25.39 |
| 129 | Cone200_G12_5_A20_V4_1 | 200 | 12.5 | 20 | 4 | 0.0625 | 719.38 | 22.90 |
| 130 | Cone200_G12_5_A20_V7_1 | 200 | 12.5 | 20 | 7 | 0.0625 | 611.15 | 19.45 |
| 131 | Cone200_G12_5_A20_V10_1 | 200 | 12.5 | 20 | 10 | 0.0625 | 510.04 | 16.24 |
| 132 | Cone200_G12_5_A20_V10_2 | 200 | 12.5 | 20 | 10 | 0.0625 | 455.08 | 14.49 |
| 133 | Cone200_G12_5_A20_V10_3 | 200 | 12.5 | 20 | 10 | 0.0625 | 382.08 | 12.16 |
| 134 | Cone200_G12_5_A30_V01_1 | 200 | 12.5 | 30 | 0.1 | 0.0625 | 622.69 | 19.82 |
| 135 | Cone200_G12_5_A30_V1_1 | 200 | 12.5 | 30 | 1 | 0.0625 | 783.43 | 24.94 |
| 136 | Cone200_G12_5_A30_V1_2 | 200 | 12.5 | 30 | 1 | 0.0625 | 797.56 | 25.39 |
| 137 | Cone200_G12_5_A30_V1_3 | 200 | 12.5 | 30 | 1 | 0.0625 | 870.54 | 27.71 |
| 138 | Cone200_G12_5_A30_V2_1 | 200 | 12.5 | 30 | 2 | 0.0625 | 847.37 | 26.97 |
| 139 | Cone200_G12_5_A30_V4_1 | 200 | 12.5 | 30 | 4 | 0.0625 | 696.39 | 22.17 |
| 140 | Cone200_G12_5_A30_V7_1 | 200 | 12.5 | 30 | 7 | 0.0625 | 635.56 | 20.23 |
| 141 | Cone200_G12_5_A30_V10_1 | 200 | 12.5 | 30 | 10 | 0.0625 | 440.98 | 14.04 |
| 142 | Cone200_G12_5_A30_V10_2 | 200 | 12.5 | 30 | 10 | 0.0625 | 534.90 | 17.03 |
| 143 | Cone200_G12_5_A30_V10_3 | 200 | 12.5 | 30 | 10 | 0.0625 | 573.99 | 18.27 |
| 144 | Cone200_G25_A00_V01_1 | 200 | 25 | 0 | 0.1 | 0.125 | 482.89 | 15.37 |
| 145 | Cone200_G25_A00_V01_2 | 200 | 25 | 0 | 0.1 | 0.125 | 534.88 | 17.03 |
| 146 | Cone200_G25_A00_V01_3 | 200 | 25 | 0 | 0.1 | 0.125 | 505.65 | 16.10 |
| 147 | Cone200_G25_A00_V1_1 | 200 | 25 | 0 | 1 | 0.125 | 576.42 | 18.35 |
| 148 | Cone200_G25_A00_V1_2 | 200 | 25 | 0 | 1 | 0.125 | 587.74 | 18.71 |
| 149 | Cone200_G25_A00_V1_3 | 200 | 25 | 0 | 1 | 0.125 | 584.35 | 18.60 |
| 150 | Cone200_G25_A00_V2_1 | 200 | 25 | 0 | 2 | 0.125 | 329.15 | 10.48 |
| 151 | Cone200_G25_A00_V2_2 | 200 | 25 | 0 | 2 | 0.125 | 375.45 | 11.95 |
| 152 | Cone200_G25_A00_V2_3 | 200 | 25 | 0 | 2 | 0.125 | 373.76 | 11.90 |
| 153 | Cone200_G25_A00_V4_1 | 200 | 25 | 0 | 4 | 0.125 | 196.72 | 6.26 |
| 154 | Cone200_G25_A00_V4_2 | 200 | 25 | 0 | 4 | 0.125 | 217.54 | 6.92 |
| 155 | Cone200_G25_A00_V4_3 | 200 | 25 | 0 | 4 | 0.125 | 281.29 | 8.95 |
| 156 | Cone200_G25_A00_V7_1 | 200 | 25 | 0 | 7 | 0.125 | 177.19 | 5.64 |
| 157 | Cone200_G25_A00_V7_2 | 200 | 25 | 0 | 7 | 0.125 | 188.01 | 5.98 |
| 158 | Cone200_G25_A00_V7_3 | 200 | 25 | 0 | 7 | 0.125 | 182.25 | 5.80 |
| 159 | Cone200_G25_A00_V10_1 | 200 | 25 | 0 | 10 | 0.125 | 139.47 | 4.44 |

| ID | Test run | Diameter | Gap height | Cone Angle | Velocity | G/D | F_max | p_nom_max |
|-----|------------------------|----------|------------|------------|----------|-------|--------|-----------|
| | | mm | mm | ° | mm/s | - | kN | MPa |
| 160 | Cone200_G25_A00_V10_2 | 200 | 25 | 0 | 10 | 0.125 | 179.88 | 5.73 |
| 161 | Cone200_G25_A00_V10_3 | 200 | 25 | 0 | 10 | 0.125 | 156.81 | 4.99 |
| 162 | Cone200_G25_A10_V01_1 | 200 | 25 | 10 | 0.1 | 0.125 | 445.19 | 14.17 |
| 163 | Cone200_G25_A10_V01_2 | 200 | 25 | 10 | 0.1 | 0.125 | 442.53 | 14.09 |
| 164 | Cone200_G25_A10_V01_3 | 200 | 25 | 10 | 0.1 | 0.125 | 441.32 | 14.05 |
| 165 | Cone200_G25_A10_V1_1 | 200 | 25 | 10 | 1 | 0.125 | 587.88 | 18.71 |
| 166 | Cone200_G25_A10_V1_2 | 200 | 25 | 10 | 1 | 0.125 | 578.54 | 18.42 |
| 167 | Cone200_G25_A10_V1_3 | 200 | 25 | 10 | 1 | 0.125 | 563.07 | 17.92 |
| 168 | Cone200_G25_A10_V2_1 | 200 | 25 | 10 | 2 | 0.125 | 351.55 | 11.19 |
| 169 | Cone200_G25_A10_V2_2 | 200 | 25 | 10 | 2 | 0.125 | 347.87 | 11.07 |
| 170 | Cone200_G25_A10_V2_3 | 200 | 25 | 10 | 2 | 0.125 | 351.12 | 11.18 |
| 171 | Cone200_G25_A10_V4_1 | 200 | 25 | 10 | 4 | 0.125 | 187.01 | 5.95 |
| 172 | Cone200_G25_A10_V4_2 | 200 | 25 | 10 | 4 | 0.125 | 187.21 | 5.96 |
| 173 | Cone200_G25_A10_V4_3 | 200 | 25 | 10 | 4 | 0.125 | 220.06 | 7.00 |
| 174 | Cone200_G25_A10_V7_1 | 200 | 25 | 10 | 7 | 0.125 | 130.83 | 4.16 |
| 175 | Cone200_G25_A10_V7_2 | 200 | 25 | 10 | 7 | 0.125 | 188.07 | 5.99 |
| 176 | Cone200_G25_A10_V7_3 | 200 | 25 | 10 | 7 | 0.125 | 182.31 | 5.80 |
| 177 | Cone200_G25_A10_V10_1 | 200 | 25 | 10 | 10 | 0.125 | 160.66 | 5.11 |
| 178 | Cone200_G25_A10_V10_2 | 200 | 25 | 10 | 10 | 0.125 | 150.59 | 4.79 |
| 179 | Cone200_G25_A10_V10_3 | 200 | 25 | 10 | 10 | 0.125 | 147.46 | 4.69 |
| 180 | Cone200_G25_A20_V001_1 | 200 | 25 | 20 | 0.01 | 0.125 | 332.10 | 10.57 |
| 181 | Cone200_G25_A20_V01_1 | 200 | 25 | 20 | 0.1 | 0.125 | 461.34 | 14.69 |
| 182 | Cone200_G25_A20_V01_2 | 200 | 25 | 20 | 0.1 | 0.125 | 451.04 | 14.36 |
| 183 | Cone200_G25_A20_V01_3 | 200 | 25 | 20 | 0.1 | 0.125 | 445.56 | 14.18 |
| 184 | Cone200_G25_A20_V1_1 | 200 | 25 | 20 | 1 | 0.125 | 590.69 | 18.80 |
| 185 | Cone200_G25_A20_V1_2 | 200 | 25 | 20 | 1 | 0.125 | 562.83 | 17.92 |
| 186 | Cone200_G25_A20_V1_3 | 200 | 25 | 20 | 1 | 0.125 | 579.61 | 18.45 |
| 187 | Cone200_G25_A20_V2_1 | 200 | 25 | 20 | 2 | 0.125 | 328.36 | 10.45 |
| 188 | Cone200_G25_A20_V2_2 | 200 | 25 | 20 | 2 | 0.125 | 318.52 | 10.14 |
| 189 | Cone200_G25_A20_V2_3 | 200 | 25 | 20 | 2 | 0.125 | 272.95 | 8.69 |
| 190 | Cone200_G25_A20_V4_1 | 200 | 25 | 20 | 4 | 0.125 | 198.06 | 6.30 |
| 191 | Cone200_G25_A20_V4_2 | 200 | 25 | 20 | 4 | 0.125 | 199.53 | 6.35 |
| 192 | Cone200_G25_A20_V4_3 | 200 | 25 | 20 | 4 | 0.125 | 195.86 | 6.23 |
| 193 | Cone200_G25_A20_V7_1 | 200 | 25 | 20 | 7 | 0.125 | 158.97 | 5.06 |
| 194 | Cone200_G25_A20_V7_2 | 200 | 25 | 20 | 7 | 0.125 | 127.81 | 4.07 |
| 195 | Cone200_G25_A20_V7_3 | 200 | 25 | 20 | 7 | 0.125 | 173.49 | 5.52 |
| 196 | Cone200_G25_A20_V10_1 | 200 | 25 | 20 | 10 | 0.125 | 172.37 | 5.49 |
| 197 | Cone200_G25_A20_V10_2 | 200 | 25 | 20 | 10 | 0.125 | 200.01 | 6.37 |
| 198 | Cone200_G25_A20_V10_3 | 200 | 25 | 20 | 10 | 0.125 | 137.84 | 4.39 |
| 199 | Cone200_G25_A30_V01_1 | 200 | 25 | 30 | 0.1 | 0.125 | 403.39 | 12.84 |
| 200 | Cone200_G25_A30_V01_2 | 200 | 25 | 30 | 0.1 | 0.125 | 451.45 | 14.37 |
| 201 | Cone200_G25_A30_V01_3 | 200 | 25 | 30 | 0.1 | 0.125 | 452.08 | 14.39 |
| 202 | Cone200_G25_A30_V1_1 | 200 | 25 | 30 | 1 | 0.125 | 531.44 | 16.92 |
| 203 | Cone200_G25_A30_V1_2 | 200 | 25 | 30 | 1 | 0.125 | 578.22 | 18.41 |
| 204 | Cone200_G25_A30_V1_3 | 200 | 25 | 30 | 1 | 0.125 | 588.54 | 18.73 |
| 205 | Cone200_G25_A30_V2_1 | 200 | 25 | 30 | 2 | 0.125 | 313.82 | 9.99 |
| 206 | Cone200_G25_A30_V2_2 | 200 | 25 | 30 | 2 | 0.125 | 344.49 | 10.97 |
| 207 | Cone200_G25_A30_V2_3 | 200 | 25 | 30 | 2 | 0.125 | 351.63 | 11.19 |
| 208 | Cone200_G25_A30_V3_1 | 200 | 25 | 30 | 3 | 0.125 | 243.82 | 7.76 |
| 209 | Cone200_G25_A30_V4_1 | 200 | 25 | 30 | 4 | 0.125 | 200.71 | 6.39 |
| 210 | Cone200_G25_A30_V4_2 | 200 | 25 | 30 | 4 | 0.125 | 203.77 | 6.49 |
| 211 | Cone200_G25_A30_V4_3 | 200 | 25 | 30 | 4 | 0.125 | 228.39 | 7.27 |
| 212 | Cone200_G25_A30_V7_1 | 200 | 25 | 30 | 7 | 0.125 | 189.27 | 6.02 |

| ID | Test run | Diameter | Gap height | Cone Angle | Velocity | G/D | F_max | p_nom_max |
|-----|-------------------------|----------|------------|------------|----------|-------|--------|-----------|
| | | mm | mm | ° | mm/s | - | kN | MPa |
| 213 | Cone200_G25_A30_V7_2 | 200 | 25 | 30 | 7 | 0.125 | 206.01 | 6.56 |
| 214 | Cone200_G25_A30_V7_3 | 200 | 25 | 30 | 7 | 0.125 | 196.27 | 6.25 |
| 215 | Cone200_G25_A30_V10_1 | 200 | 25 | 30 | 10 | 0.125 | 131.74 | 4.19 |
| 216 | Cone200_G25_A30_V10_2 | 200 | 25 | 30 | 10 | 0.125 | 135.18 | 4.30 |
| 217 | Cone200_G25_A30_V10_3 | 200 | 25 | 30 | 10 | 0.125 | 139.65 | 4.45 |
| 218 | Cone200_G50_A00_V01_1 | 200 | 50 | 0 | 0.1 | 0.25 | 292.43 | 9.31 |
| 219 | Cone200_G50_A00_V01_2 | 200 | 50 | 0 | 0.1 | 0.25 | 295.23 | 9.40 |
| 220 | Cone200_G50_A00_V01_3 | 200 | 50 | 0 | 0.1 | 0.25 | 283.87 | 9.04 |
| 221 | Cone200_G50_A00_V1_1 | 200 | 50 | 0 | 1 | 0.25 | 263.48 | 8.39 |
| 222 | Cone200_G50_A00_V1_2 | 200 | 50 | 0 | 1 | 0.25 | 280.70 | 8.94 |
| 223 | Cone200_G50_A00_V1_3 | 200 | 50 | 0 | 1 | 0.25 | 182.38 | 5.81 |
| 224 | Cone200_G50_A00_V2_1 | 200 | 50 | 0 | 2 | 0.25 | 131.84 | 4.20 |
| 225 | Cone200_G50_A00_V10_1 | 200 | 50 | 0 | 10 | 0.25 | 97.15 | 3.09 |
| 226 | Cone200_G50_A00_V10_2 | 200 | 50 | 0 | 10 | 0.25 | 111.77 | 3.56 |
| 227 | Cone200_G50_A00_V10_3 | 200 | 50 | 0 | 10 | 0.25 | 103.50 | 3.29 |
| 228 | Cone200_G50_A10_V01_1 | 200 | 50 | 10 | 0.1 | 0.25 | 243.92 | 7.76 |
| 229 | Cone200_G50_A10_V01_2 | 200 | 50 | 10 | 0.1 | 0.25 | 254.65 | 8.11 |
| 230 | Cone200_G50_A10_V01_3 | 200 | 50 | 10 | 0.1 | 0.25 | 259.24 | 8.25 |
| 231 | Cone200_G50_A10_V1_1 | 200 | 50 | 10 | 1 | 0.25 | 300.20 | 9.56 |
| 232 | Cone200_G50_A10_V1_2 | 200 | 50 | 10 | 1 | 0.25 | 301.00 | 9.58 |
| 233 | Cone200_G50_A10_V1_3 | 200 | 50 | 10 | 1 | 0.25 | 260.86 | 8.30 |
| 234 | Cone200_G50_A10_V2_1 | 200 | 50 | 10 | 2 | 0.25 | 68.66 | 2.19 |
| 235 | Cone200_G50_A10_V2_2 | 200 | 50 | 10 | 2 | 0.25 | 58.10 | 1.85 |
| 236 | Cone200_G50_A10_V10_1 | 200 | 50 | 10 | 10 | 0.25 | 33.89 | 1.08 |
| 237 | Cone200_G50_A10_V10_2 | 200 | 50 | 10 | 10 | 0.25 | 52.24 | 1.66 |
| 238 | Cone200_G50_A10_V10_3 | 200 | 50 | 10 | 10 | 0.25 | 41.26 | 1.31 |
| 239 | Cone200_G50_A20_V01_1 | 200 | 50 | 20 | 0.1 | 0.25 | 240.59 | 7.66 |
| 240 | Cone200_G50_A20_V01_2 | 200 | 50 | 20 | 0.1 | 0.25 | 256.26 | 8.16 |
| 241 | Cone200_G50_A20_V01_3 | 200 | 50 | 20 | 0.1 | 0.25 | 255.53 | 8.13 |
| 242 | Cone200_G50_A20_V1_1 | 200 | 50 | 20 | 1 | 0.25 | 311.36 | 9.91 |
| 243 | Cone200_G50_A20_V1_2 | 200 | 50 | 20 | 1 | 0.25 | 290.85 | 9.26 |
| 244 | Cone200_G50_A20_V1_3 | 200 | 50 | 20 | 1 | 0.25 | 290.62 | 9.25 |
| 245 | Cone200_G50_A20_V1_4 | 200 | 50 | 20 | 1 | 0.25 | 322.41 | 10.26 |
| 246 | Cone200_G50_A20_V2_1 | 200 | 50 | 20 | 2 | 0.25 | 56.17 | 1.79 |
| 247 | Cone200_G50_A20_V2_2 | 200 | 50 | 20 | 2 | 0.25 | 56.25 | 1.79 |
| 248 | Cone200_G50_A20_V2_3 | 200 | 50 | 20 | 2 | 0.25 | 57.56 | 1.83 |
| 249 | Cone200_G50_A20_V4_1 | 200 | 50 | 20 | 4 | 0.25 | 56.52 | 1.80 |
| 250 | Cone200_G50_A20_V4_2 | 200 | 50 | 20 | 4 | 0.25 | 61.91 | 1.97 |
| 251 | Cone200_G50_A20_V4_3 | 200 | 50 | 20 | 4 | 0.25 | 36.59 | 1.16 |
| 252 | Cone200_G50_A20_V4_4 | 200 | 50 | 20 | 4 | 0.25 | 56.11 | 1.79 |
| 253 | Cone200_G50_A20_V4_5 | 200 | 50 | 20 | 4 | 0.25 | 51.92 | 1.65 |
| 254 | Cone200_G50_A20_V10_1 | 200 | 50 | 20 | 10 | 0.25 | 44.61 | 1.42 |
| 255 | Cone200_G50_A20_V10_2 | 200 | 50 | 20 | 10 | 0.25 | 37.40 | 1.19 |
| 256 | Cone200_G50_A20_V10_3 | 200 | 50 | 20 | 10 | 0.25 | 42.29 | 1.35 |
| 257 | Cone200_G50_A30_V01_1 | 200 | 50 | 30 | 0.1 | 0.25 | 234.58 | 7.47 |
| 258 | Cone200_G50_A30_V01_2 | 200 | 50 | 30 | 0.1 | 0.25 | 258.84 | 8.24 |
| 259 | Cone200_G50_A30_V01_3 | 200 | 50 | 30 | 0.1 | 0.25 | 257.48 | 8.20 |
| 260 | Cone200_G50_A30_V1_1 | 200 | 50 | 30 | 1 | 0.25 | 268.38 | 8.54 |
| 261 | Cone200_G50_A30_V1_2 | 200 | 50 | 30 | 1 | 0.25 | 313.62 | 9.98 |
| 262 | Cone200_G50_A30_V1_3 | 200 | 50 | 30 | 1 | 0.25 | 300.15 | 9.55 |
| 263 | Cone200_G50_A30_V1_L310 | 200 | 50 | 30 | 1 | 0.25 | 260.99 | 8.31 |
| 264 | Cone200_G50_A30_V2_1 | 200 | 50 | 30 | 2 | 0.25 | 57.53 | 1.83 |
| 265 | Cone200_G50_A30_V2_2 | 200 | 50 | 30 | 2 | 0.25 | 56.34 | 1.79 |

| ID | Test run | Diameter | Gap height | Cone Angle | Velocity | G/D | F_max | p_nom_max |
|-----|------------------------|----------|------------|------------|----------|------|--------|-----------|
| | | mm | mm | ° | mm/s | - | kN | MPa |
| 266 | Cone200_G50_A30_V2_3 | 200 | 50 | 30 | 2 | 0.25 | 40.36 | 1.28 |
| 267 | Cone200_G50_A30_V4_1 | 200 | 50 | 30 | 4 | 0.25 | 41.83 | 1.33 |
| 268 | Cone200_G50_A30_V4_2 | 200 | 50 | 30 | 4 | 0.25 | 59.84 | 1.90 |
| 269 | Cone200_G50_A30_V4_3 | 200 | 50 | 30 | 4 | 0.25 | 45.99 | 1.46 |
| 270 | Cone200_G50_A30_V10_1 | 200 | 50 | 30 | 10 | 0.25 | 44.17 | 1.41 |
| 271 | Cone200_G50_A30_V10_2 | 200 | 50 | 30 | 10 | 0.25 | 41.84 | 1.33 |
| 272 | Cone200_G50_A30_V10_3 | 200 | 50 | 30 | 10 | 0.25 | 42.39 | 1.35 |
| 273 | Cone200_G58_A30_V1_1 | 200 | 58 | 30 | 1 | 0.29 | 113.71 | 3.62 |
| 274 | Cone200_G58_A30_V1_2 | 200 | 58 | 30 | 1 | 0.29 | 174.90 | 5.57 |
| 275 | Cone200_G58_A30_V1_3 | 200 | 58 | 30 | 1 | 0.29 | 176.29 | 5.61 |
| 276 | Cone200_G100_A00_V01_1 | 200 | 100 | 0 | 0.1 | 0.5 | 196.09 | 6.24 |
| 277 | Cone200_G100_A00_V01_2 | 200 | 100 | 0 | 0.1 | 0.5 | 188.78 | 6.01 |
| 278 | Cone200_G100_A00_V01_3 | 200 | 100 | 0 | 0.1 | 0.5 | 194.37 | 6.19 |
| 279 | Cone200_G100_A00_V1_1 | 200 | 100 | 0 | 1 | 0.5 | 145.63 | 4.64 |
| 280 | Cone200_G100_A00_V1_2 | 200 | 100 | 0 | 1 | 0.5 | 79.09 | 2.52 |
| 281 | Cone200_G100_A00_V1_3 | 200 | 100 | 0 | 1 | 0.5 | 140.66 | 4.48 |
| 282 | Cone200_G100_A00_V2_1 | 200 | 100 | 0 | 2 | 0.5 | 98.17 | 3.12 |
| 283 | Cone200_G100_A00_V2_2 | 200 | 100 | 0 | 2 | 0.5 | 101.13 | 3.22 |
| 284 | Cone200_G100_A00_V2_3 | 200 | 100 | 0 | 2 | 0.5 | 104.31 | 3.32 |
| 285 | Cone200_G100_A00_V4_1 | 200 | 100 | 0 | 4 | 0.5 | 91.47 | 2.91 |
| 286 | Cone200_G100_A00_V4_2 | 200 | 100 | 0 | 4 | 0.5 | 107.63 | 3.43 |
| 287 | Cone200_G100_A00_V4_3 | 200 | 100 | 0 | 4 | 0.5 | 105.11 | 3.35 |
| 288 | Cone200_G100_A00_V7_1 | 200 | 100 | 0 | 7 | 0.5 | 95.44 | 3.04 |
| 289 | Cone200_G100_A00_V7_2 | 200 | 100 | 0 | 7 | 0.5 | 73.87 | 2.35 |
| 290 | Cone200_G100_A00_V7_3 | 200 | 100 | 0 | 7 | 0.5 | 69.33 | 2.21 |
| 291 | Cone200_G100_A00_V10_1 | 200 | 100 | 0 | 10 | 0.5 | 74.54 | 2.37 |
| 292 | Cone200_G100_A00_V10_2 | 200 | 100 | 0 | 10 | 0.5 | 108.37 | 3.45 |
| 293 | Cone200_G100_A00_V10_3 | 200 | 100 | 0 | 10 | 0.5 | 60.74 | 1.93 |
| 294 | Cone200_G100_A10_V01_1 | 200 | 100 | 10 | 0.1 | 0.5 | 106.53 | 3.39 |
| 295 | Cone200_G100_A10_V01_2 | 200 | 100 | 10 | 0.1 | 0.5 | 97.81 | 3.11 |
| 296 | Cone200_G100_A10_V01_3 | 200 | 100 | 10 | 0.1 | 0.5 | 94.27 | 3.00 |
| 297 | Cone200_G100_A10_V1_1 | 200 | 100 | 10 | 1 | 0.5 | 56.52 | 1.80 |
| 298 | Cone200_G100_A10_V1_2 | 200 | 100 | 10 | 1 | 0.5 | 39.23 | 1.25 |
| 299 | Cone200_G100_A10_V1_3 | 200 | 100 | 10 | 1 | 0.5 | 45.00 | 1.43 |
| 300 | Cone200_G100_A10_V2_1 | 200 | 100 | 10 | 2 | 0.5 | 45.80 | 1.46 |
| 301 | Cone200_G100_A10_V2_2 | 200 | 100 | 10 | 2 | 0.5 | 43.36 | 1.38 |
| 302 | Cone200_G100_A10_V2_3 | 200 | 100 | 10 | 2 | 0.5 | 37.17 | 1.18 |
| 303 | Cone200_G100_A10_V4_1 | 200 | 100 | 10 | 4 | 0.5 | 37.55 | 1.20 |
| 304 | Cone200_G100_A10_V4_2 | 200 | 100 | 10 | 4 | 0.5 | 35.96 | 1.14 |
| 305 | Cone200_G100_A10_V4_3 | 200 | 100 | 10 | 4 | 0.5 | 37.40 | 1.19 |
| 306 | Cone200_G100_A10_V7_1 | 200 | 100 | 10 | 7 | 0.5 | 39.40 | 1.25 |
| 307 | Cone200_G100_A10_V7_2 | 200 | 100 | 10 | 7 | 0.5 | 33.50 | 1.07 |
| 308 | Cone200_G100_A10_V7_3 | 200 | 100 | 10 | 7 | 0.5 | 39.92 | 1.27 |
| 309 | Cone200_G100_A10_V10_1 | 200 | 100 | 10 | 10 | 0.5 | 27.47 | 0.87 |
| 310 | Cone200_G100_A10_V10_2 | 200 | 100 | 10 | 10 | 0.5 | 49.11 | 1.56 |
| 311 | Cone200_G100_A10_V10_3 | 200 | 100 | 10 | 10 | 0.5 | 39.09 | 1.24 |
| 312 | Cone200_G100_A20_V001 | 200 | 100 | 20 | 0.01 | 0.5 | 122.28 | 3.89 |
| 313 | Cone200_G100_A20_V01_1 | 200 | 100 | 20 | 0.1 | 0.5 | 104.90 | 3.34 |
| 314 | Cone200_G100_A20_V01_2 | 200 | 100 | 20 | 0.1 | 0.5 | 98.82 | 3.15 |
| 315 | Cone200_G100_A20_V01_3 | 200 | 100 | 20 | 0.1 | 0.5 | 98.25 | 3.13 |
| 316 | Cone200_G100_A20_V1_1 | 200 | 100 | 20 | 1 | 0.5 | 38.21 | 1.22 |
| 317 | Cone200_G100_A20_V1_2 | 200 | 100 | 20 | 1 | 0.5 | 30.32 | 0.97 |
| 318 | Cone200_G100_A20_V1_3 | 200 | 100 | 20 | 1 | 0.5 | 31.72 | 1.01 |

| ID | Test run | Diameter | Gap height | Cone Angle | Velocity | G/D | F_max | p_nom_max |
|-----|------------------------|----------|------------|------------|----------|--------|----------|-----------|
| | | mm | mm | ° | mm/s | - | kN | MPa |
| 319 | Cone200_G100_A20_V2_1 | 200 | 100 | 20 | 2 | 0.5 | 38.81 | 1.24 |
| 320 | Cone200_G100_A20_V2_2 | 200 | 100 | 20 | 2 | 0.5 | 43.94 | 1.40 |
| 321 | Cone200_G100_A20_V2_3 | 200 | 100 | 20 | 2 | 0.5 | 37.05 | 1.18 |
| 322 | Cone200_G100_A20_V4_1 | 200 | 100 | 20 | 4 | 0.5 | 26.31 | 0.84 |
| 323 | Cone200_G100_A20_V4_2 | 200 | 100 | 20 | 4 | 0.5 | 32.90 | 1.05 |
| 324 | Cone200_G100_A20_V4_3 | 200 | 100 | 20 | 4 | 0.5 | 39.16 | 1.25 |
| 325 | Cone200_G100_A20_V7_1 | 200 | 100 | 20 | 7 | 0.5 | 35.52 | 1.13 |
| 326 | Cone200_G100_A20_V7_2 | 200 | 100 | 20 | 7 | 0.5 | 35.27 | 1.12 |
| 327 | Cone200_G100_A20_V7_3 | 200 | 100 | 20 | 7 | 0.5 | 23.75 | 0.76 |
| 328 | Cone200_G100_A20_V10_1 | 200 | 100 | 20 | 10 | 0.5 | 30.22 | 0.96 |
| 329 | Cone200_G100_A20_V10_2 | 200 | 100 | 20 | 10 | 0.5 | 39.65 | 1.26 |
| 330 | Cone200_G100_A20_V10_3 | 200 | 100 | 20 | 10 | 0.5 | 38.34 | 1.22 |
| 331 | Cone200_G100_A30_V01_1 | 200 | 100 | 30 | 0.1 | 0.5 | 162.15 | 5.16 |
| 332 | Cone200_G100_A30_V01_2 | 200 | 100 | 30 | 0.1 | 0.5 | 89.62 | 2.85 |
| 333 | Cone200_G100_A30_V01_3 | 200 | 100 | 30 | 0.1 | 0.5 | 82.03 | 2.61 |
| 334 | Cone200_G100_A30_V1_1 | 200 | 100 | 30 | 1 | 0.5 | 32.53 | 1.04 |
| 335 | Cone200_G100_A30_V1_2 | 200 | 100 | 30 | 1 | 0.5 | 28.20 | 0.90 |
| 336 | Cone200_G100_A30_V1_3 | 200 | 100 | 30 | 1 | 0.5 | 34.76 | 1.11 |
| 337 | Cone200_G100_A30_V2_1 | 200 | 100 | 30 | 2 | 0.5 | 30.82 | 0.98 |
| 338 | Cone200_G100_A30_V2_2 | 200 | 100 | 30 | 2 | 0.5 | 33.69 | 1.07 |
| 339 | Cone200_G100_A30_V2_3 | 200 | 100 | 30 | 2 | 0.5 | 45.62 | 1.45 |
| 340 | Cone200_G100_A30_V4_1 | 200 | 100 | 30 | 4 | 0.5 | 34.74 | 1.11 |
| 341 | Cone200_G100_A30_V4_2 | 200 | 100 | 30 | 4 | 0.5 | 44.32 | 1.41 |
| 342 | Cone200_G100_A30_V4_3 | 200 | 100 | 30 | 4 | 0.5 | 28.05 | 0.89 |
| 343 | Cone200_G100_A30_V7_1 | 200 | 100 | 30 | 7 | 0.5 | 28.23 | 0.90 |
| 344 | Cone200_G100_A30_V7_2 | 200 | 100 | 30 | 7 | 0.5 | 38.36 | 1.22 |
| 345 | Cone200_G100_A30_V7_3 | 200 | 100 | 30 | 7 | 0.5 | 31.82 | 1.01 |
| 346 | Cone200_G100_A30_V10_1 | 200 | 100 | 30 | 10 | 0.5 | 32.98 | 1.05 |
| 347 | Cone200_G100_A30_V10_2 | 200 | 100 | 30 | 10 | 0.5 | 37.93 | 1.21 |
| 348 | Cone200_G100_A30_V10_3 | 200 | 100 | 30 | 10 | 0.5 | 27.56 | 0.88 |
| 349 | Cone200_G200_A00_V01_1 | 200 | 200 | 0 | 0.1 | 1 | 234.38 | 7.46 |
| 350 | Cone200_G200_A00_V01_2 | 200 | 200 | 0 | 0.1 | 1 | 226.55 | 7.21 |
| 351 | Cone200_G200_A00_V01_3 | 200 | 200 | 0 | 0.1 | 1 | 237.19 | 7.55 |
| 352 | Cone200_G200_A00_V1_1 | 200 | 200 | 0 | 1 | 1 | 159.11 | 5.06 |
| 353 | Cone200_G200_A00_V1_2 | 200 | 200 | 0 | 1 | 1 | 124.23 | 3.95 |
| 354 | Cone200_G200_A00_V1_3 | 200 | 200 | 0 | 1 | 1 | 142.22 | 4.53 |
| 355 | Cone200_G200_A00_V2_1 | 200 | 200 | 0 | 2 | 1 | 110.01 | 3.50 |
| 356 | Cone200_G200_A00_V2_2 | 200 | 200 | 0 | 2 | 1 | 145.83 | 4.64 |
| 357 | Cone200_G200_A00_V2_3 | 200 | 200 | 0 | 2 | 1 | 53.17 | 1.69 |
| 358 | Cone200_G200_A00_V4_1 | 200 | 200 | 0 | 4 | 1 | 100.49 | 3.20 |
| 359 | Cone200_G200_A00_V4_2 | 200 | 200 | 0 | 4 | 1 | 109.45 | 3.48 |
| 360 | Cone200_G200_A00_V4_3 | 200 | 200 | 0 | 4 | 1 | 75.95 | 2.42 |
| 361 | Cone200_G200_A00_V7_1 | 200 | 200 | 0 | 7 | 1 | 147.41 | 4.69 |
| 362 | Cone200_G200_A00_V7_2 | 200 | 200 | 0 | 7 | 1 | 150.43 | 4.79 |
| 363 | Cone200_G200_A00_V7_3 | 200 | 200 | 0 | 7 | 1 | 106.63 | 3.39 |
| 364 | Cone200_G200_A00_V10_1 | 200 | 200 | 0 | 10 | 1 | 121.76 | 3.88 |
| 365 | Cone200_G200_A00_V10_2 | 200 | 200 | 0 | 10 | 1 | 136.10 | 4.33 |
| 366 | Cone200_G200_A00_V10_3 | 200 | 200 | 0 | 10 | 1 | 137.76 | 4.39 |
| 367 | Cone800_G100_A20_V01 | 800 | 100 | 20 | 0.1 | 0.125 | 3,624.82 | 7.21 |
| 368 | Cone800_G100_A20_V4_1 | 800 | 100 | 20 | 4 | 0.125 | 2,935.00 | 5.84 |
| 369 | Cone800_G100_A20_V4_2 | 800 | 100 | 20 | 4 | 0.125 | 2,360.64 | 4.70 |
| 370 | Cone800_G230_A30_V04 | 800 | 230 | 30 | 0.4 | 0.2875 | 2,497.99 | 4.97 |
| 371 | Cone800_G230_A30_V4_1 | 800 | 230 | 30 | 4 | 0.2875 | 512.09 | 1.02 |